



5-2018

## **Electronic Functionalities in Two-Dimensional Layered Materials for Device Applications**

Akinola David Oyedele  
*University of Tennessee*, [aoyedele@vols.utk.edu](mailto:aoyedele@vols.utk.edu)

Follow this and additional works at: [https://trace.tennessee.edu/utk\\_graddiss](https://trace.tennessee.edu/utk_graddiss)

---

### **Recommended Citation**

Oyedele, Akinola David, "Electronic Functionalities in Two-Dimensional Layered Materials for Device Applications." PhD diss., University of Tennessee, 2018.  
[https://trace.tennessee.edu/utk\\_graddiss/4883](https://trace.tennessee.edu/utk_graddiss/4883)

This Dissertation is brought to you for free and open access by the Graduate School at TRACE: Tennessee Research and Creative Exchange. It has been accepted for inclusion in Doctoral Dissertations by an authorized administrator of TRACE: Tennessee Research and Creative Exchange. For more information, please contact [trace@utk.edu](mailto:trace@utk.edu).

To the Graduate Council:

I am submitting herewith a dissertation written by Akinola David Oyedele entitled "Electronic Functionalities in Two-Dimensional Layered Materials for Device Applications." I have examined the final electronic copy of this dissertation for form and content and recommend that it be accepted in partial fulfillment of the requirements for the degree of Doctor of Philosophy, with a major in Energy Science and Engineering.

Kai Xiao, Major Professor

We have read this dissertation and recommend its acceptance:

Gong Gu, David G. Mandrus, Philip D. Rack, David Geohegan

Accepted for the Council:

Dixie L. Thompson

Vice Provost and Dean of the Graduate School

(Original signatures are on file with official student records.)

# **Electronic Functionalities in Two-Dimensional Layered Materials for Device Applications**

A Dissertation Presented for the  
Doctor of Philosophy  
Degree  
The University of Tennessee, Knoxville

Akinola David Oyedele

May 2018

## **Dedication**

This dissertation is dedicated -

**To the glory of God,**  
the giver of life and the source of wisdom.

**In loving memory of my father,**  
Olufemi Buraimo Oyedele,  
who inspired and supported my interest in science.

**To my beloved mother,**  
Olufunmilayo Florence Oyedele,  
for her ceaseless prayers and emotional kindness.

**To my partner,**  
Adeola Idowu Adediran,  
for strong support since the beginning of this journey.

**To my son,**  
Moyosore Olabomi Oyedele,  
for always being a source of joy. His arrival created an epiphany to embrace life's  
journey rather than focusing on the destination. Because, destination is an illusion.  
The end of one journey is the beginning of another.

## Acknowledgments

This dissertation is a result of the collective effort of many people without which it would not have been possible. First, I would like to wholeheartedly appreciate my advisor, Dr. Kai Xiao for his constant guidance and mentorship during my Ph.D. Dr. Xiao was particularly patient and displayed trust in my ability to hone the requisite skills needed for scientific investigations. He spent a significant amount of his time discussing my research results and helped me with feedbacks to improve my scientific communication.

I would like to thank Dr. David Geohegan for supporting my research work at the Center for Nanophase Materials Science (CNMS), Oak Ridge National Laboratory and for his insightful discussions. Special thanks to my committee members; Prof. David Mandrus, Prof. Philip Rack and Prof. Gong Gu for spending their valuable time and giving me important suggestions on my dissertation. I would also like to thank -

- Dr. Pushpa Raj Pudasaini, for his excellent collaboration, important scientific discussions and his moral and academic support.
- Dr. Liangbo Liang, Dr. Shize Yang, Dr. Masoud Mahjouri-Samani, Dr. Alexandra Puretzky, and Dr. Kai Wang, for their insightful and rewarding collaborations. Dr. Liang performed density functional theory (DFT) calculations to support my experimental work. Dr. Yang carried out scanning transmission electron microscopy (STEM) investigation on my PdSe<sub>2</sub> samples. And Dr. Puretzky, helped with the Raman and absorption spectroscopy measurements.
- Dr. Christopher Rouleau, for always willing to lend a helping hand. Dr. Rouleau designed the JACS publication cover and provided technical support for the AFM and probe-station instruments I used during my dissertation work.

- Alex Strasser and Yiyi Gu, who helped with some experiments.
- Dr. Sanjib Das and Dr. Bin Yang, for their constant encouragement.
- Ms. Tracy Whitaker and Ms. Kara Clayton, for enhancing my experience at CNMS.
- Prof. Lee Riedinger, Dr. Mike Simpson, Wanda Davis, and Jessica Garner of the Bredesen Center for their moral and financial support. I worked with Prof. Riedinger as a teaching assistant for 4 years. The experience was valuable to hone my teaching skills.
- Prof. Zheng Liu of NTU Singapore and Amanda Haglund for bulk material synthesis.
- Dr. Xufan Li, Dr. Michael Stanford, and Jingjie Zhang for their nice collaboration.
- Dr. Iliia Ivanov for Raman characterization.
- Dr. David Keffer and Dr. Orlando Rios for their mentorship and collaborations on developing atomistic models for the determining the structures of complex materials.
- My siblings, Kemi Idowu, Anu Oyedele, and Demilade Oyedele, for their understanding.
- My friends, Uche Anozie, Christine Ajinjeru, Eva Mutunga, Michael Henderson, Emily Bean, Dr. Janet and Mark Cockrum, who made my stay in Knoxville worthwhile.
- The Nigerian community in Knoxville for their loving support, – especially Dr. Femi & Remi Omitaomu and Mr. Shina Oshifala.
- Dr. Tunde Alawode and Wole Okusaga for their friendship.
- Liz Norred for her constructive feedback of the manuscript.
- The staff of nanofabrication research laboratory, CNMS for the technical support during device fabrication. Special thanks to Kevin Lester, Dayrl Briggs, Dale Hensley, Dr. Ivan Kravchenko and Dr. Jason Fowlkes and Dr. Ming-Wei Lin for showing me how to fabricate devices.

This research was conducted at CNMS which is a DOE Office of Science User facility at ORNL.

## Abstract

The rise of two-dimensional (2D) materials has enabled the realization of ultra-thin electronic devices with a broad range of applications in transistors, memory devices, photodetectors, chemical sensors, and electronic displays. The optoelectronic functionality displayed by this unique material class is determined by the underlying phenomena relating to their crystal structure, quantum confinement, and heterogeneities such as defects, dopants, and atomic interface in their heterostructures.

The first part of this thesis highlights the effects of heterogeneities in tuning the electronic functionalities of 2D materials. For example, the presence of sharp atomic interfaces could introduce p-n junction rectifying behavior which is the fundamental unit of electronic devices.

The second part introduces a novel 2D anisotropic material, palladium diselenide ( $\text{PdSe}_2$ ), with a unique pentagonal, puckered structure unlike most other 2D materials with hexagonal building blocks.  $\text{PdSe}_2$  displays a strong layer-dependent optical and electronic properties. Density Functional Theory (DFT) calculations and absorption spectroscopy reveal that  $\text{PdSe}_2$  exhibit a wide-tunable indirect bandgap from  $\sim 0$  eV in bulk to 1.3 eV in monolayer. Also, the anomalous layer-dependent Raman peak shifts around  $5 - 9 \text{ cm}^{-1}$  from bulk to monolayer for  $\text{PdSe}_2$  confirms the strong interlayer coupling in  $\text{PdSe}_2$ .

The third section discusses the field-effect transistor (FET) device performance of  $\text{PdSe}_2$ , which shows a characteristic high carrier mobility as high as  $158 \text{ cm}^2\text{V}^{-1}\text{s}^{-1}$  and air stability for wide-tunable electronic applications. Also,  $\text{PdSe}_2$  devices show temperature-dependent conductivity with observed metal to insulator (MIT) transition.



Finally, through plasma treatment, a new complementing metallic phase can be achieved from PdSe<sub>2</sub> that forms a sharp atomic interface with negligible Schottky barrier heights. The phase transformation process is understood to be induced by the removal of selenium atoms. The entirely new material, Pd<sub>17</sub>Se<sub>15</sub>, with an electrically-conducting property, is used as a contact for PdSe<sub>2</sub> devices which resulted in the reduction of the Schottky barrier present at the metal-semiconductor interface. This realization is an important step in the quest to eliminate contact resistance in 2D electronic devices.

The ease of manipulating the structure of 2D materials, coupled with ample device engineering opportunities, makes 2D materials viable candidates for future nano-electronics.

## Table of Contents

Chapter 1: Introduction .....	1
1.1 Motivation .....	1
1.2 Objectives.....	3
1.3 Organization of the thesis.....	3
Chapter 2: Literature Review .....	5
2.1 Introduction to 2D materials and their applications .....	5
2.2 Graphene .....	5
2.3 Transition Metal Dichalcogenides (TMDs) .....	8
2.4 Noble Transition Metal Dichalcogenides (NTMDs).....	11
2.5 Pentagonal building blocks of 2D materials .....	14
2.5.1 Penta-graphene .....	14
2.5.2 Penta-SnX <sub>2</sub> and others penta-2D materials .....	15
2.5.3 Pentagonal group-10 TMDs .....	17
2.6 Anisotropy in buckled and puckered 2D materials .....	17
Chapter 3: Atomically-thin van der Waals Heterostructure Built via Dry-Transfer .....	21
3.1 Introduction .....	21
3.2 Deterministic dry-transfer method .....	22
3.3 Results .....	25
3.3.1 InSe-WSe <sub>2</sub> Heterostructure.....	25
3.3.2 Black Phosphorus-MoSe <sub>2</sub> Heterostructure .....	30
3.4 Conclusion.....	33
Chapter 4: Structural, optical, and electronic properties of layered 2D PdSe <sub>2</sub> .....	35
4.1 Introduction .....	35
4.2 Growth and synthesis of bulk and few-layers PdSe <sub>2</sub> .....	38
4.3 Atomic structure of PdSe <sub>2</sub> .....	40
4.4 Electronic properties of PdSe <sub>2</sub> .....	42
4.4.1 Density Functional Theory (DFT) calculations.....	42
4.4.2 Phonon spectrum .....	50
4.4.3 Electronic band structure .....	50
4.5 Optical properties of PdSe <sub>2</sub> .....	53
4.5.1 Absorption spectroscopy .....	53

4.5.2 Raman spectroscopy .....	56
4.6 Summary .....	62
Chapter 5: Electrical transport properties of 2D PdSe <sub>2</sub> : high carrier-mobility and anisotropic behavior.....	64
5.1 Introduction .....	64
5.2 Device fabrication and architecture.....	65
5.3 Layer-dependent ambipolar conduction, high mobility and air stability in PdSe <sub>2</sub> .....	65
5.4 Temperature-dependent properties in PdSe <sub>2</sub> .....	73
5.5 Anisotropic properties of PdSe <sub>2</sub> .....	77
5.6.1 Raman spectroscopy .....	78
5.6.2 Structure anisotropy characterized by second-harmonic generation (SHG) .....	82
5.6.3 Anisotropic electrical behavior of 2D PdSe <sub>2</sub> .....	84
5.6 Summary .....	86
Chapter 6: Vacancy-induced phase transition in layered PdSe <sub>2</sub> .....	87
6.1 Introduction .....	87
6.2 Phase-transition mechanism in PdSe <sub>2</sub> .....	88
6.3 Structural properties of PdSe <sub>2</sub> and the new phase.....	89
6.4 Optical properties in PdSe <sub>2</sub> and the new phase .....	93
6.5 Improved contact resistance with PdSe <sub>2</sub> /Pd <sub>17</sub> Se <sub>15</sub> heterojunction Field Effect Transistors (FETs).....	98
6.6 Summary .....	102
Chapter 7: Conclusion.....	103
7.1 Major contributions of this thesis.....	103
7.2 Recommendations for future work.....	104
References.....	107
Appendix.....	115
Author's published journal papers .....	116
Conference presentations .....	118
Notable awards.....	119
Vita.....	121

## List of Tables

Table 4.1: Optimized bulk PdSe <sub>2</sub> lattice constants using different functionals with projector-augmented-wave (PAW) pseudopotentials in the DFT package of VASP. The experimental values are also shown in the second column for comparison .....	44
Table 4.2: Optimized bulk PdSe <sub>2</sub> lattice constants using different functionals with projector-augmented-wave (PAW) pseudopotentials in the DFT package of Quantum Espresso.....	46
Table 4.3: Optimized bulk PdSe <sub>2</sub> lattice constants using different functionals with Troullier-Martins type norm-conserving pseudopotentials in Quantum Espresso.....	47
Table 4.4: Calculated frequencies of the bulk-related Raman modes for 1L, 2L and bulk PdSe <sub>2</sub> .....	61
Table 6.1: Composition of atoms from the irradiated and pristine areas obtained from nano-Auger electron spectroscopy .....	95
Table 6.2: Comparison of the Schottky barrier heights at the heterointerface of metal-PdSe <sub>2</sub> .....	101

## List of Figures

<b>Figure 2.1.</b> Schematic diagram highlighting some applications of 2D materials. ....	6
<b>Figure 2.2.</b> Schematic diagram illustrating the crystal structure of graphene with a C-C interatomic distance of 1.42 Å. ....	7
<b>Figure 2.3.</b> Periodic table highlighting possible layered 2D materials. ....	10
<b>Figure 2.4.</b> Side and top view of the crystal structure of monolayer MoS <sub>2</sub> .....	12
<b>Figure 2.5.</b> (a) Crystal structure of penta-graphene which matches the Cairo pentagonal tiling illustrated in (b). ....	16
<b>Figure 2.6.</b> (a) Side and top view of the crystal structure of PdSe <sub>2</sub> . (b) Puckered structure of black phosphorus. ....	18
<b>Figure 3.1.</b> Optical image of the deterministic dry-transfer setup. ....	23
<b>Figure 3.2.</b> Schematic illustration of the steps involved in the deterministic transfer of few-layers InSe onto a WSe <sub>2</sub> flake.....	24
<b>Figure 3.3.</b> (a) Optical image of the first flake (few-layer WSe <sub>2</sub> ) mechanically exfoliated on the Si/SiO <sub>2</sub> substrate. (inset): The thickness profile of few-layer WSe <sub>2</sub> corresponding to the white line in (2d). (b) Optical image after the transfer of the second flake (few-layer InSe) on the WSe <sub>2</sub> flake to form a heterojunction. (b) Inset: The thickness profile of few-layer InSe corresponding to the red line in (2c). (c) The atomic force microscopy (AFM) image of the FET device. (d) Raman spectra for WSe <sub>2</sub> , the heterostructure, and InSe arranged in a stacking manner. ....	26

**Figure 3.4.** (a) Schematic of the WSe<sub>2</sub>-InSe heterojunction field effect transistor (FET) device. (b) The suggested band alignment for few-layer WSe<sub>2</sub> and InSe flakes showing type-II heterojunction. (c) The transfer characteristics of the WSe<sub>2</sub>, InSe and WSe<sub>2</sub>-InSe FET device with 2 V source-drain bias (in logarithmic scale). Inset: Schematic of the WSe<sub>2</sub>-InSe field effect transistor device. The left y-axis corresponds to the red (InSe- WSe<sub>2</sub>) curve, while the right y-axis corresponds to the blue (InSe) and black (WSe<sub>2</sub>) curves. (d) Output characteristics of the FET based on WSe<sub>2</sub>-InSe heterostructures at different gate bias. (e-f) Output characteristics of InSe and WSe<sub>2</sub>, at various gate bias, showing symmetric behaviors.....28

**Figure 3.5.** (a) Optical image of MoSe<sub>2</sub>-black phosphorus heterostructure. The inserted lines are where AFM heights profile in (b) were taken. The red and black profiles are for monolayer MoSe<sub>2</sub> and black phosphorus, respectively. (c) Photoluminescence spectra of monolayer MoSe<sub>2</sub>, with signature emission at ~1.53 eV. (d) Raman spectra of MoSe<sub>2</sub> and black phosphorus and the heterostructure, showing the presence of individual peaks in the heterostructure formed. ...31

**Figure 3.6.** (a) Optical image of MoSe<sub>2</sub>-black phosphorus heterostructure, with electrical contact of Ti/Au. (b) Transfer characteristics of monolayer MoSe<sub>2</sub> and black phosphorus, showing predominant n-type and p-type behaviors, respectively. The left y-axis corresponds to the red (MoSe<sub>2</sub>) curve, while the right y-axis corresponds to the black (black phosphorus) curve. (c) Transfer curve of the heterostructure, displaying both n-type and p-type conduction typical of a p-n junction. The left y-axis corresponds to the black (logarithmic scale) curve, while the right y-axis corresponds to the red (linear scale) curve. (d) Output characteristics of the heterojunction with a rectifying behavior at different gate bias. Inset shows the output curve at zero gate bias. (e) Output characteristics of monolayer MoSe<sub>2</sub> and (f) black phosphorus, at various gate bias, showing linear-symmetric behaviors.....32

**Figure 4.1.** Polymorphism in 2D materials displayed across hexagonal flat graphene (a), hexagonal puckered black phosphorus (b), and pentagonal puckered PdSe<sub>2</sub> (c). (d) Top and side view of the crystal structure of monolayer PdSe<sub>2</sub> showing a puckered pentagonal configuration. The gray spheres represent the Pd atoms, while the yellow spheres represent the Se atoms. Dashed line indicates the unit cell. The vertical puckering distance,  $\delta$ , is around  $\sim 1.6$  Å. (e) Crystal structure of tri-layer PdSe<sub>2</sub> with dashed line indicating the unit cell.....36

**Figure 4.2.** (a) Schematic of the thermal furnace used for the growth of PdSe<sub>2</sub> bulk single crystals. (b) Image of the as-grown PdSe<sub>2</sub> single crystals ( $\sim 4$  mm). (c) Powder XRD pattern of the as-synthesized PdSe<sub>2</sub> sample. (d-f) Optical images of single and few-layer PdSe<sub>2</sub>. (g-h) Atomic force microscopy image and height profile corresponding to image (f) and its inset.....39

**Figure 4.3.** Atomic resolution structure of few-layer PdSe<sub>2</sub> crystals revealed by Z-contrast STEM images (top row) and corresponding simulated images (bottom row) of PdSe<sub>2</sub>. (a, c) Single layer, (b, e) Even number of layers, (c, f) odd number of layers. Insets in (d-f) show atomic models of the corresponding STEM images.....41

**Figure 4.4.** (a-c) The atomic resolution STEM images of PdSe<sub>2</sub> monolayer, (b) even layer (c) and odd layer. Insets of these STEM images show the corresponding Fast Fourier Transformation diffraction patterns. Diffraction spots corresponding to two principle planes (020) and (200) are labeled. (d) A low-magnification STEM image of few-layer PdSe<sub>2</sub> crystal. Inset shows the line profile of the red dash line in image which the layer thickness is determined to be 4L and 6L according intensity. (e) Electron energy loss spectroscopy of few-layer PdSe<sub>2</sub>, Pd N edge, Pd M edge and Se M edge are shown in the spectra. ....43

**Figure 4.5.** Calculated phonon dispersion spectrum of single-layer and few-layers of PdSe<sub>2</sub>. There are no noticeable soft modes in 1L PdSe<sub>2</sub>, while the small negative frequencies are probably due to the computational error. ....51

**Figure 4.6.** Calculated electronic band structures of (a) 1L, (b) bulk, (c) 2L and (d) 3L PdSe<sub>2</sub> by the PBE method. The dashed arrows indicate the lowest energy transitions between the valence band maximum (VBM) and conduction band minimum (CBM). The VBM is set at 0 eV. Inset of figure shows Brillouin zones of PdSe<sub>2</sub> 2D crystals with high-symmetry points labeled.....52

**Figure 4.7.** (a) Plot of the absorbance versus the number of layers where the number of layers was determined by AFM. (b) Plot of absorbance with the number of layers determined based on absorbance measured at 800 nm that was used in the analysis of the bandgap. (c) Absorption spectra for the selected number of layers. (d-g) Tauc plots for 1, 4, 16 and 42 layers, respectively which demonstrates how the bandgap was extrapolated. (h) Band gaps extracted from the Tauc plots for various number of PdSe<sub>2</sub> layers derived from the optical absorption spectra. (i) Band gaps obtained from first-principles calculations - PBE and optPBE shown in red and black dots, respectively. ....54

**Figure 4.8.** (a) Layer-dependent Raman spectra of PdSe<sub>2</sub> from 1L to bulk measured for an excitation laser wavelength of 532 nm. (b) Corresponding calculated Raman spectra by the optPBE method. In both (a) and (b), the dashed lines indicate positions of the Raman peaks for bulk PdSe<sub>2</sub>. Note that the A<sub>g</sub><sup>1</sup>-B<sub>1g</sub><sup>1</sup> label means the overlapping of two close peaks: A<sub>g</sub><sup>1</sup> and B<sub>1g</sub><sup>1</sup>. For convenience, bulk notations of A<sub>g</sub> and B<sub>1g</sub> are also used for other systems. (c) Atomic displacements (blue arrows) of six Raman modes in bulk PdSe<sub>2</sub>. (d) Comparison of the experimental (black) and theoretical (red) frequencies of Raman modes A<sub>g</sub><sup>1</sup>-B<sub>1g</sub><sup>1</sup>, B<sub>1g</sub><sup>2</sup> and A<sub>g</sub><sup>3</sup> at



different thicknesses. Although the calculated frequencies are systematically smaller than the experimental ones, the trend of the frequency shift versus thickness agrees.....58

**Figure 4.9.** (a) Zoom-in Raman spectra for to see the presence of the  $B_{1g}^3$  shoulder peak near the  $A_g^3$  peak. The line spectra of the  $A_g^3$  and  $B_{1g}^3$  are fitted to the Raman spectra. (b) Calculated Raman spectra of PdSe<sub>2</sub> via the optPBE method at different thickness. (c) Polarization Raman spectra for several layers (~20 layers) PdSe<sub>2</sub> from experiment (d) bulk PdSe<sub>2</sub> from theory under different laser polarization configurations: unpolarized,  $\bar{z}(x, x)z$ , and  $\bar{z}(x, y)z$ . Both  $A_g$  and  $B_{1g}$  modes can be observed in the unpolarized spectra, only  $A_g$  modes can be observed under the parallel  $\bar{z}(x, x)z$  polarization configuration, while only  $B_{1g}$  modes can be observed under the perpendicular  $\bar{z}(x, y)z$  polarization configuration. ....60

**Figure 5.1.** (a) Fabrication of PdSe<sub>2</sub> FET: PdSe<sub>2</sub> flake is first exfoliated onto the substrate before the deposition of electrodes. (b) Optical image of fabricated devices. ....66

**Figure 5.2.** (a) Transfer curve of a typical ~5 L PdSe<sub>2</sub> device, with both logarithmic and linear scales, showing ambipolar characteristics (b) Typical output curves showing linear characteristics at 295 K for 20 L at positive back voltages  $V_{bg} = 60 \text{ V} \sim 0 \text{ V}$ . (c) Drain-source current versus back gate voltage plot for PdSe<sub>2</sub> with different number of layers at  $V_{ds} = 1.0 \text{ V}$  showing ambipolar behavior in all cases at room temperature, with logarithmic plot. (d) Thickness-dependent properties showing increasing off-current with thickness. (e) Electron and hole apparent mobility, and on/off ratio versus flakes thickness for PdSe<sub>2</sub> devices measured at room temperature. Black line indicates mobility curve, while red line indicates on/off ratio curves. Data points in squares and circles represents electron and holes, respectively. The electron mobilities are higher than hole mobilities, and thicker films consistently show lower on/off ratio than that of thinner flakes. ....67

**Figure 5.3.** Statistically analysis of the performance of 65 devices based on (a-b) apparent mobility and (c-d) on/off ratio for electron and hole conduction, respectively.....69

**Figure 5.4.** The transfer curve of pristine PdSe<sub>2</sub> FET and the device after 60 days exposed in air for (a) 10 L (b) 46 L.....71

**Figure 5.5.** Transfer characteristics of 20 L PdSe<sub>2</sub> (a) on 280 nm SiO<sub>2</sub> with Ti/Au contacts (b) with high work-function, Pd metal contacts, (c) on 50 nm Al<sub>2</sub>O<sub>3</sub> with Ti/Au contacts, and (d) with ionic-liquid top gate. The voltage bias used in (a-b) is 1.0 V, and 0.1 V for (c-d). .....72

**Figure 5.6.** (a) Drain-source current ( $I_{ds}$ ) versus voltage ( $V_{ds}$ ) at negative back voltages  $V_{bg} = -60$  V  $\sim$  0 V showing linear characteristics at 300 K. The inset shows a similar characteristic at positive back voltages  $V_{bg} = 60$  V  $\sim$  0 V, confirming the ambipolar characteristics of PdSe<sub>2</sub>. (b)  $I_{ds} - V_{ds}$  characteristics at 16 K, for negative back voltages. Inset shows for positive back voltages. (All measurements were from a 46 L PdSe<sub>2</sub>). .....74

**Figure 5.7.** (a) The electron apparent mobilities measured at different temperatures for PdSe<sub>2</sub> flakes with a thickness of 10 L. Below 100 K, the mobilities are independent of temperature, but above 100 K, the mobilities decrease with increasing temperature due to the phonon scattering, following a  $T^{-\gamma}$  dependence with  $\gamma$  close to 0.24. (b) Log-log plot of mobility as a function of the temperature for different number of layers through two-terminal configuration. The power-law coefficient,  $\gamma$  is extracted from the slope of the graph, which reveals phonon scattering mechanism for few-layers, and scattering by charged impurities for several layers. (c) Plot of on/off ratio (rounded to the nearest tens) with temperature for 10 L and 46 L PdSe<sub>2</sub>. (d) Plot of temperature dependence of the two-terminal conductance at different gate voltages for 10 L device. (e-f) Conductance as a function of gate voltage for different temperatures for PdSe<sub>2</sub> flakes with a thickness of 10 L and 46 L, respectively. The crossing around  $\sim$ 40 V for the 10 L device indicate

the change in temperature dependence which is absent in the 46 L device. Inset shows the color plot of the conductance as a function of temperature and gate bias. ....75

**Figure 5.8.** Theoretical polarization diagrams for (a)  $A_g$  symmetry and (b)  $B_{1g}$  symmetry Raman modes of PdSe<sub>2</sub> in parallel  $z(xx)\bar{z}$  and cross  $z(xy)\bar{z}$  polarization configurations. ....80

**Figure 5.9.** The major Raman peaks for 2L PdSe<sub>2</sub> measured in polarization configuration. Inserts show polar plots of Raman intensities versus polarization angles measured by rotating the sample. ....81

**Figure 5.10.** (a) Second harmonic generation (SHG) spectrum from PdSe<sub>2</sub> thin layers with different layer number (800 nm wavelength laser was utilized). b) The SHG intensity as a function of layer number. (c) Optical image of PdSe<sub>2</sub> with 4L and 3L regions. (d) SHG map of the PdSe<sub>2</sub> crystal showing intense SHG signal for 4L part of the crystal and almost no signal for the 3L part. (e) Integrated intensity of the SHG spectrum (from 380 to 420 nm) versus a rotation angle relative to the laser polarization. Two inserts show optical images of the PdSe<sub>2</sub> crystal corresponding to 0° (right) and 90° (top) crystal orientations relative to the laser polarization. The blue line shows fit with  $A + B\cos^2\alpha$  where  $A = 5925$  and  $B = 628$ . ....83

**Figure 5.11.** (a) Optical image of the device with the angular orientation. (b) Schematic of the crystal structure along the puckered axis. (c) STEM image showing the zigzag puckered structure. (d) Angular dependence transconductance and field-effect mobility. ....85

**Figure 6.1.** (a) Optical image of ~40 nm thick PdSe<sub>2</sub> before and after 10s argon plasma treatment. (b) Scanning electron microscope (SEM) image of pristine and irradiated PdSe<sub>2</sub> on TEM grid. (c) Atomic resolution STEM image of pristine PdSe<sub>2</sub>. (d) Schematic diagram depicting the phase transformation process. (e-f) Atomic resolution structure of irradiated PdSe<sub>2</sub> crystals revealed by

Z-contrast STEM images and corresponding simulated images (g-h). Insets in (e) shows atomic models of the STEM image. ....90

**Figure 6.2.** (a) Cross-sectional SEM image of the PdSe<sub>2</sub>/Pd<sub>17</sub>Se<sub>15</sub> phase transformation. (b-c) Shows the atomic structure of PdSe<sub>2</sub> and Pd<sub>17</sub>Se<sub>15</sub>, respectively, overlaid with their atomic models. (d) Cross-section STEM of the PdSe<sub>2</sub>/Pd<sub>17</sub>Se<sub>15</sub> heterointerface with possible reaction surface schematically illustrated in (e). The FFT of the Pd<sub>17</sub>Se<sub>15</sub> is shown in (f) with diffraction patterns of (220), ( $\overline{322}$ ) and ( $4\overline{12}$ ). ....92

**Figure 6.3.** (a) Stokes and anti-Stokes Raman spectra of pristine and irradiated PdSe<sub>2</sub> crystals with a focus on the high-frequency (HF) region (b), and low-frequency (LF) region (c) for ~10 nm thick flake. (d) Raman spectra on ~ 7 nm thick flakes using a lower plasma power of 25 W, with treatment done at 3 sec intervals. ....94

**Figure 6.4.** (a) Scanning electron microscope of irradiated and pristine regions of PdSe<sub>2</sub> crystal. (b) Survey spectra in both direct mode and (d) derivative mode which indicates the presence of Pd, Se, C, Si, and O atoms. (c) top image: gray scale maps for Pd, and Se obtained from the atomic composition in the survey spectra. Bottom image: color maps showing an increase in relative Pd composition for the irradiated areas. ....96

**Figure 6.5.** (a) Output characteristics of Pd<sub>17</sub>Se<sub>15</sub> device showing no gate dependence at room temperature. (b) Temperature-dependent output characteristics displaying a decrease in conductivity with temperature. (c) Optical image of PdSe<sub>2</sub> FET with Pd<sub>17</sub>Se<sub>15</sub> edge contacts. (d) Transfer characteristics for the metallic contacts and PdSe<sub>2</sub> semiconducting channel. (e) Temperature-dependent transfer characteristics. (f) The log(I<sub>ds</sub>) versus 1/T curves at different drain

bias and the corresponding extracted slopes in (g). (h) Schematic diagram showing the absence of Schottky barrier in Pd<sub>17</sub>Se<sub>15</sub>/PdSe<sub>2</sub> junction. ....99

## List of Symbols and Abbreviations

$\alpha$	Absorption spectroscopy coefficient
$\gamma$	Power-law coefficient
$\lambda$	Wavelength
$\mu$	Mobility
2D	Two-Dimensional
ADF	Annular Dark-Field
AES	Auger Electron Spectroscopy
AFM	Atomic Force Microscopy
BP	Black Phosphorus
CBM	Conduction-Band Minimum
CCD	Charge-Coupled Device
CNMS	Center for Nanophase Materials Science
CVD	Chemical Vapor Deposition
DFT	Density Functional Theory
DI	Deionized
EELS	Electron Energy Loss Spectroscopy
FET	Field-Effect Transistor

$I_{ds}$	Drain-source Current
InSe	Indium selenide
IPA	Isopropanol
IPR	Isolated Pentagon Rule
IQHE	Integer Quantum Hall Effect
LDA	Local Density Approximation
LED	Light-Emitting Diode
MIT	Metal-Insulator Transition
MoSe <sub>2</sub>	Molybdenum diselenide
NASA	National Aeronautics and Space Administration
OM	Optical Microscopy
PAW	Projector-Augmented-Wave
PBE	Perdew-Burke-Ernzerhof
PDMS	Polydimethylsiloxane
PMMA	Poly(methyl methacrylate)
QSH	Quantum-Spin Hall
SCS	Semiconductor Characterization System
SEM	Scanning Electron Microscopy

SHG	Second Harmonic Generation
STEM	Scanning Transmission Electron Microscopy
T	Temperature
TEM	Transmission Electron Microscopy
TMD	Transition Metal Dichalcogenide
VASP	Vienna Ab initio Simulation Package
VBM	Valence Band Maximum
$V_{ds}$	Drain-source Voltage
vdW	van der Waal
$V_g$	Gate voltage
WSe <sub>2</sub>	Tungsten diselenide
XRD	X-ray Diffraction



# Chapter 1: Introduction

## 1.1 Motivation

The growth in the semiconductor industry has revolutionized various aspects of human lives through the development of ubiquitous technologies such as personal computers, electronic displays, and smartphones. The rapid adoption of these digital innovations is because of their efficiency, durability, scalability, and multi-functionality. If we look at the trends of electronic devices in the past half-decade, we'll notice that we have made great progress in increasing their capabilities. For example, the smartphones of today are more powerful and faster than the computer used by NASA during the Apollo mission. This progress is because of the ability to miniaturize transistor circuits into smaller and smaller areas, leading to increased transistor density and consequently higher performance. Gordon Moore proposed an axiom, "Moore's law", that suggests that electronic devices double in speed and capability about every two years due to approximately doubling of the number of transistors integrated in a device.<sup>1</sup> Indeed, every year, the electronics industry has come up with new, faster, smarter and better devices. However, we are approaching the limit of miniaturizing current silicon technologies, which raises the question, "how do we keep up with Moore's law?" In addition to keeping with Moore's law, changes in our society necessitates the development of electronic devices that can meet future demands. For example, the future of electronic devices is light-weight, transparent, cheaper, faster, smaller, scalable, efficient, foldable, tunable and flexible. Moreover, owing to the challenge of recycling electronic wastes, self-cleaning and dissolvable electronic materials are desired. Therefore, it is important to engineer current systems and explore new materials to develop next-generation devices that will meet the requirements for future electronic devices.

Two-dimensional (2D) layered materials represent an emerging class of nanomaterials which have characteristic mechanical and electronic properties that make them relevant for future electronic applications. 2D layered materials like graphene, MoS<sub>2</sub> and black phosphorus are composed of atomically-thin layers with in-plane strong covalent bonds and separated by weak van der Waal forces, which makes it possible to isolate each layer with scotch tape. 2D materials have characteristic high crystallinity, lack dangling bonds, high optical transparency, and high mechanical flexibility which makes them interesting for electronic applications. Moreover, 2D materials can effectively deal with the short-channel effect problems that have limited the continuous scale of silicon technologies, while offering a route to expand the number of transistors in Integrated Circuits (ICs). Also, the 2D feature is unique in which charge carriers are restricted to the 2D space which allows for studying their electronic, physical and chemical properties due to quantum confinement. 2D materials can exhibit semiconductor, insulator, conductor, superconductor, magnetic, and thermoelectric behaviors, which are suitable not only to the semiconductor industry, but also in flexible electronics, superconductors, capacitors, batteries, thermoelectrics, piezoelectrics, and memory devices.

For electronic applications, 2D semiconductors with wide tunability, high on/off ratio, high mobility, and air stability are desired for switching and logic applications. In the search for highly desirable 2D materials, graphene, MoS<sub>2</sub>, and black phosphorus have received a lot of attention. For example, graphene has gained prominence due to its high carrier mobility resulting from an effectively massless state of charge carriers,<sup>2</sup> but its inherent lack of a band gap, and the inability so far to induce a sizable one, limits its application in electronics. This led to the exploration of transition metal dichalcogenides (TMDs) and other 2D materials beyond graphene.<sup>3</sup> In this regard, MoS<sub>2</sub> has attracted the most attention because of its moderate mobility and high current on/off

ratio in transistors, however, MoS<sub>2</sub> possesses a limited band gap variation between ~1.2 – 1.9 eV,<sup>4,5</sup>. Until the recent introduction of black phosphorus (BP), with a band gap variation from 0.3 – 1.5 eV, materials with such a widely tunable band gap were difficult to find.<sup>6</sup> BP has a honeycomb network similar to graphene, but is unstable in air. To this end, the aim of this thesis is to engineer existing 2D materials and explore new ones to achieve desired functionalities for electronic device applications.

## 1.2 Objectives

The main objectives of this thesis are as follows:

1. To study the effects of heterogeneities on the optoelectronic functionality of 2D materials.
2. To introduce wide-tunable electronics using novel 2D PdSe<sub>2</sub> and examine the origin of its strong layer dependence on optical and electronic properties.
3. To realize PdSe<sub>2</sub> FET devices, and study their transport characteristics.
4. To engineer phase of the PdSe<sub>2</sub> to achieve a single-material device architecture.

## 1.3 Organization of the thesis

The thesis is organized in the following manner:

- Chapter 2 reviews the status of 2D materials and their applications in electronic devices. A short review compares the structure-property relationships of hexagonal building blocks, such as graphene and pentagonal building blocks, like penta-graphene. In addition, an overview of noble transition metal dichalcogenides (TMDs) are presented, while highlighting the differences between TMDs with group-6 and -10 transition metals. Lastly, the properties of anisotropic 2D materials, such as BP and SnSe<sub>2</sub> are summarized.

- Chapter 3 discusses the effect of sharp atomic interfaces on the electronic properties of 2D materials
- Chapter 4 discusses the structure of novel pentagonal PdSe<sub>2</sub> and the consequence of its strong layer interaction on optical and electronic properties from both experimental and theoretical perspectives.
- Chapter 5 presents PdSe<sub>2</sub> FET with ambipolar conduction, high carrier mobility, and air-stability. In addition, the temperature dependent transport properties of PdSe<sub>2</sub> are demonstrated with characteristic metal-insulator transition in few-layer systems.
- Chapter 6 introduces the construction of single-material device to eliminate Schottky barriers present at the metal-active channel interface in transistors. Phase transformation of PdSe<sub>2</sub> through Se- atoms removal achieved a metallic-PdSe<sub>2</sub> phase that provide perfect ohmic contact with PdSe<sub>2</sub> active-channel.
- Chapter 7 highlights original contributions and gives recommendations for future work.

## Chapter 2: Literature Review

### 2.1 Introduction to 2D materials and their applications

Two-dimensional (2D) materials<sup>7</sup> have been identified as one of the top emerging technologies that will drive the fourth industrial revolution due to their remarkable physics and potential applications in flexible, ultra-thin and wearable electronics.<sup>8</sup> Research on ultrathin two-dimensional (2D) nanomaterials has grown exponentially in the fields of condensed matter physics, material science, chemistry, and nanotechnology since the discovery of mechanically exfoliated graphene in 2004, which displayed different properties from its 3D graphite counterpart<sup>9</sup>. The 2D materials platform offers unique access to novel physical, electronic, and chemical properties due to electron confinement in two dimensions. The large portfolio of 2D materials with attractive vibrational, electronic, magnetic, and topological properties makes them interesting for applications in electronics/optoelectronics, spintronics, piezoelectrics, thermoelectrics, electrocatalysis, photocatalysis, photovoltaics, batteries, supercapacitors, sensing platforms and emerging quantum devices as illustrated in Fig. 2.1.<sup>10</sup> In particular, atomically-thin 2D materials have become the focus of nanoelectronics research because of their intriguing mechanical and electronic properties. Their ultrathin nature makes them resilient to short channel effects while having high mechanical flexibility with the absence of dangling bonds.

### 2.2 Graphene

Graphene is the most studied 2D layered material partially because it is the first material to be realized in 2D and most importantly due to its remarkable properties, including ultrahigh room-temperature carrier mobility, quantum Hall effect, ultrahigh specific surface area, high Young's modulus, excellent optical transparency, and excellent electrical and thermal conductivities.<sup>11</sup> Graphene, shown in Fig. 2.2, is a one-atom thick, 2-D sheets of  $sp^2$ -hybridized

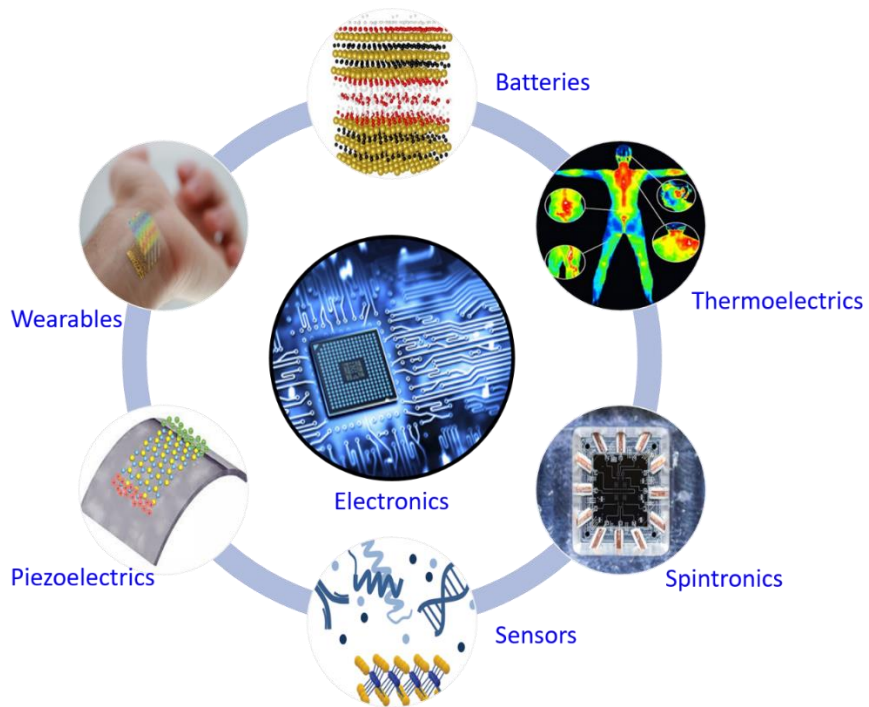


**Figure 2.1.** Schematic diagram highlighting some applications of 2D materials.

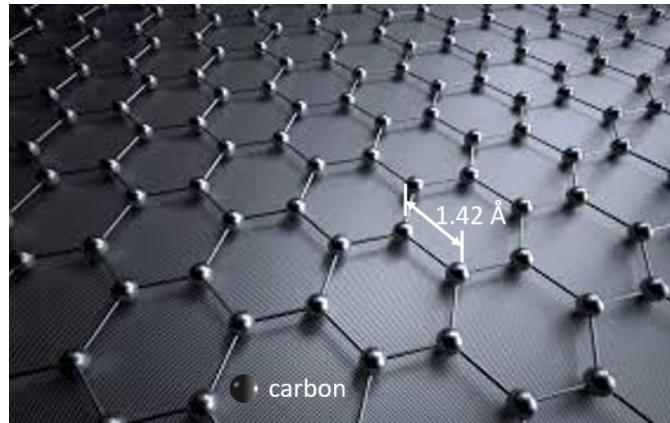


**Figure 2.2.** Schematic diagram illustrating the crystal structure of graphene with a C-C interatomic distance of 1.42 Å.

carbon atoms arranged on a honeycomb structure made of hexagons with a C-C distance of  $\sim 1.42$  Å. Structurally, graphene can be stacked to form 3-D graphite with each layer separated by van der Waals forces, rolled to form 1-D-nanotubes having only hexagons, and wrapped to form 0-D-fullerenes with the introduction of pentagons that create curvature defects. Charge transport in graphene is characterized as ballistic, with nearly massless Dirac fermions traveling at  $\sim 1/300$  of the speed of light <sup>11</sup>, leading to electron mobility in excess of  $10^5$  cm<sup>2</sup> V<sup>-1</sup>s<sup>-1</sup> at room temperature <sup>12,13</sup>. The Dirac fermions behave in unusual ways when compared to ordinary electrons when subjected to magnetic fields, which results in new physical phenomena such as the anomalous integer quantum Hall effect (IQHE) that can be observed at room temperature. Besides the unusual properties, graphene can be chemically and/or structurally modified to change its functionality. Although the properties of graphene can be tuned via chemical and structural functionalization, the lack of sizeable bandgap limits its application logic devices. The new physics and phenomena discovered in graphene serves, however, as a foundation in the exploration of other ultrathin 2D nanomaterials for new physics and complementary functionalities.

### 2.3 Transition Metal Dichalcogenides (TMDs)

Beyond graphene, there is a wide spectrum of 2D electronic materials that range from insulators to semiconductors to metals and even to superconductors. Fig. 2.3 shows the selection of possible 2D layered materials from the periodic table. Prominent in the emerging class of atomically-thin 2D materials are the transition metal dichalcogenides (TMDs), with chemical formulas of MX<sub>2</sub>, where M represents the transition metal (e.g., Mo, W, Pd, Pt) and X represents the chalcogenide (e.g., S, Se, Te). TMDs exhibit a unique combination of atomic-scale thickness, direct bandgap, strong spin-orbit coupling and favorable electronic and mechanical properties, which make them interesting for fundamental studies and for applications in high-end electronics,



spintronics, optoelectronics, energy harvesting, and flexible electronics. TMD semiconductors, such as MoS<sub>2</sub>, WSe<sub>2</sub>, exhibit unique electrical and optical properties that evolve from the quantum confinement and surface effects that arise during the transition of an indirect bandgap to a direct bandgap.<sup>5</sup> This tunable bandgap in TMDs is accompanied by a strong photoluminescence (PL) and large exciton binding energy, making them promising candidates for a variety of optoelectronic devices, including photovoltaics, photodetectors, light-emitting diodes, and phototransistors.<sup>14</sup>

Apart from tuning the bandgap, the functionality of TMDs can be expanded by stacking together sheets of dissimilar 2D materials to achieve vertical heterostructures which allows for the realization of unique properties that cannot be obtained otherwise.<sup>15</sup> For example, several new electronic/optoelectronic devices such as tunneling transistors, barristers, photodetectors, LEDs and flexible electronics can be created by exploiting novel properties such as band alignment, tunneling transports, and strong interlayer coupling in these vdW heterostructures.<sup>16-19</sup> In addition, polymorphic phase transitions in van der Waals layered materials have received recent widespread interest due to their ability for tuning their structural and quantum states, which allows for investigating their novel topological and Weyl states, and applications in fields ranging from electronic and optical/quantum devices to electrochemical catalysis.<sup>20</sup> For example, structural transformation of semiconducting 2H-MoS<sub>2</sub> can achieve a metallic 1T phase, which can be used as the contact in homojunction devices to reduce Schottky barriers in metal-semiconductor interface.<sup>21 22</sup> The sheer number of the available 2D materials offers a diversified portfolio of new science and discovery at the fundamental atomic limit.

MoS<sub>2</sub> has been one of the most studied layered TMDs due to the wide-spread availability

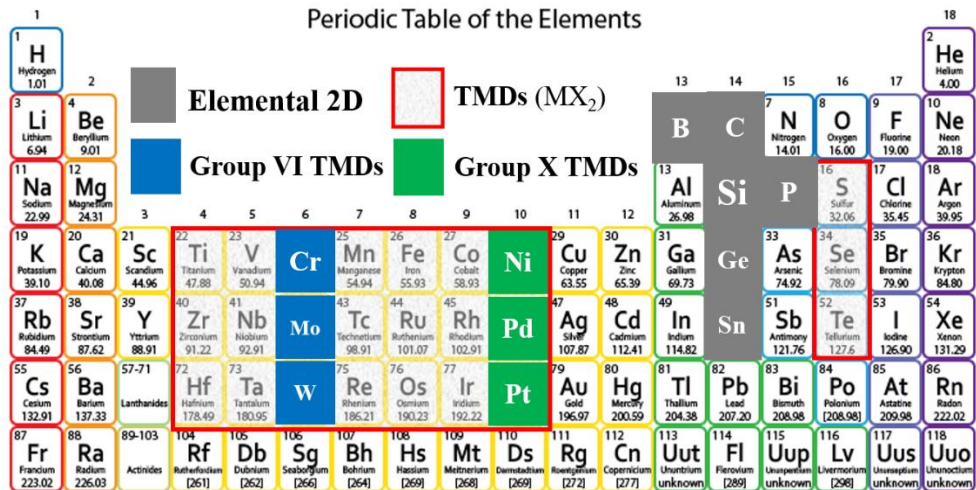
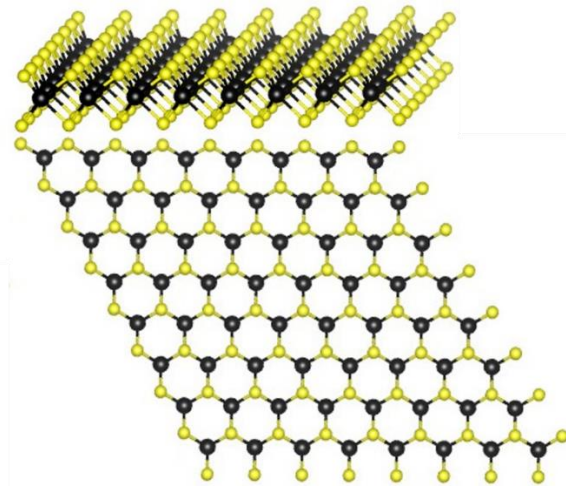


Figure 2.3. Periodic table highlighting possible layered 2D materials.

of molybdenite and its tunable band gap of  $\sim 1.2 - 1.9$  eV. It tackles the gapless problems of graphene, thus making it possible for MoS<sub>2</sub> to be used in the next generation switching and optoelectronic devices. In contrast to graphene, each MoS<sub>2</sub> layer consists of three atomic layers, in which Mo atoms are sandwiched between two S- layers, which are separated by van der Waals forces. One of MoS<sub>2</sub> unique features is their capability to form different crystal polytypes. MoS<sub>2</sub> crystallizes with four different crystal structures, that is, 2H, 1T, 1T', and 3R, depending on the different coordination models between Mo and S atoms and/or stacking orders between layers (Fig. 2.4). The 2H structure has an atomic stacking sequence (S–Mo–S') ABA in a hexagonal closed packing symmetry and trigonal prismatic coordination. The 1T structure has an octahedral coordination with tetragonal symmetry in which each layer has an atomic stacking sequence of (S–Mo–S') ABC. The distorted 1T (denoted as 1T') structure also has an octahedral coordination, similar to that of the 1T structure, but it contains a superstructure in each layer. The 3R structure has an ABC-ABC stacking order where A, B, and C layers are in the same direction. It maintains broken inversion symmetry from monolayer to bulk, revealing strong valley and spin polarizations that are not achieved in natural 2H MoS<sub>2</sub>. The 2H-type MoS<sub>2</sub> is dominant because it is thermodynamically stable in nature. In the manner of the 3R-structure, the 2H-MoS<sub>2</sub> is found to be semiconducting. The T-phases are metallic, with the 1T'-MoS<sub>2</sub> reported to be a Weyl semimetal, a quantum spin Hall insulator, and a superconductor. So far, MoS<sub>2</sub> has achieved progress in nanodevices, stretchable electronics, energy conversion and storage and hydrogen evolution reaction (HER).<sup>23</sup>

## 2.4 Noble Transition Metal Dichalcogenides (NTMDs)

In exploring the layered 2D material landscape beyond graphene, extensive attention has been drawn to group-6 TMDs - MoS<sub>2</sub>, MoSe<sub>2</sub>, WS<sub>2</sub>, WSe<sub>2</sub> - while TMDs with group-10 transition



**Figure 2.4.** Side and top view of the crystal structure of monolayer MoS<sub>2</sub>.

metals of Pd, Ni and Pt, have been under- or unexplored<sup>4,14,24-32</sup>. Only few reported experimental works are available on PtS<sub>2</sub> and PtSe<sub>2</sub> with no experimental evidence on the exfoliation of palladium dichalcogenides (PdX<sub>2</sub>)<sup>33-36</sup>. Group-10 TMDs, such as PtS<sub>2</sub> and PtSe<sub>2</sub>, have demonstrated high carrier mobility, widely tunable bandgap, and air-stability for electronic and optoelectronic applications.<sup>33,37</sup> They have shown strong interlayer coupling, with each layer exhibiting distinct layer-dependent electronic, optical, thermal, mechanical and vibrational properties. The strong interlayer interaction is due to the strong hybridization between the d-orbital of the transition metals and the p-orbital of the chalcogen atoms. This is in contrast with group-6 TMDs (MoS<sub>2</sub>, WS<sub>2</sub>), which have weak interlayer interaction, thus, moderately layer-dependent bandgap.<sup>5,38</sup> Group-7 TMDs such as ReS<sub>2</sub>, whose monolayer band gap is similar to its bulk counterpart due to the very weak interlayer interactions.<sup>39</sup> The influence of the transition metal group on layer interactions has been established to be due to the strong dependence of the coordination structure of TMDs on the d-electron number of the transition metal.<sup>40,41</sup>

Layered PtS<sub>2</sub> and PtSe<sub>2</sub> have a wide-tunable indirect bandgap of 0.25 eV – 1.6 eV, and ~0 eV – 1.2 eV, respectively, from bulk down to monolayer, which covers a wide part of the electromagnetic spectrum from visible to mid-infrared.<sup>33,35</sup> In addition, field-effect transistors based on PtS<sub>2</sub> have shown high phonon-limited mobility ~1107 cm<sup>2</sup>/Vs at room temperature and high air-stability, which makes them interesting for electronic applications.<sup>33,42</sup> Furthermore, few-layer PtS<sub>2</sub> has been used to fabricate phototransistors that show high photoresponsivity and photoconductive gain.<sup>37</sup> Another case is few-layer PtSe<sub>2</sub> infrared photodetectors with high photoresponsivity and fast response.<sup>35</sup> Moreover, heterostructures of PtS<sub>2</sub>/PtSe<sub>2</sub> built by the sequential sulfurization and selenization of Pt thin-films can be used to assemble photodiodes with high photoresponsivity, external quantum efficiency, and fast respond speed.<sup>43</sup> Besides electronics

and optoelectronics, the existence of symmetry-protected type-II Dirac fermions have been predicted in bulk PtSe<sub>2</sub>.<sup>44</sup> This discovery leads to the realization of exotic physical properties, such as chiral anomaly.<sup>45</sup> The origin of the fermions is understood to be related to the structural symmetry of PtSe<sub>2</sub> ( $P\bar{3}m1$ ). Similarly, group-10 TMDs such as PtTe<sub>2</sub> and PdTe<sub>2</sub> have been proposed to be a type-II Dirac fermions.<sup>46</sup>

## 2.5 Pentagonal building blocks of 2D materials

The most dominant motif found as the basic building block in 2D materials is the hexagonal/honeycomb structure, which includes graphene, MoS<sub>2</sub>, and black phosphorus. These hexagonal lattices form a hexagonal tiling when projected to a plane, similar to honeycomb structures. Pure pentagonal tilings in 2D materials are rare and have only been recently predicted theoretically, but have remained unexplored experimentally.<sup>47-49</sup> The pentagons are usually considered as topological defects or geometrical frustrations, as stated in the well-known “isolated pentagon rule” (IPR).<sup>50</sup> Mathematically, pentagon tessellation has been a century-old problem because the internal angle of a regular pentagon, 108°, is not a divisor of 360°. Triangles, squares and hexagons are the only regular shapes which tessellate by themselves. By relaxing some of the constraints on regular tilings, it has been found that there are in fact no more than 15 possible monohedral convex pentagonal tilings made of distorted pentagons.<sup>51</sup> Out of these, only the Cairo pentagonal tiling has been found to exist in 2D materials. Unlike the hexagonal structure, most of the predicted pentagonal 2D materials, including penta-graphene and penta-SnS<sub>2</sub>, are buckled or puckered in a regular corrugated manner to maintain symmetry.

### 2.5.1 Penta-graphene

Penta-graphene, a 2D carbon allotrope, was recently proposed from first-principle calculations and confirmed to be thermodynamically and mechanically stable.<sup>47</sup> Penta-graphene is

composed entirely of carbon pentagons which resembles the Cairo pentagonal tiling different from graphene which forms a honeycomb structure (Fig. 2.5). Penta-graphene consists of both  $sp^3$  and  $sp^2$  carbons which can withstand temperatures as high as 1000 K.<sup>47</sup> Structurally, penta-graphene can be rolled to form pentagon-based nanotubes which are semiconducting, and can be stacked to achieve stable 3D twin structures. The unique atomic configuration coupled with the buckled structure results in a large band gap of  $\sim 3.25$  eV, an unusual negative Poisson's ratio and ultrahigh mechanical strength, which are interesting for flexible device applications. In addition, penta-graphene demonstrates remarkably lower thermal conductivity ( $\kappa$ ) compared to graphene due to the lower phonon group velocities and fewer collective phonon excitations.<sup>52</sup> The extremely low  $\kappa$  makes penta-graphene a potential candidate for 2D thermoelectrics.

### 2.5.2 Penta-SnX<sub>2</sub> and others penta-2D materials

The realization of unusual properties in penta-graphene inspired researchers to discover other new 2D pentagonal materials such as penta-SnX<sub>2</sub>, penta-CN<sub>2</sub>, penta-CB<sub>2</sub>, and penta-B<sub>x</sub>N<sub>y</sub>.<sup>49,53</sup> For example, penta-SnS<sub>2</sub> is composed of pentagonal rings and has been theoretically predicted to be a room-temperature 2D quantum spin Hall (QSH) insulator with sizable and nontrivial band gaps (0.12 – 0.22 eV). Unlike the penta-SnX<sub>2</sub> which display a square lattice, hexa-SnX<sub>2</sub> 2D crystals follow a symmetry group -  $P\bar{3}m1$  (point group  $D_{3D}$ ) and display the CdI<sub>2</sub>-type structure with a hexagonal lattice. Another example is the Si-based pentagonal monolayers p-SiX (X = C, and N) which are indirect semiconductors with band gaps of 2.35 and 4.98 eV, respectively.<sup>54</sup> They have been reported to have high carrier mobilities ( $\sim 2500$  cm<sup>2</sup>V<sup>-1</sup>s<sup>-1</sup>) and mechanical flexibility which indicate that p-SiX can be used as flexible electronic devices.

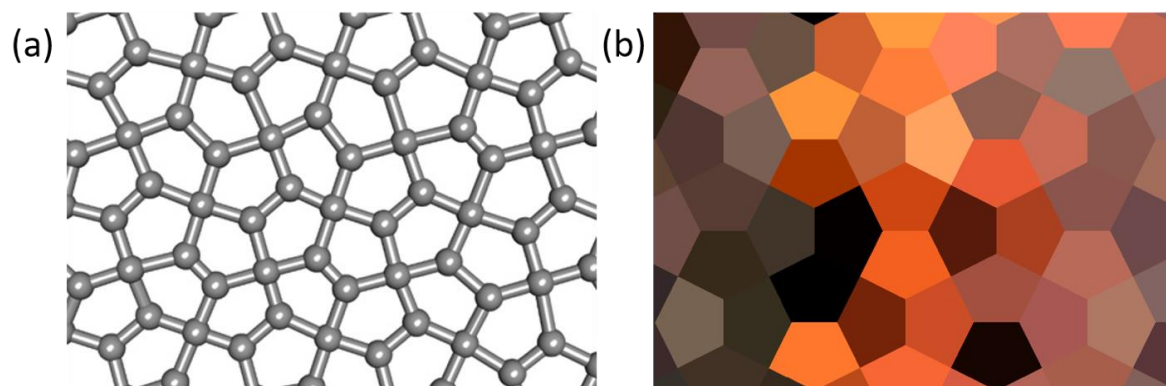


**Figure 2.5.** (a) Crystal structure of penta-graphene which matches the Cairo pentagonal tiling illustrated in (b).



### 2.5.3 Pentagonal group-10 TMDs

The first report on pentagonal structures in TMDs shows that unlike other 2D TMDs which adopt the ordinary 2H or 1T configuration, in PdS<sub>2</sub> each Pd atom can only bind to four rather than six S atoms, leading to the formation of a novel pentagonal structure.<sup>36</sup> This new PdS<sub>2</sub>-type structure is the most thermodynamically favorable with planar tetra-coordinate Pd atoms and covalent S–S bonds. Interestingly, PdS<sub>2</sub> exhibits a wide-tunable bandgap from ~0 eV to 1.6 eV (bulk to monolayer) with large carrier mobilities. Similarly, PdSe<sub>2</sub> has been predicted to have a pentagonal crystal structure of the PdS<sub>2</sub>-type with strong interlayer coupling and an extraordinarily high carrier mobility.<sup>55</sup> As shown by the side view and projected top view of a 2D PdSe<sub>2</sub> monolayer in Fig. 2.6a, it consists entirely of pentagonal rings with the vertices in a slightly asymmetrical boat conformation, which is similar to the puckered structure of BP (Fig. 2.6b) that has hexagonal rings. Each Pd atom binds to four Se atoms in the same layer, and two neighboring Se atoms can form a covalent Se–Se bond. To the best of our knowledge, this pentagonal conformation has not yet been experimentally reported for any 2D materials structure, including graphene, other elemental 2D materials (also called Xenos), and TMDs. In general, the realization of these 2D buckled pentagonal materials with low symmetry could open the possibility for future optoelectronic, piezoelectric, spintronic, and valleytronic applications.

## 2.6 Anisotropy in buckled and puckered 2D materials

Owing to its high charge-carrier mobility at room-temperature, tunable direct-bandgap and unique in-plane anisotropic structure, black phosphorus (BP) has been received a lot of attention since its rediscovery early 2014.<sup>56</sup> Like graphene and MoS<sub>2</sub>, black phosphorus has a hexagonal

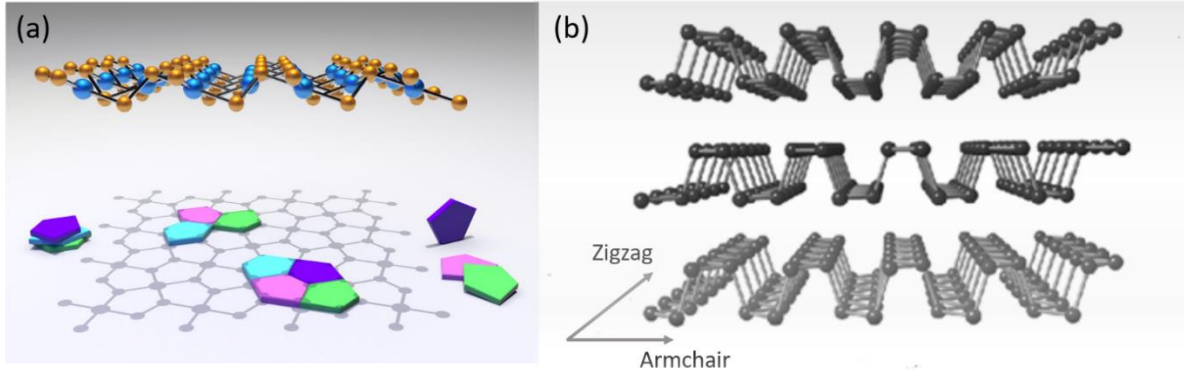


**Figure 2.6.** (a) Side and top view of the crystal structure of PdSe<sub>2</sub>. (b) Puckered structure of black phosphorus.

crystal structure, however, it is buckled and corrugated differently along the x-y directions (Fig 2.6b). Puckering in BP renders exotic properties of the in-plane anisotropic response to external stimulations which provides a new degree of freedom to explore in 2D materials. Bulk BP is a layered orthorhombic crystal structure with the space group  $Cmca$  (64) with individual layers stack together through vdW forces at a separation distance of 5.4 Å. Each BP monolayer is composed of parallel puckered double layers in which each phosphorus atom is covalently bonded to three other phosphorus atoms. Apart from its application in electronic and optoelectronic devices owing to its widely tunable band gap variation from 0.3 to 1.5 eV, BP has the lowest thermal conductance of layered materials (graphene, TMDs, *h*-BN) which makes it a promising thermoelectric nanomaterial.<sup>57</sup> Also, BP belongs to a group of materials known as topological insulators with highly anisotropic magnetic properties, as both diamagnetic and paramagnetic behavior can be observed depending on the orientation in the magnetic field.<sup>58</sup> In addition, theoretical studies predict that in-plane strains in monolayer BP could substantially modify its electronic band structure, thereby resulting in a dramatic and anisotropic change in the carrier mobility along the zigzag and armchair directions.<sup>59</sup>

Recently, other buckled or puckered 2D materials with hexagonal structure have been theoretically and experimentally reported in elemental 2D materials (also called Xenes) such as silicene, germanene, and stanene.<sup>60,61</sup> In contrast with an isotropic planar hexagonal structure, the buckling breaks the sublattice symmetry, enhances spin-orbit coupling, and allows tuning of a topological quantum phase transition.<sup>62</sup> However, despite their potential importance for device applications, the realization of stable 2D buckled or puckered hexagonal structures of 2D elemental materials including BP, silicene, germanene, and stanene is still a great challenge for practical electronics. Other 2D materials with low-symmetry structures such as group-4 monochalcogenides

(SnS, SnSe), group-6 TMDs (MoTe<sub>2</sub>, WTe<sub>2</sub>) and group-7 TMDs (ReS<sub>2</sub>, ReSe<sub>2</sub>) have known anisotropy due to their asymmetrical, distorted octahedral phase, unlike counterpart hexagonal flat phase structures.<sup>63</sup> The anisotropy introduces in-plane orientation-dependent electron and phonon properties, an additional degree of freedom which can be used to control device performance with crystal orientation for field-effect transistors (FETs), photodetectors, thermoelectric and piezoelectric applications.

## Chapter 3: Atomically-thin van der Waals Heterostructure Built via Dry-Transfer

### 3.1 Introduction

Most 2D materials display a layer-dependent electronic band structure, which allows for the tuning of their electronic properties by changing the number of layers. They are also known for their strong light-matter interactions, which are important for photonic and electronic applications<sup>64-66</sup>. The unique characteristics of these individual 2D materials can be further functionalized by stacking different crystals to form vertical heterostructures. These heterostructures, held together by van der Waals (vdW) forces, allow for the study of exciting interfacial phenomena between the constituents hetero-layers. For example, the interface of vdW heterostructures have exhibited interlayer exciton coupling due to their electron-hole correlation.<sup>67</sup> These interfaces are also great for charge carrier separation, which are the basis of photovoltaics, and phototransistors.<sup>68,69</sup> Unlike traditional 3D systems, vdW heterostructures do not require that the lattice constants match due to the presence of atomically sharp interfaces<sup>15</sup>. As such, they allow for the matching of different 2D crystals to form atomically-thin heterostructures, which have found applications in 2D field effect transistors (FET), memory devices and light-emitting diodes (LED) applications<sup>17,19,67,70</sup>.

In this work, we explore two vdW heterostructures based on exfoliated and CVD-grown few-layers InSe/WSe<sub>2</sub> and MoSe<sub>2</sub>/black phosphorus, built via deterministic dry-transfer process. The heterostructures result in a type-II junction, which displayed a pronounced rectification behavior like that of conventional p-n junction diodes. The current rectification factor obtained is as high as  $\sim 10^2$  in the InSe-WSe<sub>2</sub> device. The electrical characteristics exhibited by the heterostructures can be further tuned via electrostatic gate-control. Our results demonstrate that

atomically-thin devices can form an important component of modern semiconductor devices, including diodes, bipolar transistors, photodiodes, light-emitting diodes, and solar cells.

### 3.2 Deterministic dry-transfer method

Various approaches have been utilized to make vdW heterostructures, which include ones built by sequential epitaxial chemical vapor deposition (CVD) or physical epitaxy<sup>71,72</sup>, and those mechanically-assembled via wet-transfer<sup>73</sup> or dry-transfer methods<sup>74,75</sup>. The deterministic dry-transfer method developed by Castellanos-Gomez et al<sup>74</sup>, is a flexible technique for heterostructure assembly, allowing for the control of stacking orientation with clean interfaces free from chemical contaminants. This technique is amenable to build heterostructures on both exfoliated and vapor deposited samples to form exfoliated-exfoliated and CVD-exfoliated heterojunctions. The transfer setup was replicated at CNMS for this dissertation work. Fig. 3.1 shows an optical image of the setup. The setup includes a Canon DSLR 500D camera with additional lenses to increase the power of the objectives. The camera is connected to a monitor for live viewing and it is equipped with a memory device for recording videos and photos. The stage is lit with a lamp for illumination. To ensure that 2D flakes can be transfer deterministically, with minimal wobbling, the setup has micromanipulators with magnetic base to control the stacking process. This all dry-transfer deterministic process was used to build InSe-WSe<sub>2</sub> and MoSe<sub>2</sub>-BPh heterostructures, illustrated in the schematic shown in Fig. 3.2. The first step in the process is to exfoliate or deposit the bottom material on a desired substrate. Then, using a piece of Scotch tape, the top material is exfoliated on a transfer agent polydimethylsiloxane (PDMS) polymer. A glass slide is used as a mechanical support for the PDMS polymer, and to provide transparency that allows the transfer process to be seen through the aid of an optical microscope. Using the optical microscope, the alignment of the

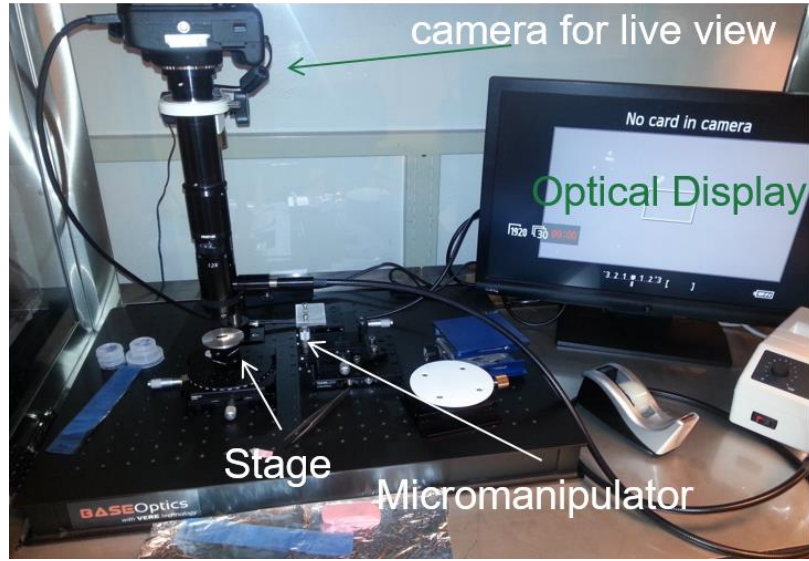


**Figure 3.1.** Optical image of the deterministic dry-transfer setup.

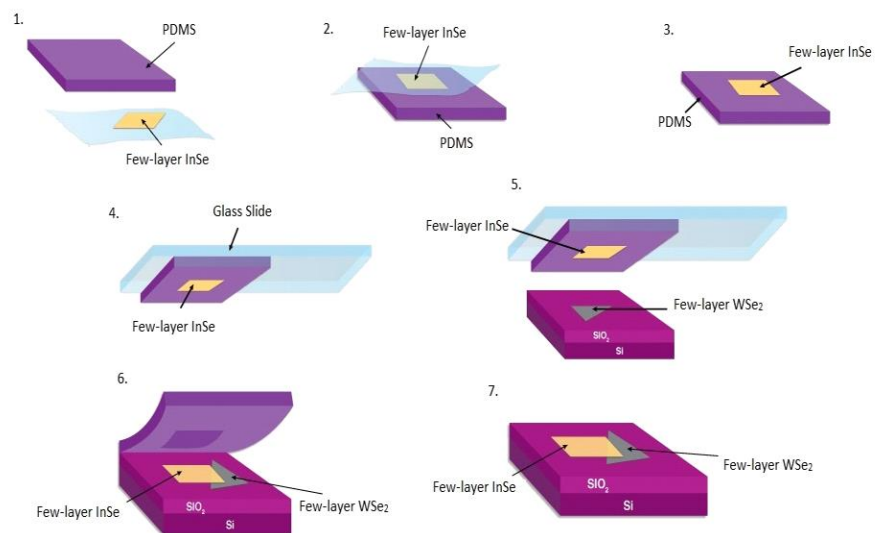


**Figure 3.2.** Schematic illustration of the steps involved in the deterministic transfer of few-layers InSe onto a WSe<sub>2</sub> flake.



top and bottom layer material can be precisely controlled to ensure that there is an overlapping region – vertical heterojunction - between the two materials. This allows for the characterization of the individual materials constituting the heterostructures as well as the junctions. The formation of a contamination-free heterostructure are very useful for making different high-performance electronic devices.

### 3.3 Results

The formation of heterojunctions requires understanding of the individual 2D material to create heterostructures with predefined qualities. This includes engineering their band alignment and interfacial properties. Here, we demonstrate atomically-thin p-n junctions built via deterministic dry-transfer method. Few-layer tungsten diselenide ( $\text{WSe}_2$ ) and black phosphorus (BPh) were selected as p-type materials due to their preferential hole conduction<sup>6,76</sup>, while few-layer indium selenide (InSe) and monolayer molybdenum diselenide ( $\text{MoSe}_2$ ) were selected as n-type materials due to their preferential electron conduction<sup>4,77,78</sup> to form InSe- $\text{WSe}_2$  and  $\text{MoSe}_2$ -BPh heterostructures. The heterojunctions formed at the interfaces are of type-II junction, with different band alignments. We observed a strong current-rectifying junction behavior in the heterostructures, with gate tunable electrical properties. Thus, providing a solid foundation for their incorporation of such heterojunctions in complex electronic circuitry, including logic gates, solar cells and amplifiers.

#### 3.3.1 InSe- $\text{WSe}_2$ Heterostructure

An InSe- $\text{WSe}_2$  heterostructure was built using the dry-transfer method illustrated in Fig. 3.2. As shown in Fig. 3.3a, few-layer  $\text{WSe}_2$  flake with  $\sim 7$  nm thick was first exfoliated on to a

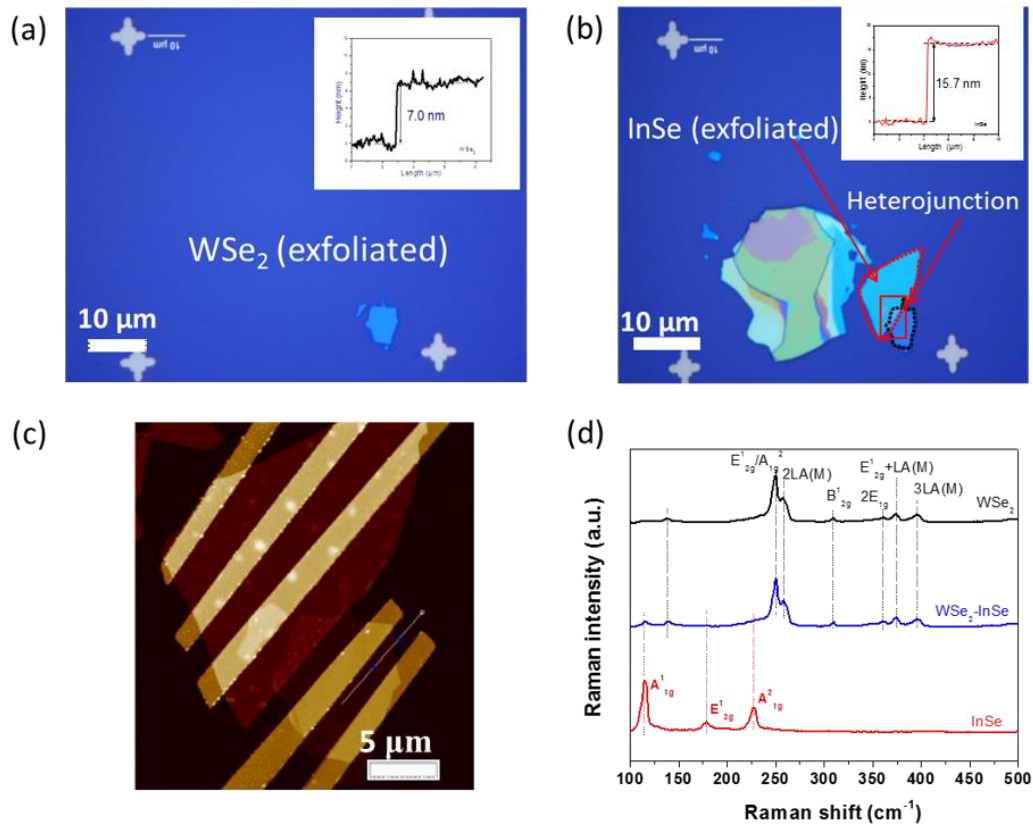


**Figure 3.3.** (a) Optical image of the first flake (few-layer WSe<sub>2</sub>) mechanically exfoliated on the Si/SiO<sub>2</sub> substrate. (inset): The thickness profile of few-layer WSe<sub>2</sub> corresponding to the white line in (2d). (b) Optical image after the transfer of the second flake (few-layer InSe) on the WSe<sub>2</sub> flake to form a heterojunction. (b) Inset: The thickness profile of few-layer InSe corresponding to the red line in (2c). (c) The atomic force microscopy (AFM) image of the FET device. (d) Raman spectra for WSe<sub>2</sub>, the heterostructure, and InSe arranged in a stacking manner.

SiO<sub>2</sub> substrate. Fig. 3.3b shows the optical image of the heterostructure after few-layers of InSe had been transferred on the WSe<sub>2</sub> flakes. The WSe<sub>2</sub> flake is indicated by the black dotted lines and the InSe flake is indicated by the red dotted lines. The inset image is the profile of the thickness of the InSe flake (~15 nm) was taken from atomic force microscopy (AFM) measurements shown in Fig. 3.3c. The Raman spectra of the few-layers WSe<sub>2</sub>, InSe, and the heterojunction are shown in Fig. 3.3d. The Raman spectra of the heterojunction is a composite of the individual Raman spectra of InSe and WSe<sub>2</sub>. There is no visible new peak, which implies the formation of a contaminant-free heterojunction device. The spectra obtained for the individual materials, InSe and WSe<sub>2</sub>, are similar to those reported in literature<sup>79,80</sup>.

To characterize the electrical properties of the InSe-WSe<sub>2</sub> heterostructure, a two-terminal field-effect transistor (FET) configuration was used as shown in Fig. 3.4a, with Ti/Au (5nm/30nm) metal contacts. Two parallel contacts were made on each of InSe and WSe<sub>2</sub> to characterize their individual properties, while the nearest two contacts to the junction were used to characterize the performance of the heterojunction. The schematic of the suggested band alignment formed at the junction of this heterostructure is shown in Fig. 3.4b, illustrating the formation of a type-II heterojunction. The type of heterojunction formed is dependent on the electronic characteristics of the adjacent materials. A typical example is the p-n junction formed by stacking a p- and n-type semiconductors, which is the fundamental building block for most modern electronic devices. In conventional 3D semiconductor systems, the p-n junction is achieved by doping silicon to achieve either excess electrons or holes, thus constituting an homojunction (n-Si/p-Si). In 2D systems, however, doping is not required, as the crystals can be inherently p-, n-type or ambipolar. Thus, eliminating an additional processing step required for traditional 3D heterojunctions.

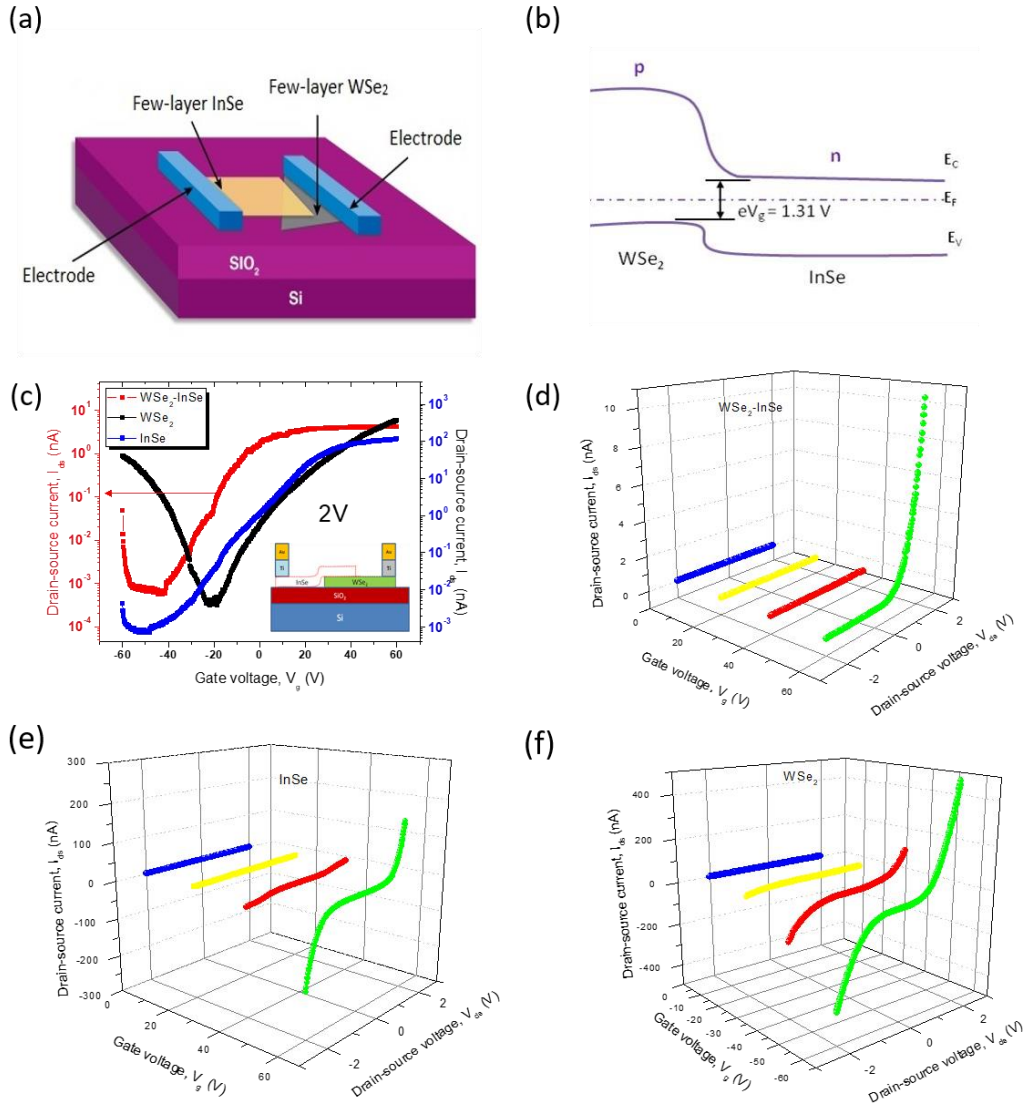


**Figure 3.4.** (a) Schematic of the WSe<sub>2</sub>-InSe heterojunction field effect transistor (FET) device. (b) The suggested band alignment for few-layer WSe<sub>2</sub> and InSe flakes showing type-II heterojunction. (c) The transfer characteristics of the WSe<sub>2</sub>, InSe and WSe<sub>2</sub>-InSe FET device with 2 V source-drain bias (in logarithmic scale). Inset: Schematic of the WSe<sub>2</sub>-InSe field effect transistor device. The left y-axis corresponds to the red (InSe- WSe<sub>2</sub>) curve, while the right y-axis corresponds to the blue (InSe) and black (WSe<sub>2</sub>) curves. (d) Output characteristics of the FET based on WSe<sub>2</sub>-InSe heterostructures at different gate bias. (e-f) Output characteristics of InSe and WSe<sub>2</sub>, at various gate bias, showing symmetric behaviors.

The transfer characteristics of the InSe, WSe<sub>2</sub> and the heterojunction device at a source-drain bias of 2V are shown in Fig. 3.4c. The transfer curve of the InSe device, shown in the blue curve of Fig. 3.4c, highlights a predominant n-type behavior as expected, with current on/off ratio of 10<sup>4</sup> and mobility of 0.03 cm<sup>2</sup>V<sup>-1</sup>s<sup>-1</sup>. WSe<sub>2</sub>, on the other hand, shows an ambipolar behavior, with current on/off ratio of 10<sup>4</sup> and electron mobility of 0.09 cm<sup>2</sup>V<sup>-1</sup>s<sup>-1</sup>. The transfer characteristics of the heterojunction device displays an ambipolar transport with preferential electron conduction. As suggested by the band-alignment diagram in Fig. 3.4b, the offset at the conduction band in Fig. 3.4b is much more than that at the valence band, suggesting that the junction will favor more electron transport than hole transport. This is because few-layer WSe<sub>2</sub> exhibits an ambipolar characteristics. Similar observations were made in other devices that were fabricated. The use of p-type WSe<sub>2</sub>, will reduce the electron transport in this heterostructure in favor of more hole transport.

The output characteristics of InSe and WSe<sub>2</sub> are shown in Fig. 3.4(e-f) in the supplementary information. The I<sub>ds</sub>-V<sub>ds</sub> curves at various gate bias show a symmetric characteristic behavior about the drain voltage. However, as shown in Fig. 3.4d, the atomically thin WSe<sub>2</sub>-InSe heterojunction displays a highly asymmetric current-voltage characteristic, typical of type II junctions with a rectification factor of about ~65. This value could be improved by using a preferentially p-type WSe<sub>2</sub>. The origin of this electrical rectification is the quantum tunneling charge transport across the atomically thin junction, rather than the semi-classical drift and diffusion of charge carriers through the depletion regions at junctions. This rectifying behavior, which allows for the selective flow of charge carriers in only one direction, is the basis of electronic devices. More so, owing to the atomically thin nature of 2D heterostructures, their electronic properties can be modified using

external field effect. As shown in Fig. 3.4d, the rectifying behavior can be tuned with different gate bias.

### 3.3.2 Black Phosphorus-MoSe<sub>2</sub> Heterostructure

Similar to WSe<sub>2</sub>, black phosphorus exhibits stronger hole conduction, which can be coupled with n-type MoSe<sub>2</sub> to form a p-n junction. Fig. 3.5a shows the optical image of a few-layer black phosphorus and monolayer molybdenum diselenide (MoSe<sub>2</sub>) heterostructure device formed using the dry-transfer technique. Monolayer MoSe<sub>2</sub> was grown via chemical vapor deposition, while black phosphorus was mechanically exfoliated using a piece of Scotch tape. The black and red dotted lines in Fig. 3.5a are for the height profiles of black phosphorus (black) and MoSe<sub>2</sub> (red) shown in Fig. 3.5b determined using AFM. The thickness of monolayer MoSe<sub>2</sub> is ~0.9 nm, while that of black phosphorus is ~37 nm. The strong photoluminescence peak at 1.53 eV shown in Fig 3.5c. confirms the thickness of the MoSe<sub>2</sub> flakes to be that of a single layer. Monolayer MoSe<sub>2</sub> exhibits a direct band gap, with multilayers exhibiting an indirect band gap<sup>80</sup>. The Raman spectra of monolayer MoSe<sub>2</sub>, black phosphorus and the heterojunction are shown in Fig. 3.5d. A strong Raman peak at ~238 cm<sup>-1</sup> can be observed for monolayer MoSe<sub>2</sub>, representing the A<sup>1</sup><sub>g</sub> peak<sup>81</sup>. The peaks at ~360 cm<sup>-1</sup>, 437 cm<sup>-1</sup> and 464 cm<sup>-1</sup> for the few-layer black phosphorus represents the A<sup>1</sup><sub>g</sub>, B<sub>2g</sub> and A<sup>2</sup><sub>g</sub> peak vibrational mode, respectively<sup>82</sup>. The Raman spectra at the heterojunction is a result of the juxtaposition of the spectra from the individual material, as observed in the InSe-WSe<sub>2</sub> heterostructure. The absence of other peaks in the heterostructure Raman spectra suggests that the junction formed is contaminant-free.

The electrical characteristics was measured via a field-effect transistor (FET) architecture. Fig. 3.6a shows the optical image of the MoSe<sub>2</sub>-black phosphorus heterostructure. The transfer characteristics for the individual materials forming the heterostructure are shown in Fig. 3.6b, with

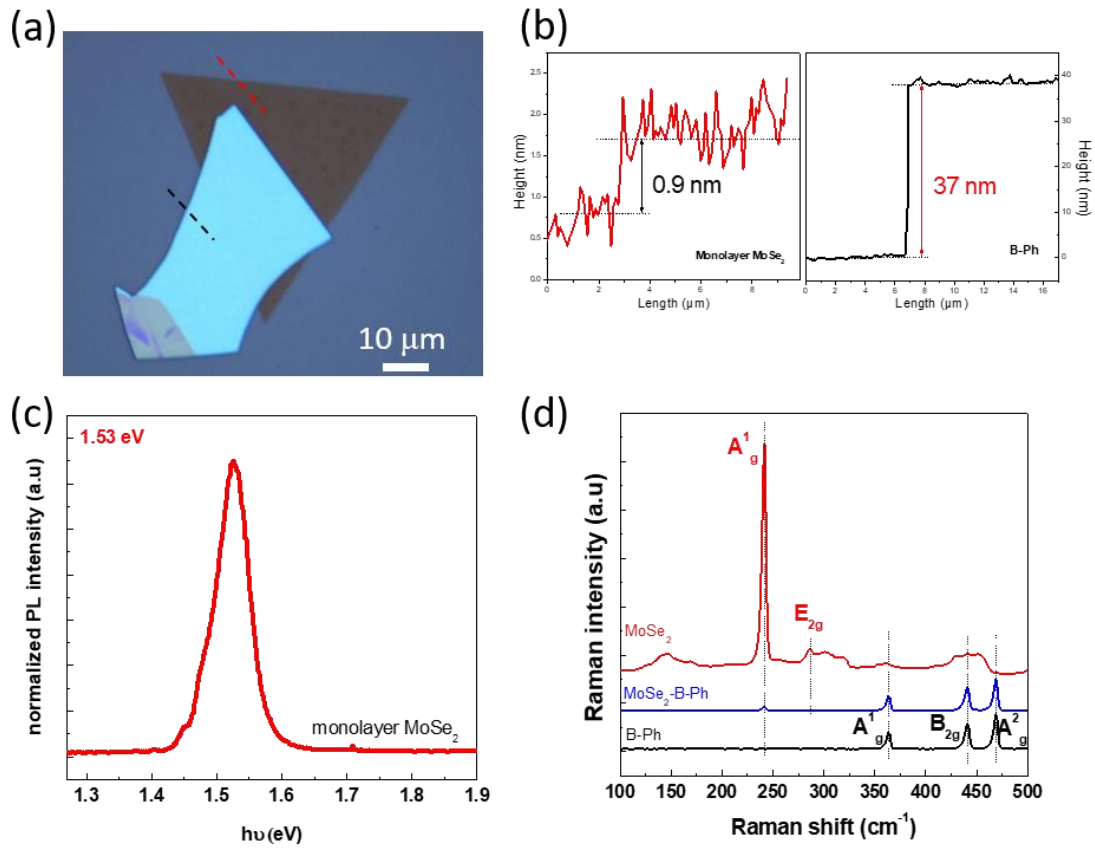


**Figure 3.5.** (a) Optical image of MoSe<sub>2</sub>-black phosphorus heterostructure. The inserted lines are where AFM heights profile in (b) were taken. The red and black profiles are for monolayer MoSe<sub>2</sub> and black phosphorus, respectively. (c) Photoluminescence spectra of monolayer MoSe<sub>2</sub>, with signature emission at ~1.53 eV. (d) Raman spectra of MoSe<sub>2</sub> and black phosphorus and the heterostructure, showing the presence of individual peaks in the heterostructure formed.

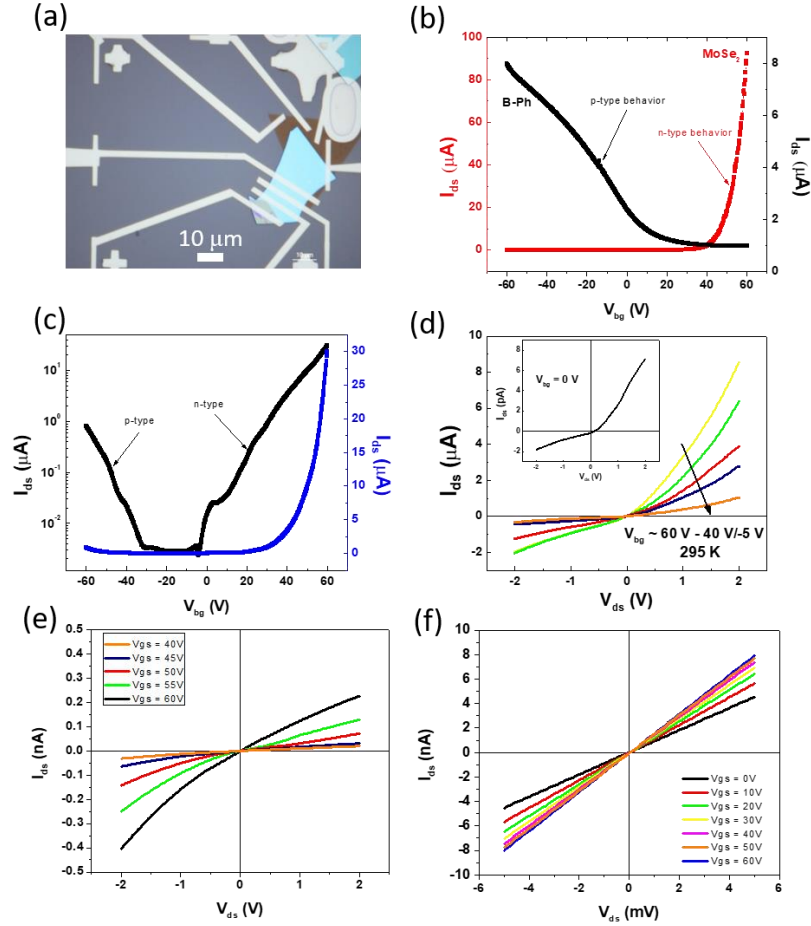


**Figure 3.6.** (a) Optical image of MoSe<sub>2</sub>-black phosphorus heterostructure, with electrical contact of Ti/Au. (b) Transfer characteristics of monolayer MoSe<sub>2</sub> and black phosphorus, showing predominant n-type and p-type behaviors, respectively. The left y-axis corresponds to the red (MoSe<sub>2</sub>) curve, while the right y-axis corresponds to the black (black phosphorus) curve. (c) Transfer curve of the heterostructure, displaying both n-type and p-type conduction typical of a p-n junction. The left y-axis corresponds to the black (logarithmic scale) curve, while the right y-axis corresponds to the red (linear scale) curve. (d) Output characteristics of the heterojunction with a rectifying behavior at different gate bias. Inset shows the output curve at zero gate bias. (e) Output characteristics of monolayer MoSe<sub>2</sub> and (f) black phosphorus, at various gate bias, showing linear-symmetric behaviors.



black-phosphorus having an extraordinary hole mobility of around  $336 \text{ cm}^2\text{V}^{-1}\text{s}^{-1}$ , and monolayer  $\text{MoSe}_2$  showing preferential electron conduction. The combination of this n-type  $\text{MoSe}_2$  and p-type black phosphorus forms a p-n junction evident by the transfer characteristics of the heterojunction shown in Fig. 3.6c. The ambipolar characteristics of this heterojunction allows for both electron and hole conduction. The output curve at different gate bias for  $\text{MoSe}_2$  and black phosphorus are shown in Fig. 3.6(e-f) respectively. Both display a characteristic linear-symmetric behavior about positive and negative drain voltages. The output current-voltage characteristics of the heterojunction, shown in Fig. 3.6d, confirms the presence of the rectifying behavior at the junction, with carrier conduction preferential in one direction. The output curve at zero gate bias is shown as inset in Fig. 3.6d. The current rectification factor is  $\sim 4.5$ . Compared to the  $\text{InSe-WSe}_2$  heretojunction, the rectification factor is smaller, which is thought to be due to the huge difference in the relative thickness of the black phosphorus (39 nm) in contrast of the monolayer  $\text{MoSe}_2$  (0.9 nm). As a juxtaposition,  $\text{InSe}$  and  $\text{WSe}_2$  has comparative thickness of 15.7 nm and 7.0 nm, respectively.

### 3.4 Conclusion

We have demonstrated the rectifying behavior at the p-n junction formed by different heterostructures, namely  $\text{WSe}_2\text{-InSe}$  and  $\text{BPh-MoSe}_2$  heterojunctions. The heterojunctions were formed by the stacking of two dissimilar materials by an all dry-transfer process, with the aid of a micromanipulator to ensure that the top layer material forms an overlap (a junction) with the bottom material. This method is amenable to both exfoliated and CVD-grown samples. The band alignment of the p-n junction formed is of the type II heterojunction. The transfer characteristics show  $\text{InSe}$  and  $\text{MoSe}_2$  with a predominantly n-type behavior, while  $\text{WSe}_2$  shows ambipolar behavior, and  $\text{BPh}$  displayed n-type behavior. The I-V curve at the atomically thin  $\text{WSe}_2\text{-InSe}$  and

BPh-MoSe<sub>2</sub> heterojunctions show gate-tunable rectifying behavior indicating the formation of p-n junction. The rectification factor obtained for these heterojunctions is as high as 20. The formed atomically p-n heterojunctions could have potential applications in modern electronics and optoelectronics, ranging from rectifying diodes, to light-emitting diodes, solar cells, and photodetectors.

## Chapter 4: Structural, optical, and electronic properties of layered 2D PdSe<sub>2</sub>

### 4.1 Introduction

The emergence of 2D materials with unique structure and extraordinary electronic properties provides exciting opportunities for applications in nanoscale electronics.<sup>16</sup> For example, graphene (whose crystal structure is shown in Fig. 4.1a) has gained attention due to its high carrier mobility resulting from an effectively massless state of charge carriers,<sup>2</sup> but its inherent lack of a band gap, and the inability so far to induce a sizable one, limits its application in electronics. It would thus be desirable to realize a 2D system with a widely tunable band gap when targeting applications in nanoscale devices. This has led to the exploration of TMDs and other 2D materials beyond graphene.<sup>3</sup> In this regard, MoS<sub>2</sub> has attracted the most attention because of its moderate mobility and high current on/off ratio in transistors, however, MoS<sub>2</sub> possesses a limited band gap variation between  $\sim 1.2 - 1.9$  eV<sup>4,5</sup>.

Until the recent introduction of black phosphorus (BP), with a band gap variation from 0.3 – 1.5 eV, materials with such a widely tunable band gap were difficult to find.<sup>6</sup> As shown in Fig. 4.1b, BP has a honeycomb network similar to graphene, but is strongly puckered (that is, not ideally planar, but oscillating out-of-plane in a regular corrugated manner), rendering exotic properties of the in-plane anisotropic response to external stimulations, such as polarized light, electric field, applied strain.<sup>56,83,84</sup> These anisotropies have their origins rooted in the puckering of the lattice structure, which provides a new degree of freedom to explore in 2D materials. Recently, other buckled or puckered 2D materials with hexagonal structure have been theoretically and experimentally reported in elemental 2D materials (also called Xenes) such as silicene, germanene, and stanene.<sup>60,61</sup> In contrast with an isotropic hexagonal structure, the buckling breaks the

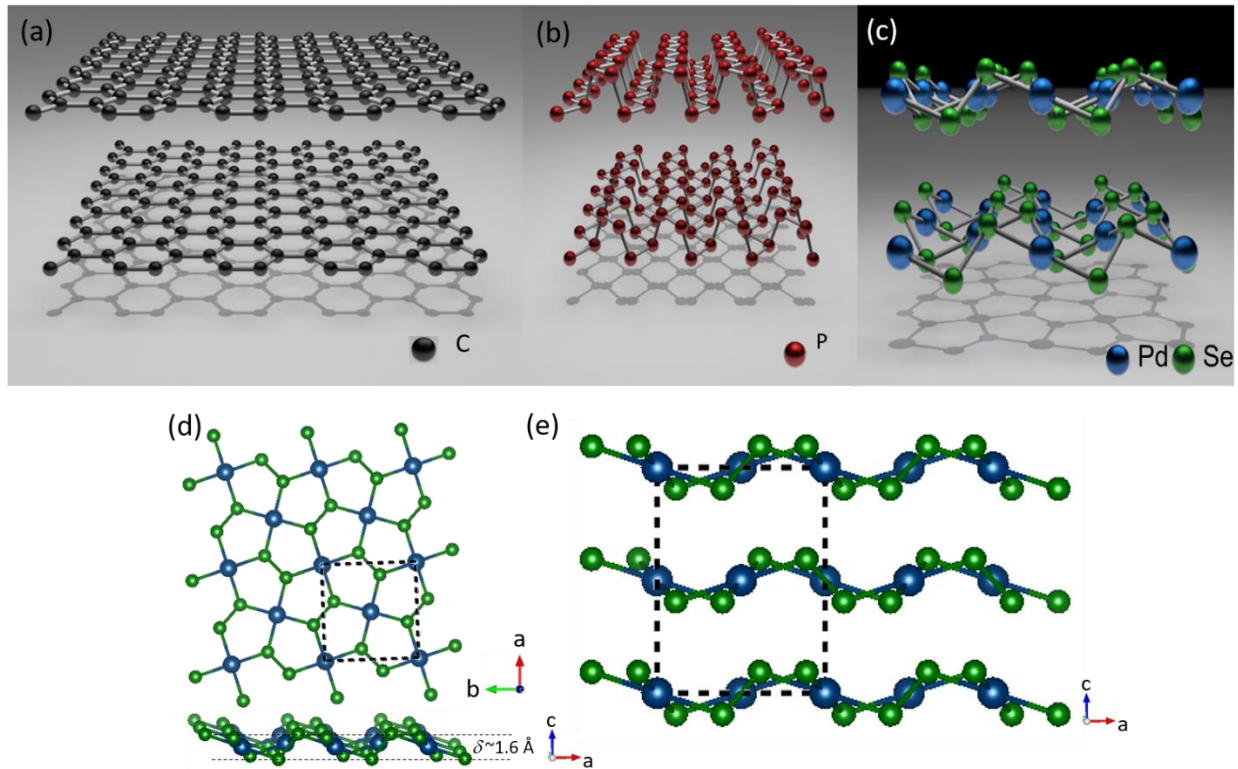


**Figure 4.1.** Polymorphism in 2D materials displayed across hexagonal flat graphene (a), hexagonal puckerd black phosphorus (b), and pentagonal puckerd PdSe<sub>2</sub> (c). (d) Top and side view of the crystal structure of monolayer PdSe<sub>2</sub> showing a puckerd pentagonal configuration. The gray spheres represent the Pd atoms, while the yellow spheres represent the Se atoms. Dashed line indicates the unit cell. The vertical puckerd distance,  $\delta$ , is around  $\sim 1.6$  Å. (e) Crystal structure of tri-layer PdSe<sub>2</sub> with dashed line indicating the unit cell.

sublattice symmetry, enhances spin-orbit coupling, and allows tuning of a topological quantum phase transition.<sup>62</sup> However, despite their potential importance for device applications, the realization of stable 2D buckled or puckered hexagonal structures of 2D elemental materials including BP, silicene, germanene, and stanene is still a great challenge for practical electronics. Furthermore, 2D materials with buckled or puckered pentagonal structure are another class of highly desirable 2D materials due to the low symmetry lattice structure. They have recently been theoretically predicted but have remained unexplored experimentally.<sup>47-49</sup> The pentagons are usually considered as topological defects or geometrical frustrations as stated in the well-known “isolated pentagon rule” (IPR),<sup>50</sup> but rarely found as basic building blocks in 2D materials.

In this chapter, a new 2D material, atomically thin PdSe<sub>2</sub> crystals (shown in Fig. 4.1c) with a novel puckered pentagonal structure is revealed. The puckered 2D PdSe<sub>2</sub> flakes exhibit a widely tunable band gap that varies from metallic (bulk) to ~1.3 eV (monolayer). The top and side view of the crystal structure of monolayer and few-layer PdSe<sub>2</sub> are shown in Fig. 4.1d, with the solid line showing the unit cell. Each layer has a Se-Pd-Se configuration, with each Pd atom located at the corners of a square and covalently bonded to four Se atoms, thereby forming a unique pentagonal structure that has only been predicted theoretically for graphene and few other 2D materials<sup>36,47,49</sup>. The bulk structure is made up of single layers of PdSe<sub>2</sub> stacking along the *c*-axis and held together mainly by vdW forces (Fig. 4.1e). From the top view, we can see that the monolayer PdSe<sub>2</sub> crystals are composed entirely of pentagonal rings, presenting an intriguing pattern that is known as the Cairo pentagonal tiling. This unique pentagonal structure has been predicted theoretically to be stable only for graphene and a few other 2D materials. In contrast to the structure of hexagonal 2D materials such as graphene, Xenes, and TMDs that have been reported experimentally, the PdSe<sub>2</sub> monolayer structure features unusual planar tetra-coordination

of its Pd atoms, puckered pentagons with a vertical puckering distance,  $\delta$ , of  $\sim 1.6$  Å, as well as Se–Se bonds. Since most of the reported 2D materials that have been reported experimentally exhibit a hexagonal structure, monolayer PdSe<sub>2</sub> presents a unique opportunity to study novel phenomena in 2D pentagonal configurations.

## 4.2 Growth and synthesis of bulk and few-layers PdSe<sub>2</sub>

Bulk PdSe<sub>2</sub> single crystals were grown by a self-flux method through melting stoichiometric amounts of Pd powder (99.98%, Alfa Aesar) and Se powder (99.94%, Alfa Aesar). The Pd and Se powders in an atomic ratio of Pd : Se = 1 : 6 were thoroughly mixed together and sealed in an evacuated quartz ampoule under a vacuum condition of  $10^{-6}$  Torr and then placed in a one-zone thermal furnace (Fig. 4.2a). The furnace was slowly heated up to 850 °C and held for 50 hrs and then allowed to cool to 450 °C at a rate of 3°C/hr, followed by cooling down to room temperature. Shiny single crystals of PdSe<sub>2</sub> were obtained by cleaving the ingot, i.e., the product, which is composed of the PdSe<sub>2</sub> flakes. The as-grown crystals are plate-like with a thickness around 4 mm (Fig. 4.2b). Fig. 4.2c shows the diffraction pattern where the diffraction peaks at 23.1°, 41.5°, 50.1° and 64.9° which can be indexed to (002), (113), (213) and (400) plane reflections of PdSe<sub>2</sub>.<sup>85</sup> The strong and sharp (002) peak indicates that the (002) plane is the highly preferred orientation for the synthesized PdSe<sub>2</sub>. Bulk PdSe<sub>2</sub> displays Pbc<sub>a</sub> symmetry (point group D<sub>2h</sub>) with an orthorhombic lattice that contains four Pd and eight Se atoms in one unit cell.<sup>86</sup>

Although the predicted interlayer binding energy of PdSe<sub>2</sub> (190 meV/atom) is significantly higher than that of BP (40 meV/atom),<sup>36</sup> PdSe<sub>2</sub> mono- and few-layer structures were able to be isolated using micromechanical exfoliation by adhesive tapes, and as shown in Fig. 4.2(d-f), large areas ( $\sim 30$  μm) were obtained. Interestingly, PdSe<sub>2</sub> exfoliates primarily into regular rectangular

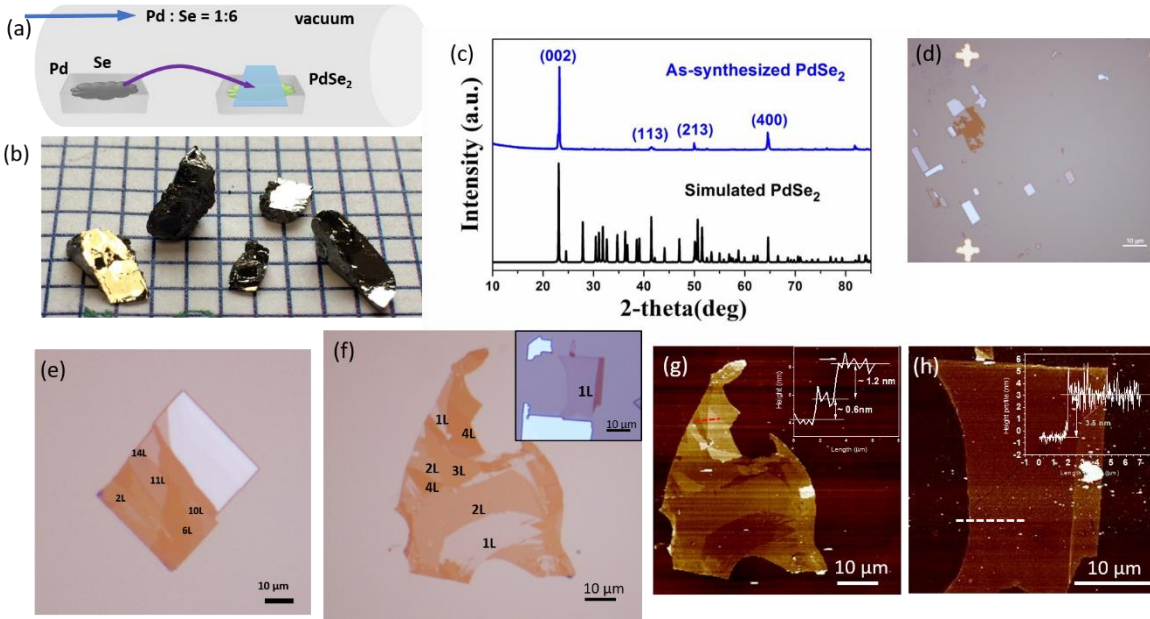


**Figure 4.2.** (a) Schematic of the thermal furnace used for the growth of PdSe<sub>2</sub> bulk single crystals. (b) Image of the as-grown PdSe<sub>2</sub> single crystals (~ 4 mm). (c) Powder XRD pattern of the as-synthesized PdSe<sub>2</sub> sample. (d-f) Optical images of single and few-layer PdSe<sub>2</sub>. (g-h) Atomic force microscopy image and height profile corresponding to image (f) and its inset.

shapes, allowing the identification of its crystalline orientation. The optical contrast being a function of thickness aids the identification of few-layer PdSe<sub>2</sub>. Thicker samples appear brighter, so monolayer and bilayer PdSe<sub>2</sub> areas are more challenging to identify due to their low optical reflectance. The thickness of the monolayer crystals was verified from atomic force microscopy (AFM) to be ~0.6 nm as shown in Fig. 4.2g. The thickness of multilayered PdSe<sub>2</sub> crystals was inferred from AFM measurements and cross-calibrated by micro-Raman and micro-absorption spectroscopies. Due to tip-surface interaction effects, measuring monolayer flakes can give spurious measurement.<sup>64</sup> For example, monolayer PdSe<sub>2</sub> shown in the inset of Fig. 4.2f determined by Raman and optical contrast gave a measurement of 3.5 nm (Fig. 4.2h). To estimate the thickness accurately, the difference in the thickness of corresponding layers, i.e. the difference between 1 L and 2 L, 2 L and 3 L, and so (shown in Fig. 4.2g) was used. For accurate measurement, low-frequency Raman<sup>87</sup> measurements were carried out.

### 4.3 Atomic structure of PdSe<sub>2</sub>

The atomic structure of the PdSe<sub>2</sub> flakes was characterized by scanning transmission electron microscopy (STEM). As-exfoliated PdSe<sub>2</sub> flakes on silicon substrate were transferred onto TEM grids. Although large monolayer PdSe<sub>2</sub> flakes can be exfoliated onto a substrate and transfer onto a TEM grid, it is hard to distinguish the pentagonal structure in the annular dark-field (ADF) image (Fig. 4.3a) due to the surrounding disordered region of the flakes, perhaps resulting from damage during transfer. The ADF intensity in the line profile corresponding to the red dashed line shows distinct intensity for Pd and Se columns. Although, the positions of atomic columns agree with the monolayer simulated model (Fig. 4.3b) sliced from bulk PdSe<sub>2</sub>, the intensity of the columns does not quite follow the ration between Pd and Se atoms. There are three explanations for this. One, single layer PdSe<sub>2</sub> might exist on a substrate like SiO<sub>2</sub> but is unstable in the free-



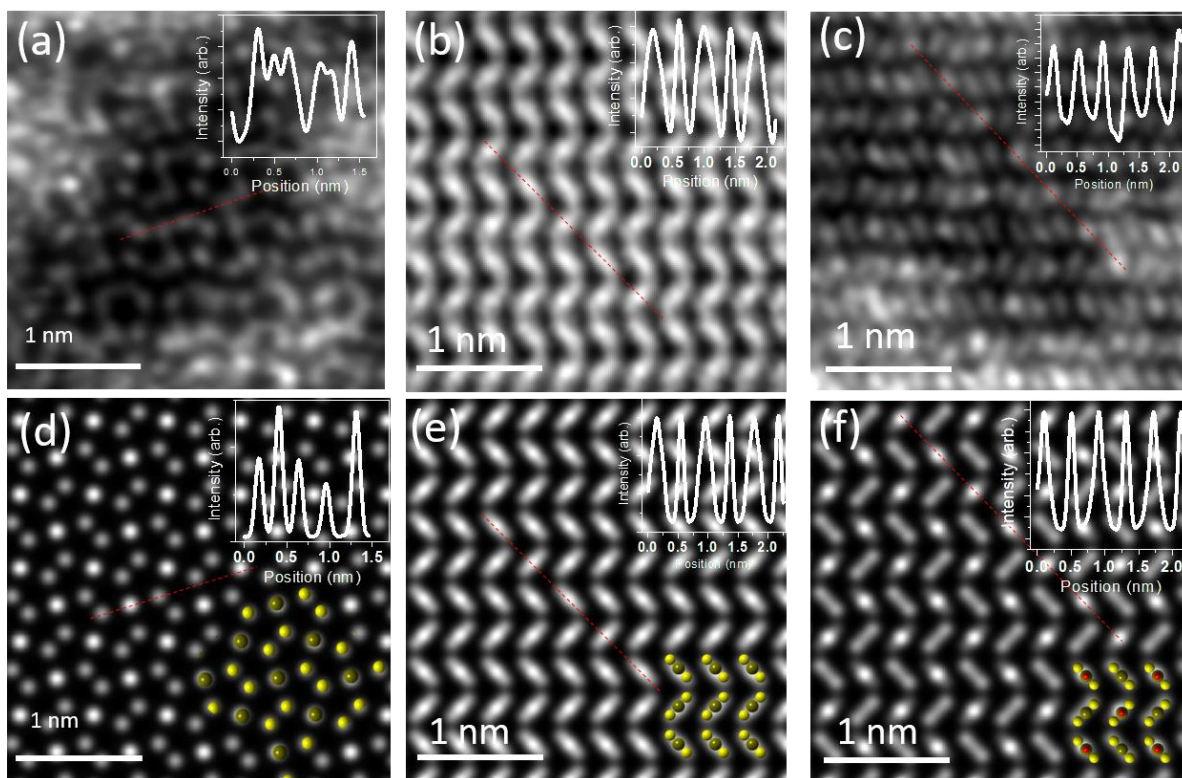


**Figure 4.3.** Atomic resolution structure of few-layer PdSe<sub>2</sub> crystals revealed by Z-contrast STEM images (top row) and corresponding simulated images (bottom row) of PdSe<sub>2</sub>. (a, c) Single layer, (b, e) Even number of layers, (c, f) odd number of layers. Insets in (d-f) show atomic models of the corresponding STEM images.

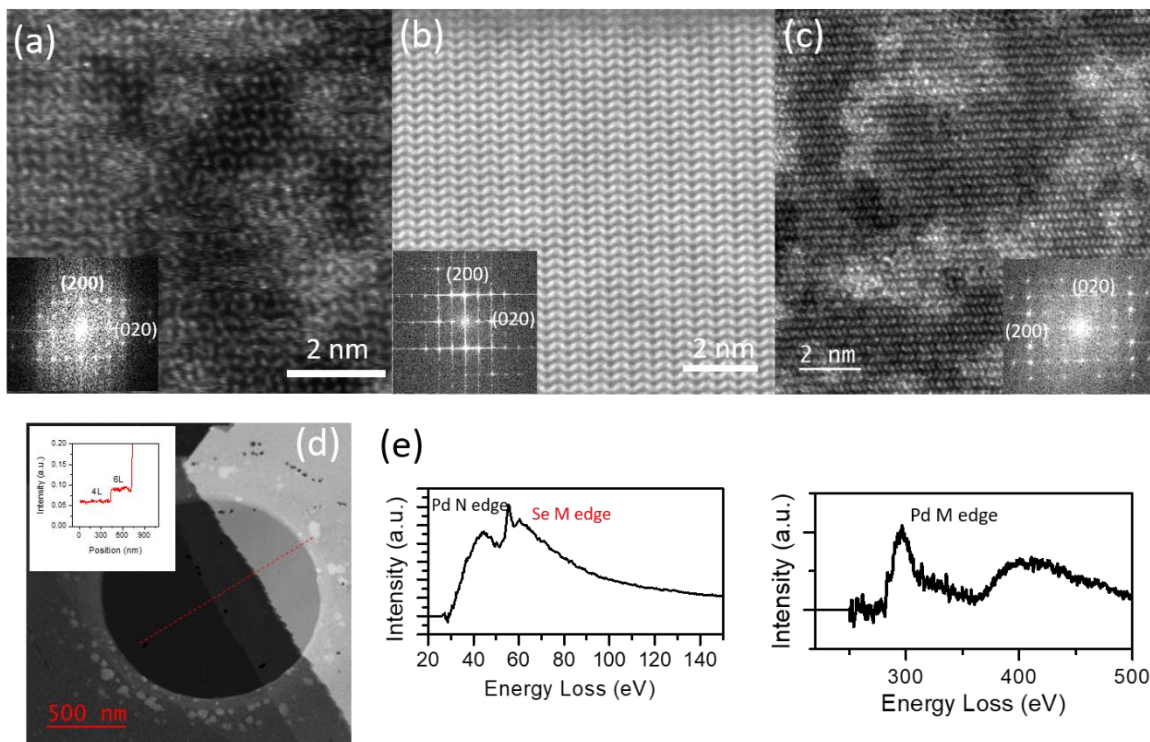
standing form. Two, single layer PdSe<sub>2</sub> is fragile and is easily damaged during transfer on the TEM grid. Three, the electron beam from STEM could easily damage single layer PdSe<sub>2</sub> after transfer.

Fig. 4.3(b-c) shows the ADF images of few-layer PdSe<sub>2</sub> crystals, and although even and odd layer numbers appear very different in ADF due to symmetry differences, the patterns agree very well with the image simulations shown in Fig. 4.3(d-e), respectively. Bulk PdSe<sub>2</sub> crystals exhibit *Pbca* space group symmetry and *D*<sub>2h</sub> point group symmetry. In contrast, thin flakes with either an odd or even number of layers belong to space group *P2*<sub>1</sub>/*c* (No. 14) and point group *C*<sub>2h</sub> (*2/m*) with inversion symmetry or space group *Pca2*<sub>1</sub> (No. 29) and point group *C*<sub>2v</sub> (*mm2*) without inversion symmetry, respectively. The fast Fourier transform (FFT) patterns of single and few-layer PdSe<sub>2</sub> in Fig. 4.4(a-c) show the rectangular structure distinct from the hexagonal structure of other TMDs. Each flake has an identical lattice structure with similar diffraction patterns of (020) and (200), confirming the crystallinity of each flake. Electron energy loss spectroscopy (EELS) of the few-layer PdSe<sub>2</sub> flakes (Fig. 4.4(d-e)) shows characteristic peaks of Pd N, M edges and Se M edges.

## 4.4 Electronic properties of PdSe<sub>2</sub>

### 4.4.1 Density Functional Theory (DFT) calculations

Plane-wave density functional theory (DFT) calculations were performed using the VASP package equipped with the projector-augmented-wave (PAW) method for electron-ion interactions<sup>88</sup>. The exchange-correlation interactions were considered in the generalized gradient approximation (GGA) using the Perdew-Burke-Ernzerhof (PBE) functional<sup>89</sup>. Van der Waals (vdW) interactions between the PdSe<sub>2</sub> layers were included using the vdW density functional method optPBE-vdW (denoted as optPBE)<sup>90</sup>. For bulk PdSe<sub>2</sub>, both atoms and cell volume were allowed to relax (i.e., ISIF = 3) until the residual forces were below 0.001 eV/Å, with the cutoff



**Figure 4.4.** (a-c) The atomic resolution STEM images of PdSe<sub>2</sub> monolayer, (b) even layer (c) and odd layer. Insets of these STEM images show the corresponding Fast Fourier Transformation diffraction patterns. Diffraction spots corresponding to two principle planes (020) and (200) are labeled. (d) A low-magnification STEM image of few-layer PdSe<sub>2</sub> crystal. Inset shows the line profile of the red dash line in image which the layer thickness is determined to be 4L and 6L according intensity. (e) Electron energy loss spectroscopy of few-layer PdSe<sub>2</sub>, Pd N edge, Pd M edge and Se M edge are shown in the spectra.

energy at 350 eV and the  $12 \times 12 \times 8$  k-point sampling. The optimized bulk lattice constants obtained via optPBE are  $a=5.85 \text{ \AA}$ ,  $b=5.99 \text{ \AA}$  and  $c=7.95 \text{ \AA}$ , in agreement with the experimental values ( $a=5.75 \text{ \AA}$ ,  $b=5.87 \text{ \AA}$  and  $c=7.69 \text{ \AA}$ )<sup>55,85</sup>. Note that the out-of-plane direction is defined as the  $z$  axis. Other functionals implemented in VASP were also tested, including the local density approximation (LDA), PBE, the DFT-D2 approach of Grimme, vdW-DF, vdW-DF2, optB86b-vdW, and optB88-vdW.

**Table 4.1.** Optimized bulk PdSe<sub>2</sub> lattice constants using different functionals with projector-augmented-wave (PAW) pseudopotentials in the DFT package of VASP. The experimental values are also shown in the second column for comparison.

Lattice constant	Exp. value	LDA	PBE	DFT-D2	Nonlocal van der Waals functionals				
					vdW-	vdW-	optPBE	optB86b	optB88
$a(\text{\AA})$	5.75	6.11	5.79	6.20	5.90	6.01	5.85	6.22	5.85
$b(\text{\AA})$	5.87	6.10	5.94	6.19	6.05	6.15	5.99	6.22	5.97
$c(\text{\AA})$	7.69	6.12	8.48	6.21	8.47	8.34	7.95	6.23	7.63

Table 4.1 lists the optimized bulk PdSe<sub>2</sub> lattice constants using different functionals with projector-augmented-wave pseudopotentials in the self-consistent plane-wave DFT package VASP. Among studied functionals, optPBE and optB88 yield the best results compared to the experimental values. Though the structural parameters by optB88 are closer to experimental ones than optPBE, optPBE is found to be better for describing the electronic properties of bulk PdSe<sub>2</sub>. Compared to optB88 that predicts a negative electronic band gap -0.24 eV (i.e., the energy level of VBM is higher than that of CBM), optPBE yields a much smaller negative band gap -0.02 eV. According to our optical absorption measurements and prior experimental and theoretical works<sup>55,91,92</sup>, bulk PdSe<sub>2</sub> is intrinsically semiconducting, though its band gap is relatively small

(about 0.2-0.4 eV). Therefore, optPBE seems an overall better choice, and it is used for describing the electronic, vibrational and Raman properties of PdSe<sub>2</sub> system. Nevertheless, it still underestimates the band gap of bulk PdSe<sub>2</sub>. The PBE functional yields good description of the in-plane lattice constants (a and b), while overestimates the lattice constant c, owing to the underestimation of the interlayer coupling. However, it gives a reasonable value of the band gap (0.37 eV). Consequently, PBE is also adopted to describe the electronic properties of PdSe<sub>2</sub>.

It is interesting to note that functionals like LDA, DFT-D2 and optB86b yield a completely different structure, where the lattice constants in three directions are nearly the same (around 6.1-6.2 Å). As the lattice in the c direction is decreased, the interlayer distance is shortened and Pd atoms form new bonds with Se atoms in the adjacent layers, and then the originally orthorhombic layered structure is transformed into the 3D pyrite structure<sup>85,91</sup>. Such structural transition was investigated previously by external pressure<sup>85</sup>. Because of the existence of two phases in PdSe<sub>2</sub>, it requires caution for choosing the proper functional for theoretical investigation.

Furthermore, different functionals and pseudopotentials were tested in another DFT software, the self-consistent plane-wave Quantum Espresso<sup>93</sup>. Several vdW functionals with both projector-augmented-wave and norm-conserving pseudopotentials for bulk PdSe<sub>2</sub> were considered. The non-local vdW functionals that we considered are vdW-DF, vdW-DF2, C09-DF, C09-DF2, optB86b, optB88 and revB86b<sup>90,94,95</sup>. For comparison, LDA, PBE and the semi-empirical dispersion correction method DFT-D2 were also considered<sup>96</sup>. The bulk structures were relaxed to a force threshold  $1 \times 10^{-3}$  eV/Å and a pressure threshold 0.5 Kbar with  $12 \times 12 \times 10$  k-point sampling and 816 eV kinetic energy cutoff. The optimized lattice constants for bulk PdSe<sub>2</sub> are listed in Table 4.2 and Table 4.3 for different pseudopotentials respectively.

**Table 4.2.** Optimized bulk PdSe<sub>2</sub> lattice constants using different functionals with projector-augmented-wave (PAW) pseudopotentials in the DFT package of Quantum Espresso.

Lattice	LDA	PBE	DFT-D2	Nonlocal van der Waals functionals						
				vdW-DF	vdW-DF2	C09-DF	C09-DF2	optB86b	optB88	revB86b
<b>constant</b>										
<b>a(Å)</b>	6.09	5.80	5.79	5.89	6.01	6.16	6.18	5.84	5.86	5.84
<b>b(Å)</b>	6.10	5.95	5.92	6.05	6.16	6.17	6.17	5.95	5.99	5.96
<b>c(Å)</b>	6.10	8.65	7.70	8.68	8.47	6.17	6.19	7.49	7.71	7.53

**Table 4.3.** Optimized bulk PdSe<sub>2</sub> lattice constants using different functionals with Troullier-Martins type norm-conserving pseudopotentials in Quantum Espresso.

Lattice	LDA	PBE	DFT-D2	Nonlocal van der Waals functionals						
				vdW-DF	vdW-DF2	C09-DF	C09	optB86b	optB88	revB86b
<b>constant</b>										
<b>a(Å)</b>	6.10	5.79	5.78	5.90	5.79	6.21	6.22	5.79	5.79	5.79
<b>b(Å)</b>	6.11	5.95	5.92	6.05	5.95	6.22	6.23	5.95	5.95	5.95
<b>c(Å)</b>	6.11	8.72	7.77	8.64	8.68	6.21	6.22	8.68	8.72	8.69

Similar to the results by VASP, different functionals and pseudopotentials by Quantum Espresso also yield different structures, including the orthorhombic layered structure and the 3D pyrite structure.

The functionals of optPBE and PBE are two options that yield reasonable results for both electronic and structural properties. Unless mentioned otherwise, they are adopted throughout this thesis. Single- and few-layer PdSe<sub>2</sub> systems were modeled by a periodic slab geometry with a vacuum region of at least 21 Å in the out-of-plane direction ( $z$  direction) used to avoid spurious interactions with periodic images. For the 2D slab calculations where  $12 \times 12 \times 1$  k-point samplings were used, all atoms were relaxed until the residual forces were below 0.001 eV/Å and in-plane lattice constants were optimized using the method of fixing the total volume (ISIF = 4 in VASP)<sup>97</sup> to avoid the collapse of the vacuum separation in the  $z$  direction. Our calculations find out that the in-plane lattice constants are thickness dependent, owing to the strong interlayer coupling and hybridization in PdSe<sub>2</sub>. For instance, the loss of the neighboring layers from bulk to monolayer leads to the in-plane lattice shrinking:  $a$  is reduced from 5.85 to 5.72 Å, and  $b$  reduced from 5.99 to 5.93 Å, according to the optPBE calculations. Few-layer systems also exhibit the in-plane lattice reduction compared to the bulk, but the amplitude of the reduction decreases with the increasing number of layers. Note that the definition of the out-of-plane direction as the  $z$  direction is in line with the convention of International Crystallography Tables for the bulk, but it is not for  $NL$  PdSe<sub>2</sub>. Instead, according to the convention, for odd  $NL$  PdSe<sub>2</sub>, the out-of-plane direction should be along the  $x$  direction; for even  $NL$  PdSe<sub>2</sub>, the out-of-plane direction should be along the  $y$  direction. However, for simplicity and consistency, we chose the  $z$  axis as the out-of-plane direction for all thicknesses. As a result, the Raman mode symmetry notations in even  $NL$  are slightly different



from the convention:  $A_2$  and  $B_1$  are swapped. In this work, from bulk to even  $NL$ , the bulk  $B_{1g}$  symmetry is reduced to  $B_1$  instead of  $A_2$ .

For the fully relaxed geometries, the dynamic matrix was then calculated using the finite difference scheme implemented in the Phonopy software to obtain phonon frequencies and eigenvectors<sup>98,99</sup>. Hellmann-Feynman forces in the supercell ( $2 \times 2 \times 2$  for the bulk, while  $2 \times 2 \times 1$  for single- and few-layer systems) were computed by VASP for both positive and negative atomic displacements ( $\delta = 0.03 \text{ \AA}$ ) and then used in Phonopy to construct the dynamic matrix, whose diagonalization provides phonon frequencies and phonon eigenvectors (i.e., vibrations). Raman scattering calculations were then performed within the Placzek approximation. For the  $j$ -th phonon mode, Raman intensity is  $I \propto \frac{(n_j+1)}{\omega_j} |e_i \cdot \tilde{R} \cdot e_s^T|^2$ , where  $e_i$  and  $e_s$  are the electric polarization vectors of the incident and scattered lights respectively, and  $\tilde{R}$  is the Raman tensor of the phonon mode<sup>100</sup>.  $\omega_j$  is the frequency of the  $j$ -th phonon mode, and  $n_j = (e^{\hbar\omega_j/k_B T} - 1)^{-1}$  is its Boltzmann distribution function at the given temperature  $T = 300 \text{ K}$ . The matrix element of the ( $3 \times 3$ ) Raman tensor  $\tilde{R}$  of the  $j$ -th phonon mode is<sup>100-102</sup>

$$\tilde{R}_{\alpha\beta}(j) = V_0 \sum_{\mu=1}^N \sum_{l=1}^3 \frac{\partial \chi_{\alpha\beta}}{\partial r_l(\mu)} \frac{e_l^j(\mu)}{\sqrt{M_\mu}}, \quad (4.1)$$

where  $\chi_{\alpha\beta} = (\varepsilon_{\alpha\beta} - \delta_{\alpha\beta})/4\pi$  is the electric polarizability tensor related to the dielectric tensor  $\varepsilon_{\alpha\beta}$ ,  $r_l(\mu)$  is the position of the  $\mu$ -th atom along the direction  $l$ ,  $\frac{\partial \chi_{\alpha\beta}}{\partial r_l(\mu)}$  is the derivative of the polarizability tensor (essentially the dielectric tensor) over the atomic displacement,  $e_l^j(\mu)$  corresponds to the displacement of the  $\mu$ -th atom along the direction  $l$  in the  $j$ -th phonon mode (i.e., the eigenvector of the dynamic matrix),  $M_\mu$  is the mass of the  $\mu$ -th atom, and  $V_0$  is the unit cell volume. For both positive and negative atomic displacements ( $\delta = 0.03 \text{ \AA}$ ) in the unit cell, the

dielectric tensors  $\varepsilon_{\alpha\beta}$  were computed by VASP<sup>103</sup> at the experimental laser frequency 2.33 eV (532 nm) and thus their derivatives were obtained via the finite difference scheme<sup>104</sup>. Based on the phonon frequencies, phonon eigenvectors and the derivatives of dielectric tensors, Raman tensor  $\tilde{R}$  of any phonon mode can be obtained. In the experimental back-scattering laser geometry (i.e., the light travels in and out along the  $z$  direction, perpendicular to the sample plane), the electric polarization vectors of incoming and scattered light ( $e_i$  and  $e_s$ ) are in the  $x$ - $y$  plane. Averaging over all possible in-plane polarizations, the Raman intensity of any given mode in the experimental unpolarized laser configuration is given by  $I \propto \frac{1}{4} \frac{(n_j+1)}{\omega_j} (|\tilde{R}_{11}|^2 + |\tilde{R}_{12}|^2 + |\tilde{R}_{21}|^2 + |\tilde{R}_{22}|^2)$ . Finally, based on the calculated Raman intensities  $I(j)$  and phonon frequencies  $\omega_j$ , the Raman spectrum can be obtained after Lorentzian broadening.

#### 4.4.2 Phonon spectrum

The dynamical stability of the single- and few-layer PdSe<sub>2</sub> is confirmed by the absence of soft modes in the calculated phonon dispersions (Fig. 4.5(a-c)). Note that very small negative frequencies are still present in the calculated phonon dispersion of single-layer PdSe<sub>2</sub>, but by switching to the LDA functional they can be nearly eliminated, suggesting that such negative frequencies are likely not due to structural instability.

#### 4.4.3 Electronic band structure

According to the calculated electronic band structures in Fig. 4.6(a-b), 1L PdSe<sub>2</sub> exhibits 1.3 eV indirect band gap and no band gap for the bulk. The 1.3 eV indirect band gap for a monolayer is quite close to its direct band gap (1.43 eV), making the PdSe<sub>2</sub> monolayer promising

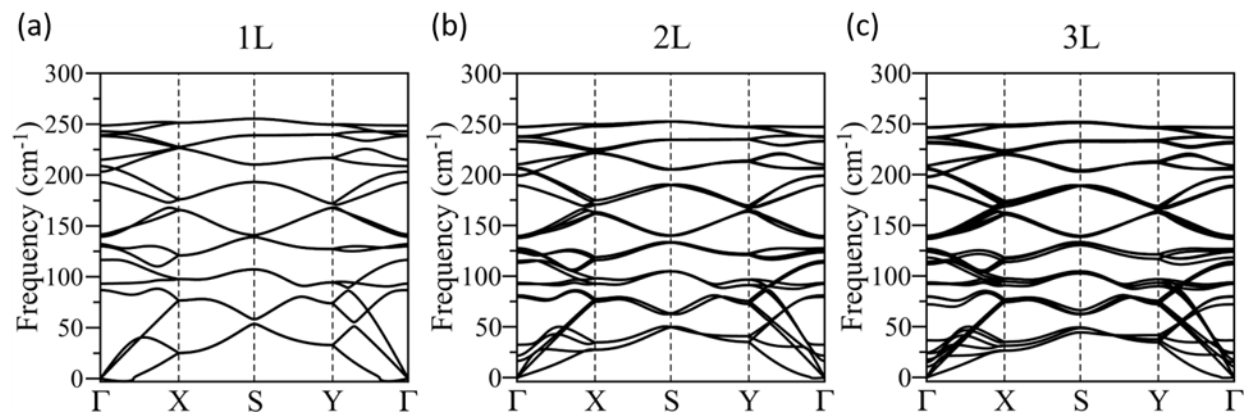


**Figure 4.5.** Calculated phonon dispersion spectrum of single-layer and few-layers of PdSe<sub>2</sub>. There are no noticeable soft modes in 1L PdSe<sub>2</sub>, while the small negative frequencies are probably due to the computational error.

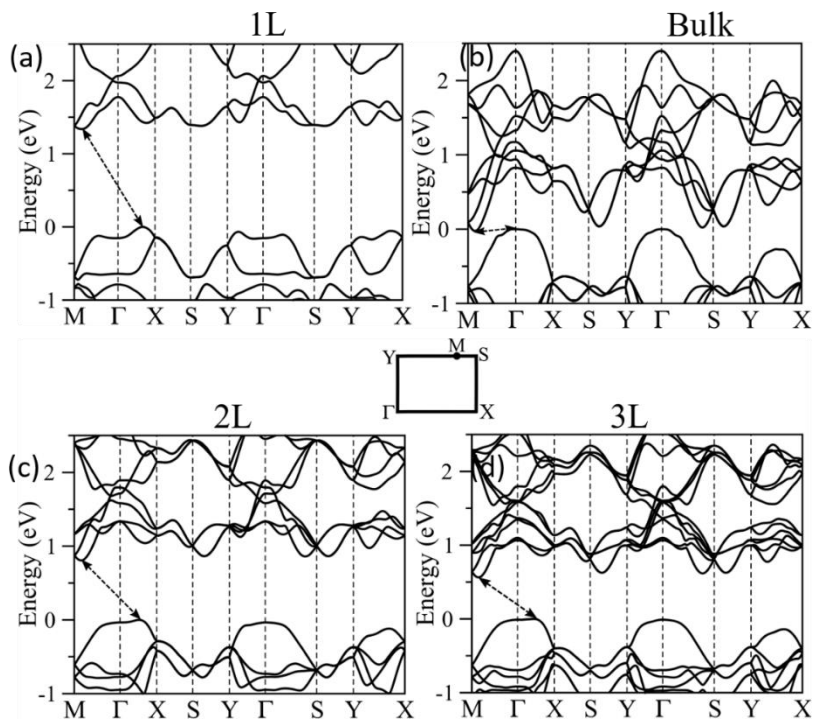


**Figure 4.6.** Calculated electronic band structures of (a) 1L, (b) bulk, (c) 2L and (d) 3L PdSe<sub>2</sub> by the PBE method. The dashed arrows indicate the lowest energy transitions between the valence band maximum (VBM) and conduction band minimum (CBM). The VBM is set at 0 eV. Inset of figure shows Brillouin zones of PdSe<sub>2</sub> 2D crystals with high-symmetry points labeled.

for optoelectronic applications. Similar indirect band gaps are observed in few-layer PdSe<sub>2</sub> as well (Fig. 4.6(c-d)), indicating the intrinsic nature of this indirect band gap semiconductor compared to the indirect-to-direct band gap transition observed in other TMDs. The valence band maximum (VBM) is located between the high-symmetry  $\Gamma$  and X (0.5, 0, 0) points while the conduction band minimum (CBM) is located between  $\Gamma$  and M (0.38, 0.5, 0) points, suggesting that it is not located along the high-symmetry lines like the commonly studied TMDs (MoS<sub>2</sub> family) and BP. For the PdSe<sub>2</sub> systems, both the valence band edge and conduction band edge are contributed mostly by the Pd 4d-states and Se 4p-states, which indicates that the energy levels of both VBM and CBM (thus the band gap) are sensitive to the interlayer coupling and electronic hybridization. The inset of Fig. 4.6 shows the rectangular shape of the first Brillouin zone of PdSe<sub>2</sub> 2D crystals.

## 4.5 Optical properties of PdSe<sub>2</sub>

### 4.5.1 Absorption spectroscopy

Owing to the indirect band gap nature of PdSe<sub>2</sub>, the photoluminescence signals are too weak to be effectively detected for experimental bandgap determination. Therefore, optical absorption measurements were carried out and Tauc plots were used to derive the band gaps from the absorption spectra as shown in Fig. 4.7. To measure the absorption spectra of the PdSe<sub>2</sub> crystals, a laser-driven light source (EQ-99-fc, Energetiq) was used (spot size at the sample was  $\sim 2 \mu\text{m}$ ). The transmitted light was captured with a long-distance microscope objective (50 $\times$ , NA = 0.5) and directed to a spectrometer (Spectra Pro 2300i, Acton) equipped with a CCD camera (Pixis 256BR, Princeton Instruments). All the spectra were collected at room temperature. The absorbance (Abs) was calculated as  $\text{Abs} = \log_{10}(I_0/I)$ , where  $I$  and  $I_0$  are the light intensities transmitted through the sapphire substrate on and off a TMD crystal, respectively. Since AFM do not give a precise number of layers, especially for atomically-thin samples, the number of layers,

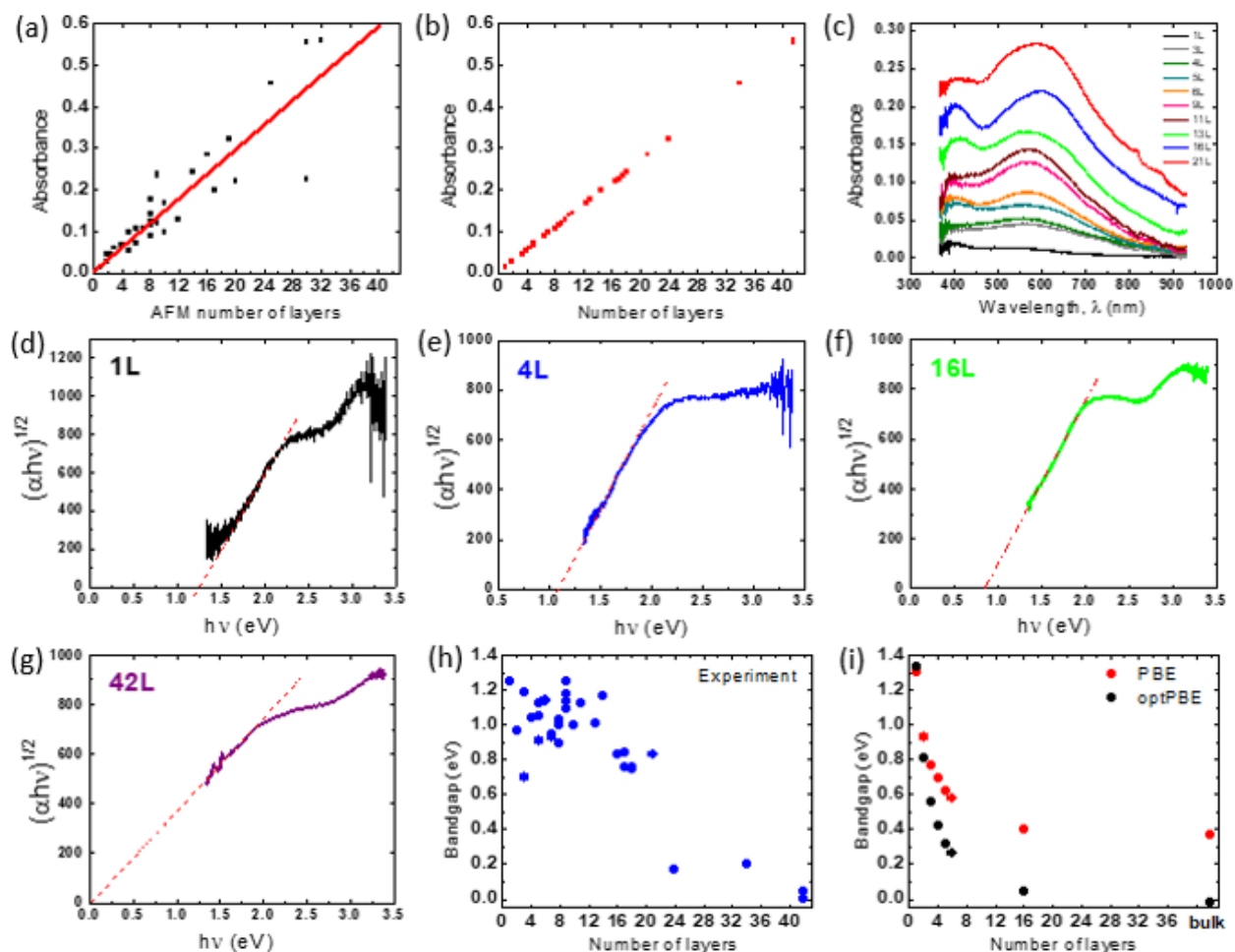


**Figure 4.7.** (a) Plot of the absorbance versus the number of layers where the number of layers was determined by AFM. (b) Plot of absorbance with the number of layers determined based on absorbance measured at 800 nm that was used in the analysis of the bandgap. (c) Absorption spectra for the selected number of layers. (d-g) Tauc plots for 1, 4, 16 and 42 layers, respectively which demonstrates how the bandgap was extrapolated. (h) Band gaps extracted from the Tauc plots for various number of PdSe<sub>2</sub> layers derived from the optical absorption spectra. (i) Band gaps obtained from first-principles calculations - PBE and optPBE shown in red and black dots, respectively.

$N$ , were determined from the absorbance,  $Abs$ , as  $N = Abs/\alpha$ , where  $\alpha$  is the absorbance per one layer or the absorption coefficient. The absorbance of 30 different crystals versus the number of layers derived from AFM measurements is shown in Fig. 4.7a together with its linear fit, that allows one to determine the absorption coefficient,  $\alpha=0.0134$ , and to find the number of layers based on the absorbance measured at 800 nm (Fig 4.7b). Figure 4.7c shows the absorption spectra of PdSe<sub>2</sub> with various numbers of layers. Some of the Tauc plots,  $(\alpha h\nu)^{1/r}$  versus  $h\nu$ , where  $h\nu$  is the energy of the incident photons are shown in Fig. 4.7(d-g). Here, we used  $r = 2$ , because PdSe<sub>2</sub> is an indirect band gap semiconductor. The x-axis intercepts of the slope of the Tauc plots were used to derive the band gaps from the absorption spectra as shown in Fig. 4.7(d-g).

Figure 4.7h shows the optical band gaps versus the number of PdSe<sub>2</sub> layers. The large uncertainty in the band gaps ( $\pm 0.2$  eV) can be explained by a possible high amount of defects in the PdSe<sub>2</sub> flakes. Another possible source of this uncertainty may be related to in-plane anisotropic absorption properties of PdSe<sub>2</sub><sup>17</sup>. However, this data shows a clear trend of decreasing band gap with increasing number of layers from  $\sim 1.3$  eV (1L) to 0 eV (bulk) (within the uncertainty of  $\pm 0.2$  eV). This trend is consistent with the first-principle calculations (Fig. 4.7d), although, the calculated band gap is generally smaller than experimental one because DFT tends to underestimate the band gap due to its limitation to describe the long-range many-body interactions. Therefore, the experimentally observed band gap dependence for the thicker layers may reflect the importance of the many-body effects. Therefore, both the absorption measurements and DFT calculations show a layer-dependent band gap that changes approximately from 0 eV (bulk) to 1.3 eV (monolayer). Note that the changes of the PdSe<sub>2</sub> band gap from bulk to monolayer are noticeably larger than those for MoS<sub>2</sub>.<sup>5</sup> Since Pd has more valence electrons than Mo (10 versus 6), it is expected that interlayer Pd and Se atoms are more hybridized, and that the interlayer

coupling is stronger in this case.<sup>55</sup> This effect contributes to the strong layer-dependent band gaps for PdSe<sub>2</sub> and also for PtS(Se)<sub>2</sub> within the same group.<sup>33,34</sup>

#### 4.5.2 Raman spectroscopy

High-resolution Raman measurements were performed using a Jobin-Yvon T64000 spectrometer consisting of a double monochromator coupled to a third monochromator stage with 1800 groves/mm grating equipped with a liquid nitrogen cooled charge-coupled device (CCD) detector. The high-intensity Raman spectra were measured in a custom high optical throughput micro-Raman setup using a 100x microscope objective with NA (numeric aperture) 0.9 (beam spot on the samples was ~1μm). In this case the scattered Raman light was analyzed by a spectrometer (Spectra Pro 2300i, Acton, f=0.3 m) that was coupled to a microscope and equipped with a 1800 groves/mm grating and a CCD camera (Pixis 256BR, Princeton Instruments). Both high-intensity and high-resolution measurements employed a continuous wave solid-state laser (wavelength 532 nm). All measurements were carried out under a microscope in backscattering geometry.

As shown in Fig. 4.1d, the unit cell of bulk PdSe<sub>2</sub> is orthorhombic with space group *Pbca* (No. 61, point group *D<sub>2h</sub>*). Unlike most well-studied hexagonal TMDs such as MoS<sub>2</sub>, the symmetry of bulk PdSe<sub>2</sub> is comparable to BP, which is also orthorhombic (space group No. 64, point group *D<sub>2h</sub>*). As a result, symmetry assignments of phonon modes for PdSe<sub>2</sub> resemble those for BP, and this indicates that 2D PdSe<sub>2</sub> flakes should have unique anisotropy due to their in-plane low symmetry. The unit cell of bulk PdSe<sub>2</sub> consists of two layers and 12 atoms, and thus there are 36 normal phonon modes at the  $\Gamma$  point whose irreducible representations are

$$\Gamma_{\text{bulk}} = 3A_g + 3B_{1g} + 3B_{2g} + 3B_{3g} + 6A_u + 6B_{1u} + 6B_{2u} + 6B_{3u}, \quad (4.2)$$



where  $3A_g$ ,  $3B_{1g}$ ,  $3B_{2g}$ , and  $3B_{3g}$  modes are Raman active. Raman intensity of a phonon mode is proportional to  $|e_i \cdot \tilde{R} \cdot e_s^T|^2$ , where  $e_i$  and  $e_s$  are the electric polarization vectors of the incident and scattered lights respectively, and  $\tilde{R}$  is the Raman tensor of the phonon mode.<sup>105</sup> It can be observed by Raman spectroscopy when  $|e_i \cdot \tilde{R} \cdot e_s^T|^2$  is not zero. For bulk PdSe<sub>2</sub>, with the out-of-plane direction defined along the lattice  $c$  (i.e., the  $z$  axis) based on the convention of International Tables for Crystallography, the calculated Raman tensors  $\tilde{R}$  of Raman-active modes  $A_g$ ,  $B_{1g}$ ,  $B_{2g}$  and  $B_{3g}$  are<sup>104</sup>

$$\begin{aligned} \tilde{R}(A_g) &= \begin{pmatrix} a & \cdot & \cdot \\ \cdot & b & \cdot \\ \cdot & \cdot & c \end{pmatrix}, & \tilde{R}(B_{1g}) &= \begin{pmatrix} \cdot & d & \cdot \\ d & \cdot & \cdot \\ \cdot & \cdot & \cdot \end{pmatrix}, \\ \tilde{R}(B_{2g}) &= \begin{pmatrix} \cdot & \cdot & e \\ \cdot & \cdot & \cdot \\ e & \cdot & \cdot \end{pmatrix}, & \tilde{R}(B_{3g}) &= \begin{pmatrix} \cdot & \cdot & \cdot \\ \cdot & \cdot & f \\ \cdot & f & \cdot \end{pmatrix}, \end{aligned} \quad (4.3)$$

where  $a$ - $f$  are major terms while other terms (denoted by “ $\cdot$ ”) are either zero or negligible due to symmetry. Note that the calculated Raman tensors can also be qualitatively predicted by group theory analysis (see “Bilbao Crystallographic Server”).<sup>106,107</sup> Raman-inactive modes have zero Raman tensors, thus always zero Raman intensities. Raman-active modes can also have zero intensities, depending on the laser polarizations. In the experimental back-scattering configuration, the electric polarization  $e_i$  and  $e_s$  are in-plane (the  $x$ - $y$  plane), and thus only Raman modes with non-zero Raman tensor elements  $\tilde{R}_{11}$ ,  $\tilde{R}_{12}$ ,  $\tilde{R}_{21}$ , or  $\tilde{R}_{22}$  can show non-zero intensities.

As shown in Fig. 4.8a, only  $A_g$  and  $B_{1g}$  modes can be observed in the unpolarized Raman measurements. This is confirmed by the theoretical Raman spectra shown in Fig. 4.8b, where the bulk spectra (gray lines) exhibit five peaks. Although bulk PdSe<sub>2</sub> has 3  $A_g$  modes ( $A_g^1$ ,  $A_g^2$ ,  $A_g^3$ ) and 3  $B_{1g}$  modes ( $B_{1g}^1$ ,  $B_{1g}^2$ ,  $B_{1g}^3$ ), our calculations found that the  $A_g^1$  and  $B_{1g}^1$  modes are very

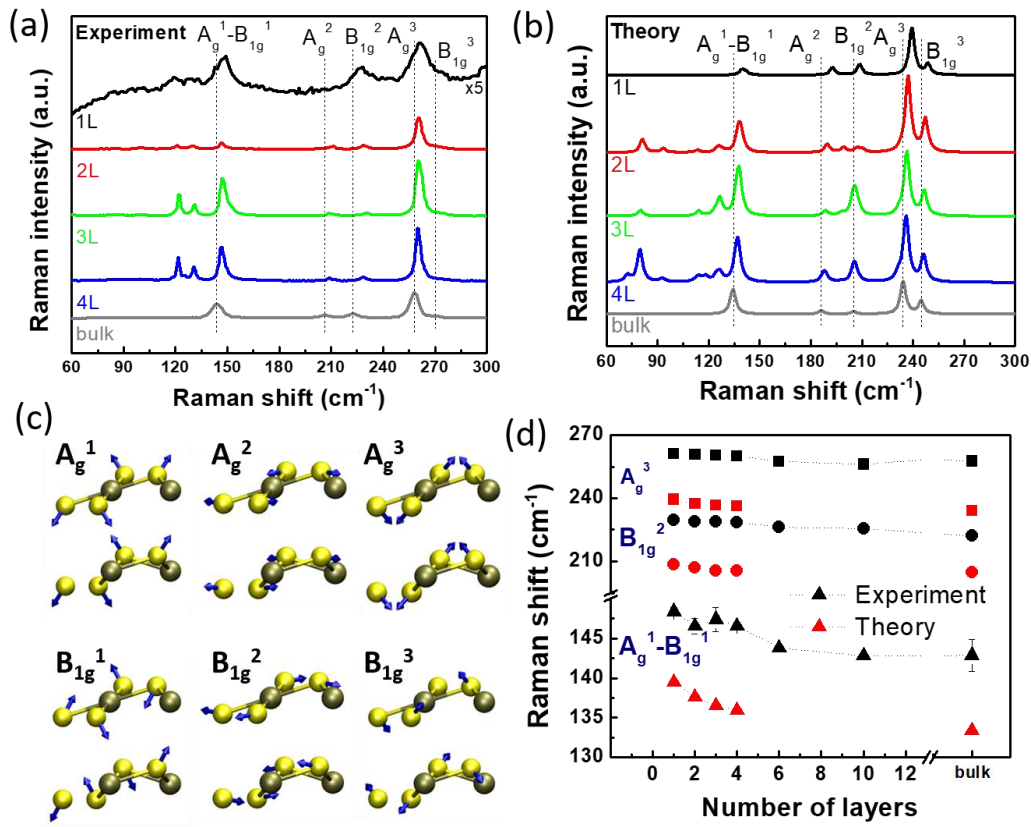


**Figure 4.8.** (a) Layer-dependent Raman spectra of PdSe<sub>2</sub> from 1L to bulk measured for an excitation laser wavelength of 532 nm. (b) Corresponding calculated Raman spectra by the optPBE method. In both (a) and (b), the dashed lines indicate positions of the Raman peaks for bulk PdSe<sub>2</sub>. Note that the A<sub>g</sub><sup>1</sup>-B<sub>1g</sub><sup>1</sup> label means the overlapping of two close peaks: A<sub>g</sub><sup>1</sup> and B<sub>1g</sub><sup>1</sup>. For convenience, bulk notations of A<sub>g</sub> and B<sub>1g</sub> are also used for other systems. (c) Atomic displacements (blue arrows) of six Raman modes in bulk PdSe<sub>2</sub>. (d) Comparison of the experimental (black) and theoretical (red) frequencies of Raman modes A<sub>g</sub><sup>1</sup>-B<sub>1g</sub><sup>1</sup>, B<sub>1g</sub><sup>2</sup> and A<sub>g</sub><sup>3</sup> at different thicknesses. Although the calculated frequencies are systematically smaller than the experimental ones, the trend of the frequency shift versus thickness agrees.

close to each other with a frequency difference of less than  $2 \text{ cm}^{-1}$ , and subsequently a single mixed peak (denoted as  $A_g^1$ - $B_{1g}^1$ ) appears around  $145 \text{ cm}^{-1}$  according to the measurements (around  $134 \text{ cm}^{-1}$  according to the calculations). The rest of four peaks in Raman spectra of the bulk belong to  $A_g^2$ ,  $B_{1g}^2$ ,  $A_g^3$ , and  $B_{1g}^3$ , respectively, as highlighted by the vertical dash lines in Fig. 4.8(a-b). Note that the  $B_{1g}^3$  peak is weak and manifests as a right shoulder peak near the strong  $A_g^3$  peak in the experimental spectra in Fig. 4.8a. For example, the deconvolution of Raman spectra of 2L sample clearly shows the presence of  $B_{1g}^3$  right next to the  $A_g^3$  peak (see Fig. 4.9a). Detailed and strict symmetry assignments for all peaks are presented in Fig. 4.9b, but to further validate the peak symmetry assignments, polarized Raman measurements were carried out. As shown in Figure 4.9(c-d), in both the experimental and simulated polarized Raman spectra of  $\text{PdSe}_2$ , indeed only the three  $A_g$  peaks appear under  $\bar{z}(x, x)z$  while the three  $B_{1g}$  peaks appear under  $\bar{z}(x, y)z$  because the  $A_g$  and  $B_{1g}$  modes have dramatically different response behaviors to laser polarization due to their different Raman tensors.

The atomic vibrations of these six Raman modes are illustrated in Fig. 4.8c. It is interesting to point out that all of them mainly involve the vibrations of the Se atoms (blue arrows in Fig. 4.8c). This can be ascribed to the unique structure in  $\text{PdSe}_2$  (Fig. 4.1d), in which each layer is actually a Se–Pd–Se trilayer with Pd atoms covalently bonded to four Se atoms on the top and bottom sublayers. It is also interesting to note that all five Raman peaks generally shift to higher frequency with the thickness reduction from bulk to 1L. Figure 3.8d shows both the experimental (black) and theoretical (red) frequencies of the  $A_g^1$ - $B_{1g}^1$ ,  $B_{1g}^2$ , and  $A_g^3$  peaks at different thicknesses. Although the calculated frequencies are systematically smaller than the experimental ones (by about  $9\text{--}20 \text{ cm}^{-1}$ ), the trend of the frequency versus thickness is similar. In addition, the significant shifts of Raman peaks around  $5\text{--}9 \text{ cm}^{-1}$  from bulk to 1L for  $\text{PdSe}_2$  are observed, which is different from

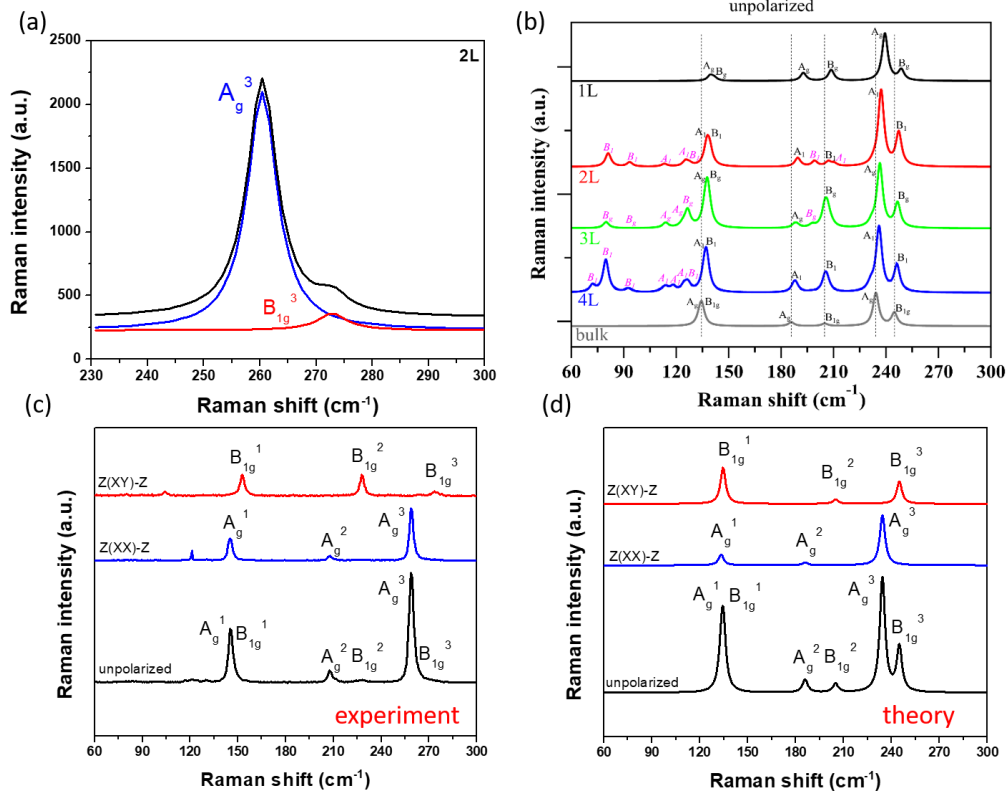


**Figure 4.9.** (a) Zoom-in Raman spectra for to see the presence of the  $B_{1g}^3$  shoulder peak near the  $A_g^3$  peak. The line spectra of the  $A_g^3$  and  $B_{1g}^3$  are fitted to the Raman spectra. (b) Calculated Raman spectra of PdSe<sub>2</sub> via the optPBE method at different thickness. (c) Polarization Raman spectra for several layers (~20 layers) PdSe<sub>2</sub> from experiment (d) bulk PdSe<sub>2</sub> from theory under different laser polarization configurations: unpolarized,  $\bar{z}(x,x)z$ , and  $\bar{z}(x,y)z$ . Both  $A_g$  and  $B_{1g}$  modes can be observed in the unpolarized spectra, only  $A_g$  modes can be observed under the parallel  $\bar{z}(x,x)z$  polarization configuration, while only  $B_{1g}$  modes can be observed under the perpendicular  $\bar{z}(x,y)z$  polarization configuration.

the small shifts around 3–5  $\text{cm}^{-1}$  observed in  $\text{MoS}_2$ . This anomalous shift behavior is attributed to the strong interlayer coupling and hybridization in  $\text{PdSe}_2$ , which also leads to the wide band gap variation as we discussed above. DFT calculations also indicate that the in-plane lattice constants decrease with decreasing thickness because of the strong interlayer interaction in  $\text{PdSe}_2$ . For instance, the in-plane lattice parameters,  $a$  and  $b$ , are reduced by  $\sim 2\%$  and  $\sim 1\%$ , respectively, going from bulk to 1L  $\text{PdSe}_2$ . Such a lattice contraction can stiffen the bonds and enhance the restoring forces (we refer to this as the “lattice shrinking effect”), which is one of the main factors responsible for the increasing peak frequencies from bulk to 1L.

**Table 4.4.** Calculated frequencies of the bulk-related Raman modes for 1L, 2L and bulk  $\text{PdSe}_2$ .

Thickness	$A_g^1$ - $B_{1g}^1$ frequency ( $\text{cm}^{-1}$ )		$B_{1g}^2$ frequency ( $\text{cm}^{-1}$ )		$A_g^3$ frequency ( $\text{cm}^{-1}$ )	
	lattice optimized	lattice fixed	lattice optimized	lattice fixed	lattice optimized	lattice fixed
<b>1L</b>	140.59	133.56	208.66	207.22	239.42	235.28
<b>2L</b>	138.36	135.40	207.03	205.66	237.23	234.92
<b>bulk</b>	133.96		204.95		234.26	

By fixing the in-plane lattice constants of  $NL$  systems to the bulk values (i.e., excluding the lattice shrink effect), the frequencies are systematically lowered by up to 7  $\text{cm}^{-1}$  (more details in Table 4.4). With the lattice shrink effect excluded, the amplitudes of the frequency shifts with the thickness are expectedly smaller, but the computed frequencies of most Raman modes still increase with the decreasing thickness (Table 4.4). This suggests the presence of other contributing

effects. It has been reported that larger force constants are present at the surface of the thin film due to the loss of neighboring layers, which is called the surface effect.<sup>108</sup> Such effect grows stronger with the decreasing thickness owing to an increasing percentage of surface bonds relative to interior bonds. Consequently, the surface effect could result in the frequency increase of a Raman mode with the decreasing thickness, and it is responsible for the upshift of the characteristic  $E_{2g}^1$  mode with the decreasing thickness in group-6 TMDs like  $\text{MoS}_2$ .<sup>38,108-110</sup> Similarly, the surface effect is also one of the factors accounted for the experimentally observed upshifts of Raman modes in  $\text{PdSe}_2$ . Note that for the  $A_g^1$ - $B_{1g}^1$  mixed peak, its experimental frequency shift as a function of the thickness (black in Fig. 4.8d) does not follow a strict monotonous trend. This could arise from the fact that it is the mixture of two peaks. It could also be due to the thickness effect, which has opposite influence on the frequency shift compared to the lattice shrink effect and surface effect discussed above. According to an intuitive harmonic oscillator model, the frequency of a phonon mode should decrease with the decreasing thickness due to the decreasing restoring force by the removal of layers, which is called the thickness effect.<sup>38,108</sup> The lattice-shrink effect and the surface effect are competing with the thickness effect to affect the frequency trend as a function of the thickness, resulting in the non-strict monotonous upshifts of Raman modes in  $\text{PdSe}_2$  in Fig. 4.8d.

## 4.6 Summary

In summary, a new member of the 2D materials family, single- and few-layer  $\text{PdSe}_2$  crystals, was successfully fabricated and characterized. 2D  $\text{PdSe}_2$  exhibits an anisotropically puckered pentagonal structure that was revealed by atomic-resolution scanning transmission electron microscopy. The micro-absorption spectroscopy and first-principles band structure calculations showed a wide band gap variation from  $\sim 0$  (bulk) to  $\sim 1.3$  eV (monolayer) in this

material. The Raman active modes in PdSe<sub>2</sub> were identified by polarized Raman spectroscopy and first-principles calculations, and strong interlayer interactions was revealed from the large layer-dependent Raman peak shifts. In addition, in-plane anisotropic properties should be expected for this highly anisotropic material because of the low in-plane symmetry structure.

## Chapter 5: Electrical transport properties of 2D PdSe<sub>2</sub>: high carrier-mobility and anisotropic behavior

### 5.1 Introduction

Lattice structure and symmetry are vital in determining materials' fundamental properties. Most studied two-dimensional materials exhibit isotropic behavior due to high lattice symmetry; however, lowering the symmetry in 2D materials could induce interesting anisotropic properties of both scientific and technological importance. In this chapter, the anisotropic properties of semiconducting 2D PdSe<sub>2</sub> with puckered pentagonal structure was first reported and exhibited strong in-plane anisotropic properties. Similar to BP, with puckered configurations but stable in air, the 2D PdSe<sub>2</sub> flakes exhibit widely tunable device properties. Fabricated monolayer and few-layer PdSe<sub>2</sub> field-effect transistors display competitive performance including ambipolar charge carrier conduction with high electron mobility of  $\sim 158 \text{ cm}^2\text{V}^{-1}\text{s}^{-1}$  as well as large on/off ratios ( $10^6$ ).

From electrical characterization using field-effect transistor (FET) architecture with two-terminal, back-gate configuration, distinct layer-dependent properties were observed, in agreement with optical characterization studies. As the number of layers increases, the gate control becomes negligible in consonance with decrease in band gap. The electron on/off ratio decreases from  $\sim 10^6$ , for bilayer PdSe<sub>2</sub>, to  $\sim 10^1$ , for bulk PdSe<sub>2</sub>. While the on/off ratio decreases monotonically as the number of layers is increased, the electron mobility peak is at  $\sim 10\text{L}$ , similar to that observed in black phosphorus<sup>6</sup>. Interestingly, PdSe<sub>2</sub> devices maintained their typical ambipolar behavior irrespective of the number of layers, though with an observed shift to become more n-type with a decrease in the number of layers. The semiconductor to semimetal transition from monolayer to bulk PdSe<sub>2</sub> is a promising indication of the ability to fabricate single layer logical junction devices



using PdSe<sub>2</sub> as both the channel and contact<sup>111</sup>, thus, eliminating contact resistance due to scattering and Schottky barriers at the contact interface with the semiconducting channel. Also, the device performance shows that PdSe<sub>2</sub> is stable in air. The fabrication after two months for 10 L and 46 L devices remain largely unchanged.

## 5.2 Device fabrication and architecture

To investigate the transport properties of 2D PdSe<sub>2</sub>, field-effect transistor (FET) devices were fabricated using a two-terminal, back-gate configuration as shown schematically in Fig. 5.1a. The fabrication process starts with exfoliating PdSe<sub>2</sub> flakes onto a degenerately doped Si substrate coated with 280 nm SiO<sub>2</sub>. The details of the exfoliation method have been covered in the previous chapter. Electron-beam (e-beam) lithography is used to pattern source and drain metal contacts, using an e-beam resist (PMMA A495) to protect areas where metals aren't desired. Metal contacts (5nm Ti/30 nm Au) are deposited using electron-beam evaporator in a vacuum of  $\sim 10^{-6}$  Torr at low rate in  $\sim 1$  Å/s. After evaporation, lift-off of excess metal was done by sonicating the device in acetone followed by cleansing with IPA and DI water. A typical final optical image is shown in Fig. 4.1b for three devices with two contacts each. The devices were measured in a vacuum station equipped with BeCu probe tips. Devices were analyzed with Keithley 4200-SCS semiconductor analyzer.

## 5.3 Layer-dependent ambipolar conduction, high mobility and air stability in PdSe<sub>2</sub>

Figure 5.2a shows the plot of the drain current ( $I_{ds}$ ) as a function of back gate voltage ( $V_{bg}$ ) for a typical 5 L PdSe<sub>2</sub> device with 1.0 V drain bias. The linear behavior of the  $I_{ds}$ – $V_{ds}$  characteristics shown in Fig. 5.2(b) indicates good Ohmic contact at room temperature. The device exhibits ambipolar transport with a slight asymmetry between holes and electrons. For this

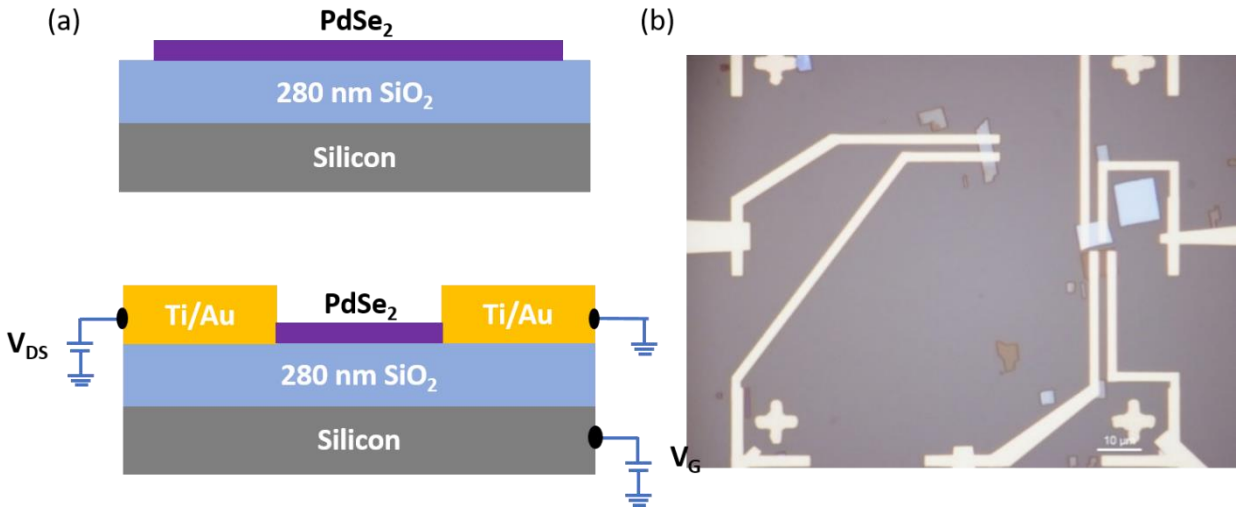


**Figure 5.1.** (a) Fabrication of PdSe<sub>2</sub> FET: PdSe<sub>2</sub> flake is first exfoliated onto the substrate before the deposition of electrodes. (b) Optical image of fabricated devices.

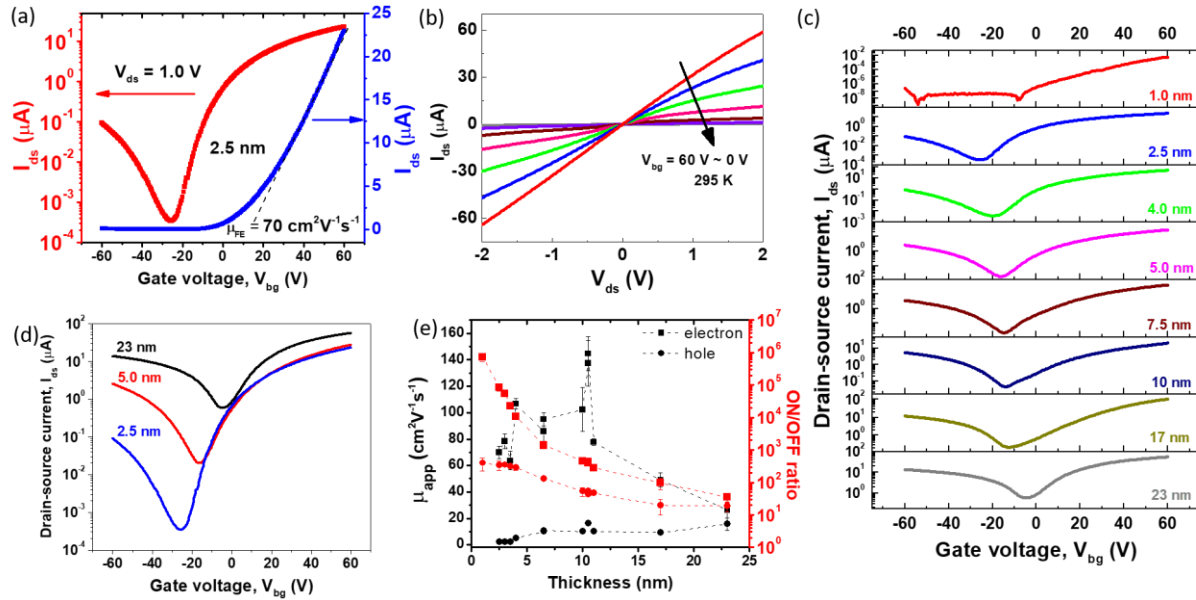


**Figure 5.2.** (a) Transfer curve of a typical  $\sim 5$  L PdSe<sub>2</sub> device, with both logarithmic and linear scales, showing ambipolar characteristics (b) Typical output curves showing linear characteristics at 295 K for 20 L at positive back voltages  $V_{bg} = 60 \text{ V} \sim 0 \text{ V}$ . (c) Drain-source current versus back gate voltage plot for PdSe<sub>2</sub> with different number of layers at  $V_{ds} = 1.0 \text{ V}$  showing ambipolar behavior in all cases at room temperature, with logarithmic plot. (d) Thickness-dependent properties showing increasing off-current with thickness. (e) Electron and hole apparent mobility, and on/off ratio versus flakes thickness for PdSe<sub>2</sub> devices measured at room temperature. Black line indicates mobility curve, while red line indicates on/off ratio curves. Data points in squares and circles represents electron and holes, respectively. The electron mobilities are higher than hole mobilities, and thicker films consistently show lower on/off ratio than that of thinner flakes.

5 L device, electron-apparent field-effect mobility as high as  $70 \text{ cm}^2 \text{ V}^{-1} \text{ s}^{-1}$  was achieved at room temperature and an on/off ratio greater than  $10^5$ . Overall, electron carriers have higher mobilities compared with holes. To elucidate the layer-dependent electrical properties of 2D PdSe<sub>2</sub> crystals, the transfer characteristics for different numbers layers of PdSe<sub>2</sub> were measured and are shown in Fig. 5.2c. Distinct layer-dependent properties were observed in agreement with optical characterization and electronic structure calculations of band gap variation. For example, as the number of layers increases, the gate control becomes negligible, which is consistent with a decrease in band gap. Also, as shown in Fig. 5.2d, the off-current in the channel increases with thickness, probably due to the presence of gate-uncontrollable channel in thick transistor channels. This is displayed in Fig. 5.2e, where the on/off ratio for electrons decreases from  $\sim 10^6$ , for bilayer PdSe<sub>2</sub>, to  $\sim 10$ , for bulk PdSe<sub>2</sub>. A similar trend also can be observed for the on/off ratio for holes. The low on/off ratio ( $<10$ ) observed in bulk PdSe<sub>2</sub> can be associated with a quasi-metallic behavior. While the on/off ratio decreases monotonically as the thickness is increased, the electron mobility peaks at  $\sim 20 \text{ L}$ , similar to that observed in BP.

The statistical analysis for the mobility and on/off ratios of about  $\sim 65$  devices are presented in Fig. 5.3, showing an average electron mobility of  $\sim 80 \text{ cm}^2 \text{ V}^{-1} \text{ s}^{-1}$  with the highest one  $\sim 158 \text{ cm}^2 \text{ V}^{-1} \text{ s}^{-1}$ . Note that these values were measured without any materials treatment or device optimization, so perhaps with further device engineering, mobilities approaching the theoretical predicted value should be expected due to the low effective mass of noble transition metal dichalcogenides. Interestingly, the PdSe<sub>2</sub> devices maintained their typical ambipolar behavior irrespective of the number of layers, with more symmetrical ambipolar behavior with increasing thickness, which is very promising for high-performance 2D logic circuits. The layer dependence of the semiconductor-to-quasi-metal transition in PdSe<sub>2</sub> is also promising for fabricating single-

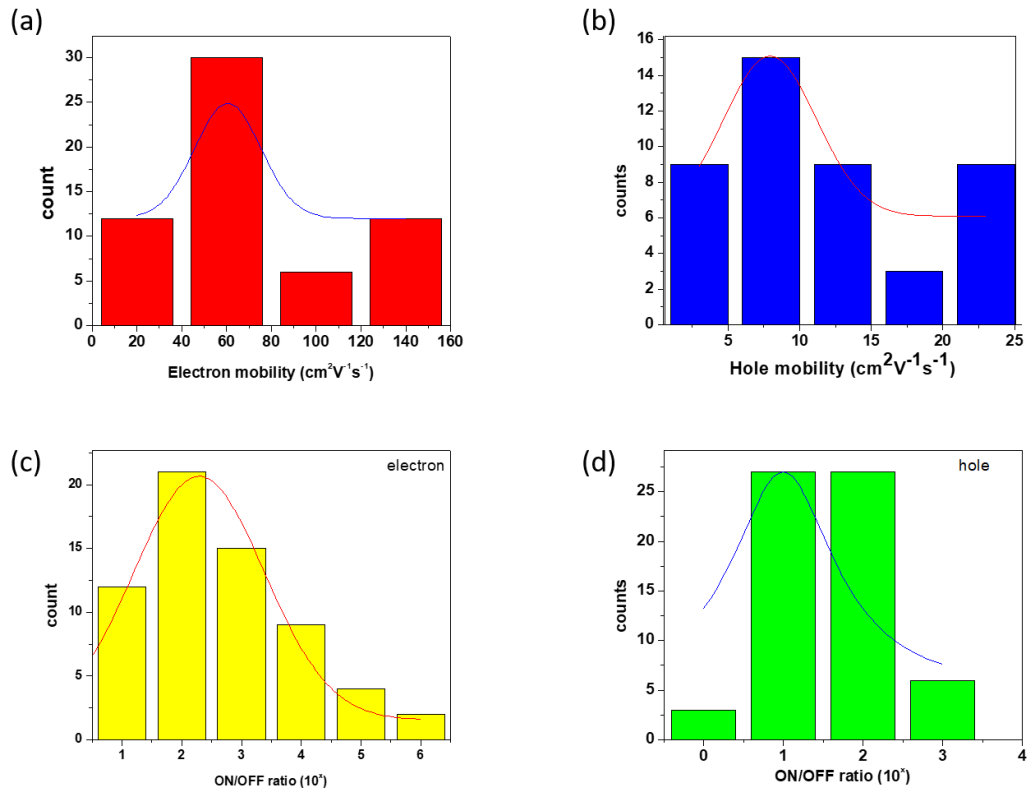


**Figure 5.3.** Statistical analysis of the performance of 65 devices based on (a-b) apparent mobility and (c-d) on/off ratio for electron and hole conduction, respectively.

material logic junction devices using 2D PdSe<sub>2</sub> crystals for both the channel and contact. This would eliminate the contact resistance due to scattering and Schottky barriers at the contact interface with the semiconducting channel. It is important to note that unlike BP, PdSe<sub>2</sub> remains stable (at least up to 60 days for the present measurements) after exposure to air as shown in Fig. 5.4.

The electrical characterization results presented above are all on 280 nm SiO<sub>2</sub> substrates with Ti/Au metal contacts. The performance of 2D devices has been established to be influenced by their environment, namely, metal contacts and support substrates. Figure 5.5 summarizes the transfer characteristics of 20 L PdSe<sub>2</sub> using different metal contact and support substrates. Fig. 5.5(a-b) compares the performance when low-work function Ti is used compared to high work function metal, Pd. The field-effect electron mobility shows an enhancement by a factor of 3. This implies that the work function of Pd aligns better with the conduction band of 20 L PdSe<sub>2</sub>. Generally, for different thickness, samples with Pd contacts result in higher electron mobility, with a pronounced gain in thicker samples. For thinner PdSe<sub>2</sub>, the Ti/Au and Pd contacts have comparable electron mobilities, suggesting that Ti/Au is better suited for thinner devices. Also, bottom and top gate high dielectrics were used in place of SiO<sub>2</sub> as shown in Fig. 5.5(c-d). The use of high dielectrics could help lower the operating voltages which is important for low-power electronics and wearables. The carrier mobility of PdSe<sub>2</sub> is not affected by the substrate, with the value being the same for 280 nm SiO<sub>2</sub> and 50 nm Al<sub>2</sub>O<sub>3</sub>. This is reasonable, as the role of high-dielectric Al<sub>2</sub>O<sub>3</sub> is to lower the sub threshold voltage from ~10 V to ~0.4 V. Similarly, ionic liquid, 1-hexyl-3-methylimidazolium bis(trifluoromethylsulfonyl)imide ([Hmim][TFSI]), was used as a top gate, achieving a lower subthreshold voltage. However, due to the increase in charge carrier

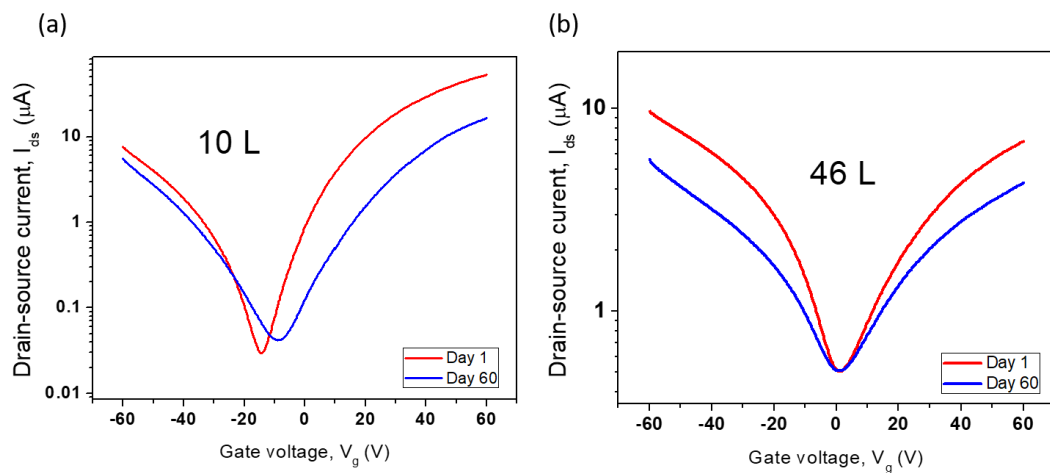


**Figure 5.4.** The transfer curve of pristine PdSe<sub>2</sub> FET and the device after 60 days exposed in air for (a) 10 L (b) 46 L.

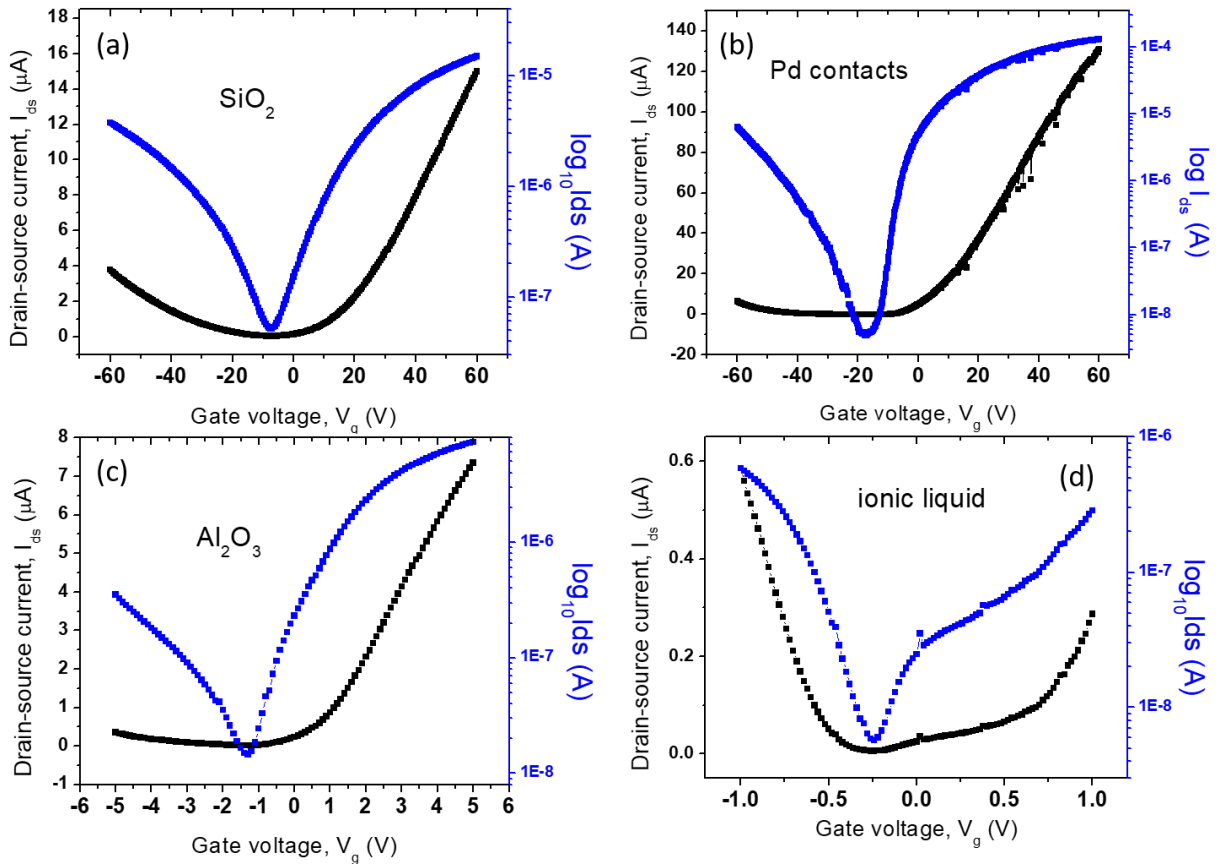


**Figure 5.5.** Transfer characteristics of 20 L PdSe<sub>2</sub> (a) on 280 nm SiO<sub>2</sub> with Ti/Au contacts (b) with high work-function, Pd metal contacts, (c) on 50 nm Al<sub>2</sub>O<sub>3</sub> with Ti/Au contacts, and (d) with ionic-liquid top gate. The voltage bias used in (a-b) is 1.0 V, and 0.1 V for (c-d).



injection in the channel as a result of the ionic liquid, the device performance was expected to be enhanced. Further studies still need to be carried out to understand the mechanism and results of carrier introduction into 2D PdSe<sub>2</sub> semiconducting channel.

#### 5.4 Temperature-dependent properties in PdSe<sub>2</sub>

Temperature dependence measurements were carried out on few-layer PdSe<sub>2</sub> to understand the mechanism governing charge-carrier transport. The  $I_{ds}$ - $V_{ds}$  output characteristics of 46 L device at different gate bias is shown in Fig. 5.6 at 300K (a) and at 16K (b). The linear behavior is maintained down to 16 K for hole carriers. The slight nonlinearity for the positive bias at 16 K suggests the presence of Schottky barrier at semiconductor-metal contact junction, which results in the increase of contact resistance for electrons carriers. Similar observations were made for thinner devices for both hole and electron carriers.

Fig. 5.7a shows the temperature dependence of the carrier mobility in 10 L PdSe<sub>2</sub> which is similar to that found in other layered materials; the carrier mobility decreases at temperatures higher than ~100 K and saturates (or decrease slightly) at lower temperature. The behavior of the mobility at low temperature is most likely due to the dominant charged impurity scattering mechanism. As the temperature increases, the mobility decreases due to phonon scattering, following a power law relation  $\mu \sim T^{-\gamma}$ , where  $\gamma$  is close to 0.24. The  $\gamma$  value for few layer PdSe<sub>2</sub> is notably smaller than values in other 2D materials such as monolayer MoS<sub>2</sub> ( $\gamma \approx 1.40$ ; ref. <sup>112</sup>), but agrees with that in few layer BP ( $\gamma \approx 0.5$ ; ref. <sup>56</sup>) and monolayer MoS<sub>2</sub> with double dielectric layers ( $\gamma \approx 0.3$ ; ref.<sup>113</sup>). The decrease in the value of  $\gamma$  with number of layers as shown in Fig. 5.7b may be attributed to the suppression of the homopolar phonon modes due to the strong interlayer

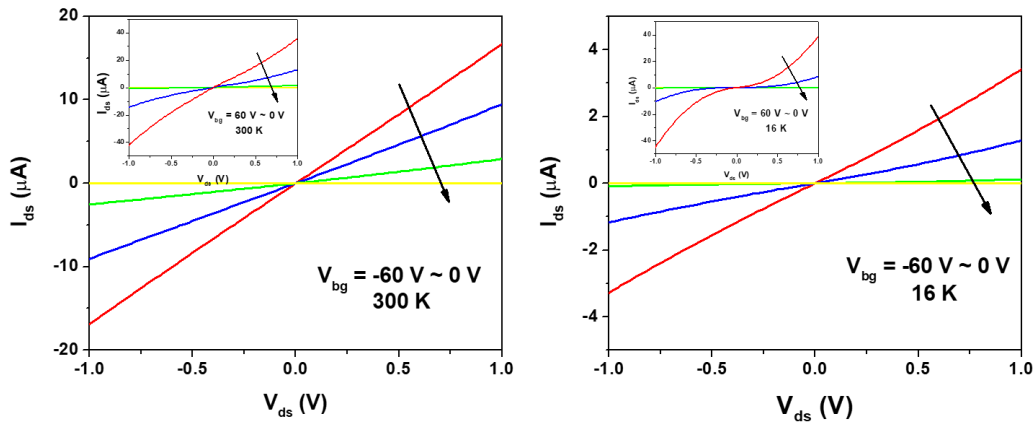


**Figure 5.6.** (a) Drain-source current ( $I_{ds}$ ) versus voltage ( $V_{ds}$ ) at negative back voltages  $V_{bg} = -60$  V  $\sim$  0 V showing linear characteristics at 300 K. The inset shows a similar characteristic at positive back voltages  $V_{bg} = 60$  V  $\sim$  0 V, confirming the ambipolar characteristics of PdSe<sub>2</sub>. (b)  $I_{ds}$  -  $V_{ds}$  characteristics at 16 K, for negative back voltages. Inset shows for positive back voltages. (All measurements were from a 46 L PdSe<sub>2</sub>).

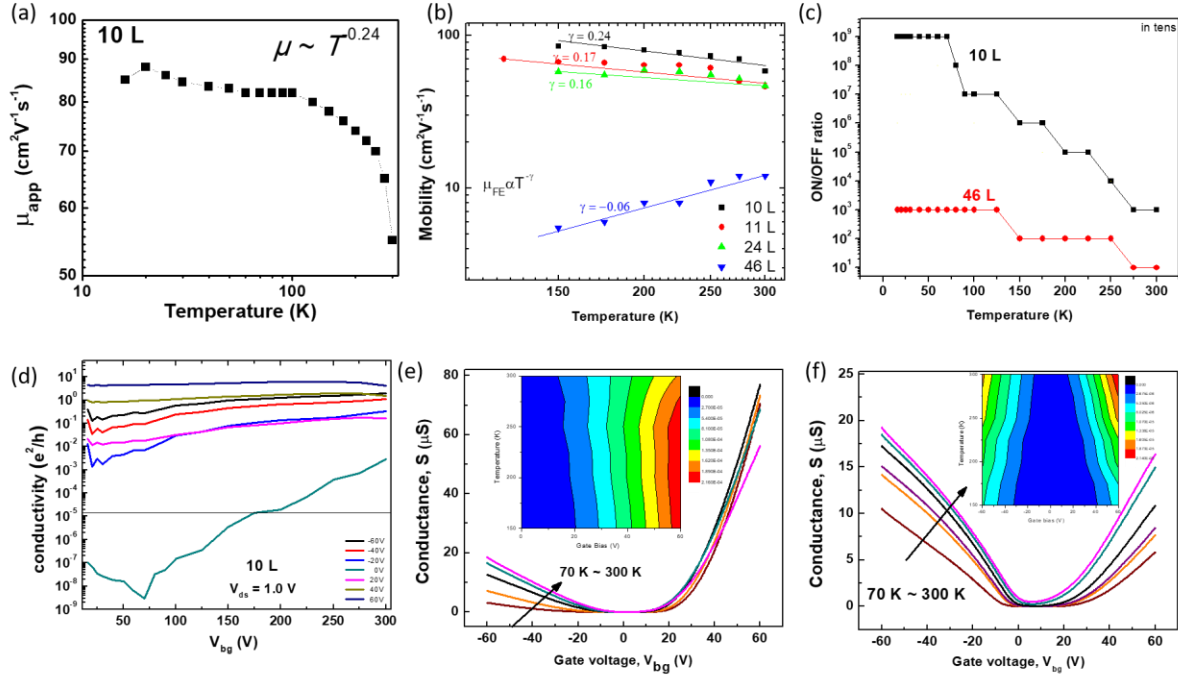


**Figure 5.7.** (a) The electron apparent mobilities measured at different temperatures for PdSe<sub>2</sub> flakes with a thickness of 10 L. Below 100 K, the mobilities are independent of temperature, but above 100 K, the mobilities decrease with increasing temperature due to the phonon scattering, following a  $T^{-\gamma}$  dependence with  $\gamma$  close to 0.24. (b) Log-log plot of mobility as a function of the temperature for different number of layers through two-terminal configuration. The power-law coefficient,  $\gamma$  is extracted from the slope of the graph, which reveals phonon scattering mechanism for few-layers, and scattering by charged impurities for several layers. (c) Plot of on/off ratio (rounded to the nearest tens) with temperature for 10 L and 46 L PdSe<sub>2</sub>. (d) Plot of temperature dependence of the two-terminal conductance at different gate voltages for 10 L device. (e-f) Conductance as a function of gate voltage for different temperatures for PdSe<sub>2</sub> flakes with a thickness of 10 L and 46 L, respectively. The crossing around  $\sim 40$  V for the 10 L device indicate the change in temperature dependence which is absent in the 46 L device. Inset shows the color plot of the conductance as a function of temperature and gate bias.

interaction in layered PdSe<sub>2</sub>. For several layer PdSe<sub>2</sub>, phonon modes have been fully quenched resulting  $\gamma \sim 0$ , making the dominant scattering mechanism charge impurity. This is due to the increase in charge carrier concentrations with number of layers. Further theoretical and experimental work is needed to clarify the detailed mechanism.

In addition, an increase in current modulation up to  $>10^9$  is observed for few-layer PdSe<sub>2</sub> as temperature is lowered (see Fig. 5.7c). The plot of the temperature dependence of the two-terminal conductivity at different gate bias for the 10 L device is shown in Fig 5.7d. With  $V_{bg} < 40$  V, the conductivity of the 10 L device decreases with decreasing temperature, indicating insulating behavior, whereas for  $V_{bg} > 40$  V, the temperature dependence is reversed, showing metallic behavior. The crossover from insulating to metallic conductance is shown in more detail in Fig 5.7e. Interestingly, this gate-bias induced metal-insulator transition (MIT) behavior was only observed in thinner devices (i.e.,  $< 24$  L). For thicker PdSe<sub>2</sub> devices, the conductance always increases with increased temperature at all gate bias (Fig. 5.7f) suggesting there is no MIT in thick flakes of PdSe<sub>2</sub>. This MIT behavior could be a result of quantum interference effects of weak and strong localization.

Strong localization occurs at the insulating state due to low carrier concentration, and weak localization occurs at the metallic state as a result of high carrier concentration. However, the conductivity of the 46 L device increases with temperature (insulator behavior) at all gate biases suggesting a threshold thickness for the transition (see inset of Fig. 5.7f for the color plot) which is estimated to be  $\sim 24$  L. Strong electron-electron interaction has been suggested as the reason for the metal-insulator transition in low-disordered 2D systems, which arises as the system is quantum confined to two dimensions<sup>112</sup>. The strength of this correlation is characterized by the Wegner-Seitz radius given as:

$$r_s = \frac{n_v}{a_B^* \sqrt{\pi n_{2D}}} = \frac{m^* e^2 n_v}{4\pi \epsilon \hbar^2 \sqrt{\pi n_{2D}}} \quad (5.1)$$

where  $n_v$  is the number of degenerate valleys in the spectrum,  $a_B^* = (4\pi\epsilon\hbar^2)/(m^*e^2)$  is the effective Bohr radius, with  $\epsilon$  being the dielectric constant and  $m^*$  is the effective electron mass. For a system in which  $r_s \ll 1$ , the scaling theory of localization is valid. However, this is not true when  $r_s \gg 1$  which is a characteristic for strongly interacting systems. For monolayer MoS<sub>2</sub><sup>112</sup> and ReS<sub>2</sub><sup>114</sup>,  $r_s \gg 1$ , similar to the values obtained for our PdSe<sub>2</sub> samples ( $\sim 6.3$  for few-layer systems, and  $\sim 2.8$  for several-layer systems). This value was obtained considering the effective mass of electron  $m^* = 0.28 - 0.52$ , while dielectric constant,  $\epsilon$ , 1.7 times that of MoS<sub>2</sub> ( $\sim 12.5\epsilon_0$ )<sup>115</sup>. This confirms that few-layer PdSe<sub>2</sub> have stronger Coulomb interactions. Ioffe–Regel criterion predicts the existence of a MIT when  $k_F \cdot l_e$  satisfies the criterion  $k_F \cdot l_e \sim 1$ , with the Fermi wave vector  $k_F = (2\pi n_{2D})^{1/2}$ , and mean free path of electrons  $l_e = \hbar k_F \sigma / n_{2D} e^2$ . According to this criterion, for  $k_F \cdot l_e \gg 1$  the phase is metallic whereas for  $k_F \cdot l_e \ll 1$ , the phase is insulating. For our devices, at the crossing point of  $V_g = 40$  V (corresponding to  $n_{2D} = 1.87 \times 10^{12} \text{ cm}^{-2}$ ), we have  $k_F \cdot l_e \sim 4.8$ , similar to that in few-layer MoS<sub>2</sub> ( $\sim 2.84$ )<sup>113</sup>. For thicker devices,  $k_F \cdot l_e$  is less than 1, showing a continuous insulating phase.

## 5.5 Anisotropic properties of PdSe<sub>2</sub>

PdSe<sub>2</sub> has a unique structure that is anisotropic in-plane. This structural anisotropy translates to some very interesting orientation-dependent vibrational, optical and electrical properties. Here, directional characterization and analysis of the phonon, non-linear optical and electrical properties in PdSe<sub>2</sub> are presented. Using polarization dependent Raman experiments coupled with Raman polarization modeling, under parallel laser configuration, the A<sub>g</sub> and B<sub>1g</sub> Raman modes exhibit distinctly different polarization profiles, which enable their

differentiation. Also, second harmonic generation (SHG) was performed with SHG detection polarization parallel to the excitation laser polarization, showing a two-fold symmetry for even-layered PdSe<sub>2</sub>. Lastly, a complementary radially contacted field effect transistor (FET) was fabricated in order to measure orientation-dependent electrical properties. Mobility and transconductance followed a sinusoidal-like dependence on orientation. Correlating these results show that Raman and SHG methods might be used as a nondestructive technique to orient PdSe<sub>2</sub> devices for optimum performance.

### 5.6.1 Raman spectroscopy

As discussed in chapter 3, A<sub>g</sub> and B<sub>1g</sub> Raman modes can be observed in back-scattering Raman measurements, and their Raman tensors  $\tilde{R}$  are

$$\tilde{R}(A_g) = \begin{pmatrix} a & \cdot & \cdot \\ \cdot & b & \cdot \\ \cdot & \cdot & c \end{pmatrix}, \quad \tilde{R}(B_{1g}) = \begin{pmatrix} \cdot & d & \cdot \\ d & \cdot & \cdot \\ \cdot & \cdot & \cdot \end{pmatrix}. \quad (5.2)$$

In the experimental back-scattering laser geometry (light Z in and Z out), the electric polarization vectors of the incident and scattered light  $\mathbf{e}_i$  and  $\mathbf{e}_s$  are in-plane (the X-Y plane), and they are given by  $\mathbf{e}_i = (\cos\theta, \sin\theta, 0)$  and  $\mathbf{e}_s = (\cos\gamma, \sin\gamma, 0)$ . Since Raman intensity  $I \propto |\mathbf{e}_i \cdot \tilde{R} \cdot \mathbf{e}_s^T|^2$ , it follows that

$$I \propto \left| (\cos\theta, \sin\theta, 0) \tilde{R} \begin{pmatrix} \cos\gamma \\ \sin\gamma \\ 0 \end{pmatrix} \right|^2. \quad (5.3)$$

Substituting the Raman tensors  $\tilde{R}$  from Eq. 5.2 into Eq. 5.3, we have

$$I(A_g) \propto |b|^2 \left| \frac{a}{b} \cos\theta \cos\gamma + \sin\theta \sin\gamma \right|^2, \quad I(B_{1g}) \propto |d|^2 \sin^2(\theta + \gamma). \quad (5.4)$$

In the parallel polarization configuration,  $\gamma = \theta$ , and thus

$$I(A_g) \propto |b|^2 \left| \frac{a}{b} \cos^2 \theta + \sin^2 \theta \right|^2 \propto |b|^2 \left| \left( \frac{a}{b} - 1 \right) \cos^2 \theta + 1 \right|^2,$$

$$I(B_{1g}) \propto |d|^2 \sin^2(2\theta). \quad (5.5)$$

On the other hand, in the cross-polarization configuration,  $\gamma = \theta + 90^\circ$ , which gives  $\cos\gamma = -\sin\theta$  and  $\sin\gamma = \cos\theta$ . Subsequently, we have

$$I(A_g) \propto |b|^2 \left| -\frac{a}{b} \cos\theta \sin\theta + \sin\theta \cos\theta \right|^2 \propto |(b-a) \sin\theta \cos\theta|^2 \propto \frac{|b-a|^2}{4} \sin^2(2\theta)$$

$$I(B_{1g}) \propto |d|^2 \sin^2(2\theta + 90^\circ) \propto |d|^2 \cos^2(2\theta). \quad (5.6)$$

According to Eq. 5.5, the  $A_g$  mode exhibits an intensity variation period of  $180^\circ$  under the parallel configuration, where the maximum intensity direction depends on the ratio of  $\frac{a}{b}$ , as shown in Fig. 5.8a. Similar results can be found for anisotropic black phosphorus.<sup>105,116</sup> According to Eq. 5.6, the period of the  $A_g$  mode changes to  $90^\circ$  under the cross configuration (Fig. 5.8a). On the contrary, for the  $B_{1g}$  mode, the intensity variation period is  $90^\circ$  under both polarization configurations. Nevertheless, there is a  $45^\circ$  phase difference between the two polarization profiles of the  $B_{1g}$  mode, as illustrated in Fig. 5.8b. In short, under the experimental parallel laser configuration, the  $A_g$  and  $B_{1g}$  Raman modes exhibit distinctly different polarization profiles (Fig. 5.8a), which enable their differentiation.

As discussed in previously, bulk PdSe<sub>2</sub> has 3  $A_g$  Raman modes ( $A_g^1$ ,  $A_g^2$ ,  $A_g^3$ ) and 3  $B_{1g}$  Raman modes ( $B_{1g}^1$ ,  $B_{1g}^2$ ,  $B_{1g}^3$ ), and they are still Raman active in NL systems. In addition, many Raman-inactive modes in the bulk become activated in few-layer systems due to symmetry reduction, giving rise to new peaks in few-layer samples. As shown in Fig. 5.9 for the LF Raman,  $A_g^1$  (P5) and  $B_{1g}^1$  (P'5) modes are very close to each other and thus often appear as a single mixed

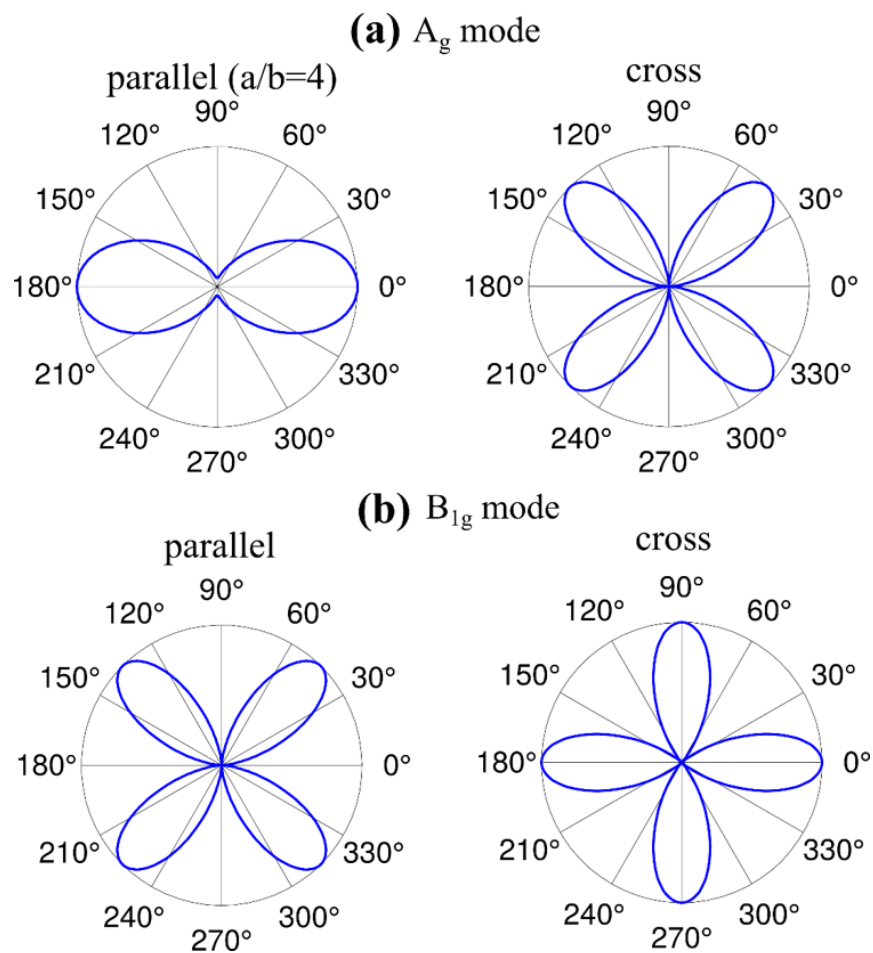


**Figure 5.8.** Theoretical polarization diagrams for (a)  $A_g$  symmetry and (b)  $B_{1g}$  symmetry Raman modes of PdSe<sub>2</sub> in parallel  $z(xx)\bar{z}$  and cross  $z(xy)\bar{z}$  polarization configurations.



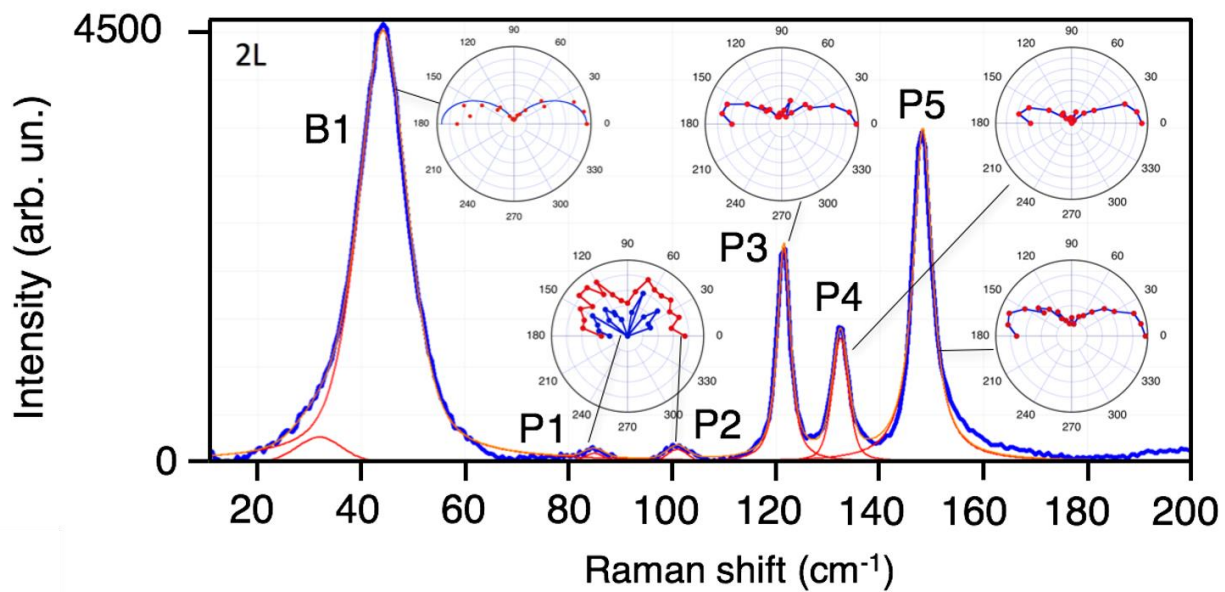


**Figure 5.9.** The major Raman peaks for 2L PdSe<sub>2</sub> measured in polarization configuration. Inserts show polar plots of Raman intensities versus polarization angles measured by rotating the sample.

peak around  $146\text{ cm}^{-1}$  in unpolarized Raman measurements. Additional new Raman peaks are noticeable on the left of the  $A_g^1$  peak (P5), with parallel polarization showing two-fold symmetry for the  $A_g$  peaks as expected from theory.

### 5.6.2 Structure anisotropy characterized by second-harmonic generation (SHG)

Nonlinear optics involves processes in which coherent light particles change their properties, such as their frequency, when they pass through an optical medium. For example, the frequency of a photon can double or triple, leading to the generation of second- or third-order harmonics, respectively. Second harmonic generation (SHG) is the basis of frequency doubling which is the phenomenon behind all-optical devices employing self-phase modulation and four-wave mixing<sup>117</sup>. For a material to exhibit SHG, absence of inversion symmetry is required since it is a second-order parametric process. Atomically-thin 2D materials with nonlinear optical properties have potential in quantum applications for the generation and manipulation of non-classical light<sup>118</sup>.

For some 2D materials, SHG was observed in odd-layered TMDs, which disappears in even-layered TMD due to the restoration of inversion symmetry<sup>119</sup>. In contrast, due to the crystal structure of  $\text{PdSe}_2$ , even layers lack inversion symmetry, which is absent in odd layers and bulk as described in chapter 3. Confocal laser scanning microscopy with wavelength  $\sim 800\text{ nm}$  was used to characterize the second harmonic response from  $\text{PdSe}_2$  with different thickness. As shown in the SHG spectra of Fig. 5.10a, SHG intensity shows up around half of the incident wavelength, which corresponds to frequency doubling. The intensity from even-layered  $\text{PdSe}_2$ , shown in Fig. 5.10b was more pronounced than that from odd-layers due to the non-centrosymmetric nature of their crystal structure. Figure 5.10c shows the optical image of a  $\text{PdSe}_2$  with even- and odd-number layer (4L on the left and 3L on the right) with the corresponding SHG intensity map shown in

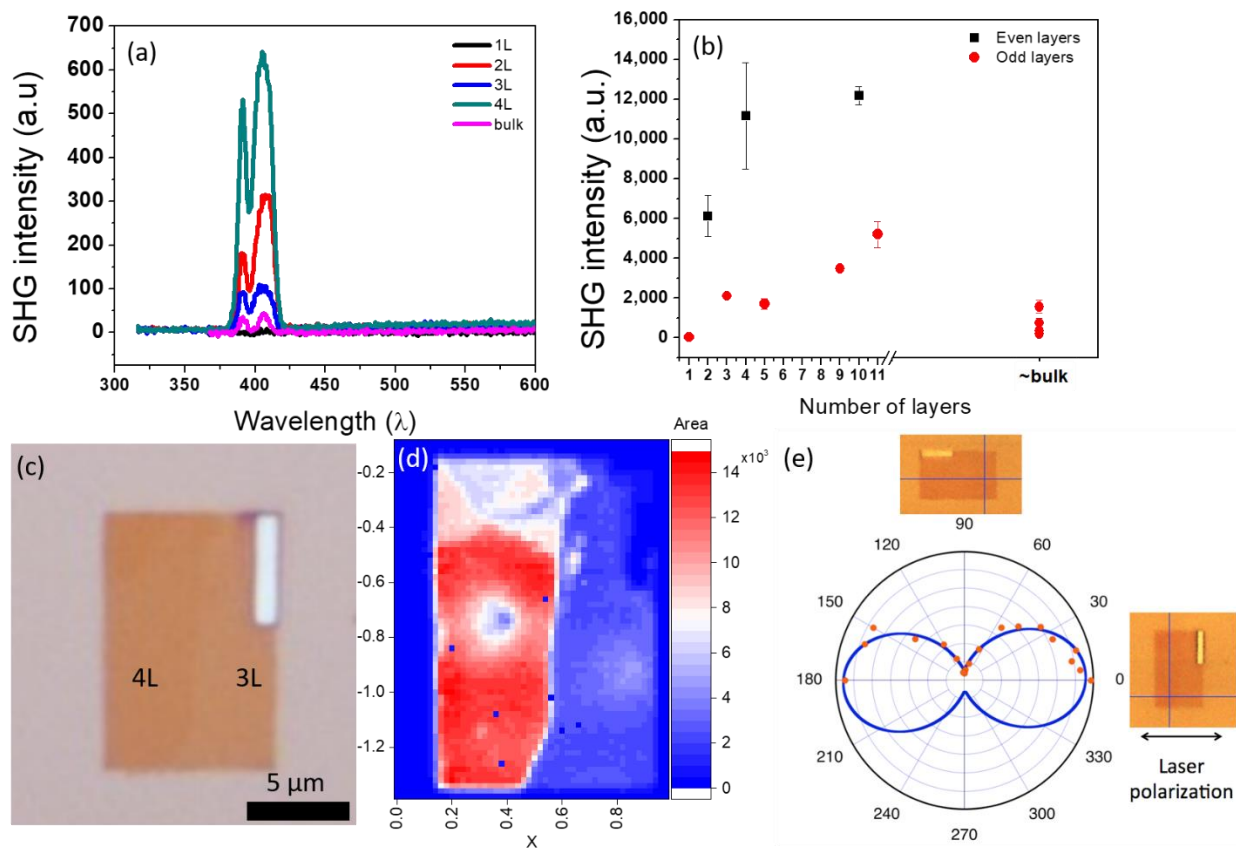


**Figure 5.10.** (a) Second harmonic generation (SHG) spectrum from PdSe<sub>2</sub> thin layers with different layer number (800 nm wavelength laser was utilized). (b) The SHG intensity as a function of layer number. (c) Optical image of PdSe<sub>2</sub> with 4L and 3L regions. (d) SHG map of the PdSe<sub>2</sub> crystal showing intense SHG signal for 4L part of the crystal and almost no signal for the 3L part. (e) Integrated intensity of the SHG spectrum (from 380 to 420 nm) versus a rotation angle relative to the laser polarization. Two inserts show optical images of the PdSe<sub>2</sub> crystal corresponding to 0° (right) and 90° (top) crystal orientations relative to the laser polarization. The blue line shows fit with  $A+B\cos 2\alpha$  where  $A=5925$  and  $B=628$ .

Fig. 5.10d. The SHG map shows that the 4L part has a strong SHG signal with almost no signal observed from the 3L part. As shown in Fig. 5.10e the SHG polarization diagram can be fit with  $\cos^2\alpha$ , where  $\alpha$  is an angle between laser polarization and crystal orientation with its  $0^\circ$  position shown in Fig. 5.10c. This two-fold symmetry displayed in even-layer PdSe<sub>2</sub> is similar to that observed in black phosphorus.<sup>105,116</sup> Note that in this case the SHG detection polarization is parallel to the excitation laser polarization. The presence of low-symmetry anisotropy in PdSe<sub>2</sub> aids the rapid identification of crystal orientation from optical characterizations.

### 5.6.3 Anisotropic electrical behavior of 2D PdSe<sub>2</sub>

To probe the orientation-dependence of the electrical properties of PdSe<sub>2</sub>, angular transconductance and field effect mobility measurements were performed using a two-terminal probe configuration. Fig. 5.11a shows the optical image of a typical PdSe<sub>2</sub> flake patterned with metal contacts at different angles. Fig. 5.11d shows the plot of transconductance and mobility as a function of angle. The transconductance ( $G_m = dI_{ds}/dV_g$ ) and field-effect mobility were estimated from the linear portion of the transfer curves measured. A clear dependence on crystallographic orientation is observed with a two-fold symmetry, similar to the anisotropy properties seen in the Raman spectroscopy and SHG experiments. The angular dependence is fit with a sinusoidal curve, with characteristic wavelength of  $\pi$  and a maximum at around  $90^\circ$ . The  $G_m$  ranges from 0.467 to 0.622  $\mu\text{S}$  and  $\mu\text{FE}$  from 169 to 180  $\text{cm}^2/\text{Vs}$ , which correspond to a  $\sim 33\%$  and  $\sim 7\%$  anisotropy in the transconductance and mobility, respectively. The discrepancy in the measurements might be as a result of the simple device structure used which can be affected by current spreading. The maximum electron mobility is achieved along the puckered axis as shown in the schematic and STEM image of Fig. 5.11(b-c). This puckered axis is similar to the arm-chair direction in black phosphorus, where effective electron mass is lowest. It's expected that like black phosphorus, the

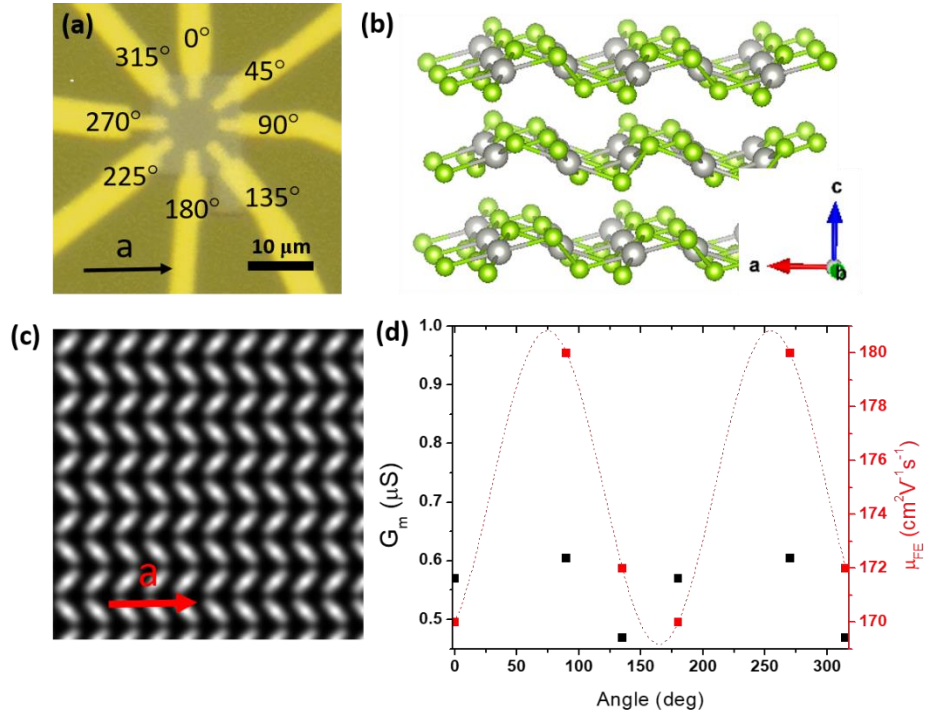


**Figure 5.11.** (a) Optical image of the device with the angular orientation. (b) Schematic of the crystal structure along the puckered axis. (c) STEM image showing the zigzag puckered structure. (d) Angular dependence transconductance and field-effect mobility.

driver of the anisotropy in electrical performance will be the difference in the effective mass along different angular orientations. Further studies are needed to provide a clearer understanding. Regardless, in order to achieve optimum electrical performance, devices should be constructed across the a-direction.

## 5.6 Summary

In summary, field-effect transistor (FET) devices of mono- and few-layer PdSe<sub>2</sub> crystals were successfully fabricated and characterized. 2D PdSe<sub>2</sub> exhibits an ambipolar characteristics, with decreasing relative n-type conduction with layer number. PdSe<sub>2</sub> shows layer-dependent and tunable electrical properties with broad-range of applications including FET active channel, CMOS, digital inverters, comparators, and FET contacts. More importantly, PdSe<sub>2</sub> exhibits a high carrier field-effect mobility  $\sim 158 \text{ cm}^2/\text{Vs}$  and high on/off ratio as high as  $10^6$ . Unlike black phosphorus, PdSe<sub>2</sub> is relatively stable in air, with little changes in device performance over a period of 60 days. Through device engineering, it was revealed that the performance of PdSe<sub>2</sub> transistors can be optimized to achieve higher carrier mobilities with Pd metal contacts, and a low operating voltage using high dielectric substrates. Temperature-dependent studies reveal a metal-insulator transition in few-layer PdSe<sub>2</sub> which is absent in several-layer systems. Finally, through Raman spectroscopy, SHG and angular-device characterization, the low-symmetry in PdSe<sub>2</sub> was confirmed which can be used for the determination of the crystal orientation. The unique characteristics exhibited by this material will spark interest making it a promising candidate for 2D layered electronics.

## Chapter 6: Vacancy-induced phase transition in layered PdSe<sub>2</sub>

### 6.1 Introduction

Phase transformation has occupied an important subject/area in the field of material science, due to its ability to realize new phases and materials which can extend the knowledge of material properties and their capabilities. Through a change in temperature and pressure, conventional phase transitions have been observed between states of matter (including solid, liquid and gas) with corresponding structural and electronic changes. In two-dimensional layered materials, structural transformations have been reported to induce metal-insulator transition, charge-density waves, and superconducting states.<sup>20</sup> Unlike monolayered graphene, hBN and black phosphorus, 2D materials which have a transition metal sandwiched between two chalcogen atoms exhibit structural polymorphs. For example, 2H-MoS<sub>2</sub> which is semiconducting has shown a transformation to metallic 1T-MoS<sub>2</sub> phase under electron-beam irradiation.<sup>120</sup> This 2H/1T phase transition involves gliding atomic planes of Sulphur and/or molybdenum and requires an intermediate phase as a precursor. Also, laser-induced phase patterning has been used to achieve metallic monoclinic 1T'-MoTe<sub>2</sub> from semiconducting hexagonal 2H-MoTe<sub>2</sub>. However, the structural transformation is triggered by Te-vacancies.<sup>121</sup> Identically, chalcogen vacancies have induced phase transformation of SnS<sub>2</sub> to SnS, SnSe<sub>2</sub> to SnSe and PdSe<sub>2</sub> to Pd<sub>2</sub>Se<sub>3</sub>.<sup>122,123</sup> In addition to gliding of atomic planes, and chalcogen vacancies, electrostatic doping, strain and pressure can induce structural phase transition in layered TMDs.<sup>124-126</sup>

Palladium diselenide (PdSe<sub>2</sub>) is a rediscovered 2D material that has garnered attention due to its unique pentagonal structure, strong interlayer interaction, excellent electronic properties and relative stability in air.<sup>127,128</sup> PdSe<sub>2</sub> belongs to group 10 transition metal dichalcogenide, with varying bandgap from ~0 – 1.3 eV depending on the thickness from bulk to monolayer.<sup>127</sup> In

addition to its widely tunable electronic properties as a result of layer dependence, PdSe<sub>2</sub> is rich in polymorphic phases which can provide an extra degree of freedom due to structural transformation. Known related phases of PdSe<sub>2</sub> include: orthorhombic PdSe<sub>2</sub>, PdS-type tetragonal PdSe, cubic Pd<sub>17</sub>Se<sub>15</sub>, orthorhombic Pd<sub>7</sub>Se<sub>4</sub>, monoclinic Pd<sub>34</sub>Se<sub>11</sub>, monoclinic Pd<sub>7</sub>Se<sub>2</sub>, tetragonal  $\alpha$ Pd<sub>4</sub>Se, and trigonal Pd<sub>9</sub>Se<sub>2</sub> with increasing relative Pd composition.<sup>129</sup> Recently, J. Lin, et. al demonstrated that the removal of Se atoms in PdSe<sub>2</sub> can result in the welding of two bulk monolayers to form novel-Pd<sub>2</sub>Se<sub>3</sub> by electron irradiation.<sup>122</sup> A loss of one-fourth of the Se atoms induced stronger interlayer interactions which results in the formation of Pd<sub>2</sub>Se<sub>3</sub>. Due to the many polymorphic phases, unlike most 2D TMDs, multiple PdSe<sub>2</sub> relative phases can be achieved by Se atom removal. For example, hypothetically, a loss of ~50% of the original Se atoms should lead to PdSe or Pd<sub>17</sub>Se<sub>15</sub>.

## 6.2 Phase-transition mechanism in PdSe<sub>2</sub>

The ability of high-energy particles to induce atomic displacements in few-layer materials raises the possibility that layered PdSe<sub>2</sub> could be controllably converted to one of more of its polymorphic phases. The shorter interlayer distance allows for an ease in atomic reconfiguration after removal of Se atoms. Atomic combination of atomic-resolution electron microscopy and ab initio calculations could reveal possible intermediate phases, as well as the final phases. Also, these methods could provide a detailed understanding of defect formation and interaction mechanisms, as well as phase interconversion pathways in PdSe<sub>2</sub>. Also, since the less Se-containing phases are metallic in nature, they can be used to design Ohmic contacts for semiconducting PdSe<sub>2</sub> devices. In this experiment, argon plasma from Oxford's reactive ion etching (RIE) metal etcher at 50W RF power was used, which has a corresponding etching rate of ~2 nm/sec. Pristine samples were protected using PMMA patterned through electron-beam lithography, which is then dissolved in



acetone and IPA after irradiation. Fig. 6.1a shows the optical image of ~40 nm pristine PdSe<sub>2</sub> before and after part of it was exposed to Ar<sup>+</sup> plasma irradiation. The exposed area was etched down to ~10 nm, with visible difference in optical contrast. To investigate the properties of the irradiated regions in comparison with the pristine areas, Z-contrast atomic-resolution and cross-sectional STEM and DFT calculations were used to identify the structure of the irradiated PdSe<sub>2</sub>, Raman spectroscopy was used to identify atomic vibrations, Nano-Auger electron spectroscopy was used to identify and quantify atomic composition, while electrical characterization was carried using a two-terminal field-effect transistor (FET) device configuration.

### 6.3 Structural properties of PdSe<sub>2</sub> and the new phase

The atomic structure of the pristine and plasma-irradiated PdSe<sub>2</sub> flakes were characterized by scanning transmission electron microscopy (STEM). Fig. 6.1b shows the SEM image of a typical sample after transferring on TEM grid. The left and right regions are the pristine and irradiated parts, respectively. A sharp interface between the two regions can be observed, which is made possible by the lithography patterning and covering of the pristine part with PMMA e-beam resist. Fig. 6.1c shows that the atomic structure of the pristine region agree very well with the structures earlier reported.<sup>127</sup> However, the atomic structure of the plasma-irradiated region deviated from that of the pristine region, indicating that the material has undergone phase transformation. The schematic of the phase transformation process is shown in Fig. 6.1d, where the pristine, PMMA-covered PdSe<sub>2</sub> retains its structure. However, due to the Ar<sup>+</sup> ion bombardment, a partial phase transformation takes place, which with a longer irradiation exposure result in a total conversion of the structure. The ADF images of the new phase appears very different from the few-layer PdSe<sub>2</sub> crystals as shown in Fig. 6.1(e-f). The atomic structure observed is that of Pd<sub>17</sub>Se<sub>15</sub> which agree well with the image simulations of shown in

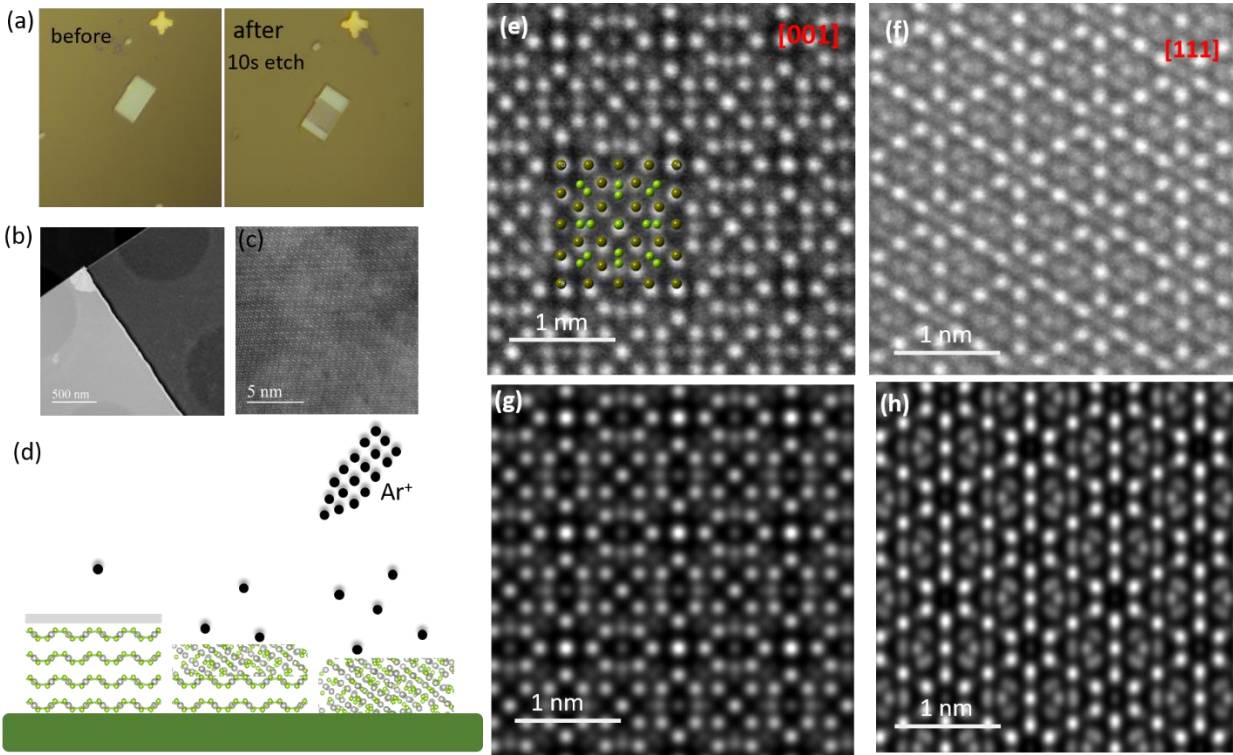


**Figure 6.1.** (a) Optical image of  $\sim 40$  nm thick PdSe<sub>2</sub> before and after 10s argon plasma treatment. (b) Scanning electron microscope (SEM) image of pristine and irradiated PdSe<sub>2</sub> on TEM grid. (c) Atomic resolution STEM image of pristine PdSe<sub>2</sub>. (d) Schematic diagram depicting the phase transformation process. (e-f) Atomic resolution structure of irradiated PdSe<sub>2</sub> crystals revealed by Z-contrast STEM images and corresponding simulated images (g-h). Inset in (e) shows atomic models of the STEM image.

Fig. 6.1(g-h), respectively. Bulk  $\text{Pd}_{17}\text{Se}_{15}$  crystals exhibit  $Pm\bar{3}m$  space group symmetry and  $m\bar{3}m$  point group symmetry. In contrast, with  $\text{PdSe}_2$  which has an orthorhombic lattice that contains four Pd and eight Se atoms in one-unit cell,  $\text{Pd}_{17}\text{Se}_{15}$  is a cubic lattice in which its unit cell is almost 9 times that of  $\text{PdSe}_2$ . Also, the new phase is isotropic in nature unlike anisotropic  $\text{PdSe}_2$  and has 0 eV bandgap.

The phase transformation process is thought to be induced by the removal of Se atoms from the lattice due to  $\text{Ar}^+$  bombardment as previously reported for  $\text{SnS}(\text{Se})_2$ .<sup>123</sup> Similarly, the removal of Se atoms from the lattice of bilayer  $\text{PdSe}_2$  has been shown to lead to  $\text{Pd}_2\text{Se}_3$  due to exposure to electron-beam.<sup>122</sup> Therefore, with varying treatment method and parameters,  $\text{PdSe}_2$  can be transformed into new materials, especially since it has many rich phases, unlike most 2D materials. The phase transformation is aided by the short interlayer distance present in  $\text{PdSe}_2$ , which induces a structural reconstruction after Se atoms removal. In addition to the phase transformation, the original material undergoes thinning as shown in Fig. 6.1d, reasonably due to the amount of Se atoms (about ~50%) that have been removed from the lattice.

Fig. 6.2a shows a cross-sectional STEM examination of a partially-converted  $\text{PdSe}_2$ . The new phase appears perpendicular to the etching direction. Fig. 6.2(b-c) shows the cross-sectional atomic structure of  $\text{PdSe}_2$  and  $\text{Pd}_{17}\text{Se}_{15}$ , respectively. The distinct interface of the phase transformation is shown in Fig. 6.2d. The possible reaction surface is shown in the schematics of Fig. 6.2e with  $\text{Pd}_{17}\text{Se}_{15}$  having a different orientation from the original  $\text{PdSe}_2$  phase similar to that reported for  $\text{SnS}_2$  to  $\text{SnS}$ .<sup>123</sup> The corresponding fast Fourier transform (FFT) patterns of the  $\text{Pd}_{17}\text{Se}_{15}$  phase is shown in Fig. 6.2f which indicates the cubic structure with diffraction patterns of  $(220)$ ,  $(3\bar{2}\bar{2})$  and  $(4\bar{1}\bar{2})$ , confirming the crystallinity of the new phase.

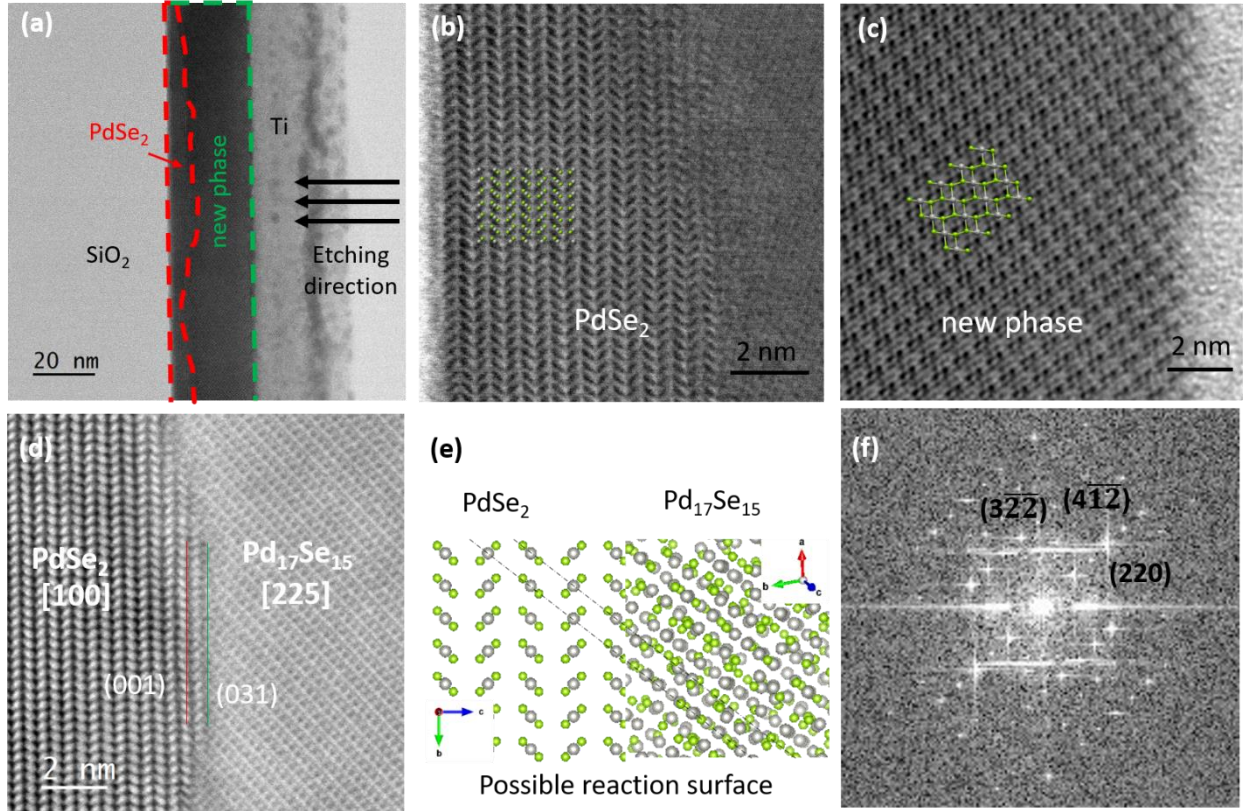


**Figure 6.2.** (a) Cross-sectional SEM image of the PdSe<sub>2</sub>/Pd<sub>17</sub>Se<sub>15</sub> phase transformation. (b-c) Shows the atomic structure of PdSe<sub>2</sub> and Pd<sub>17</sub>Se<sub>15</sub>, respectively, overlaid with their atomic models. (d) Cross-section STEM of the PdSe<sub>2</sub>/Pd<sub>17</sub>Se<sub>15</sub> heterointerface with possible reaction surface schematically illustrated in (e). The FFT of the Pd<sub>17</sub>Se<sub>15</sub> is shown in (f) with diffraction patterns of (220), (322) and (412).

## 6.4 Optical properties in PdSe<sub>2</sub> and the new phase

To understand the differences in the atomic vibrations between the pristine and irradiated PdSe<sub>2</sub>, Raman spectroscopy was carried out. Fig. 6.3a shows the obtained Raman spectra for the anti-stokes and stokes mode for a ~10 nm sample. The red and black curves represent the spectra for the pristine and irradiated samples, respectively. The three main peaks observed correspond to the A<sub>g</sub><sup>1</sup>-B<sub>1g</sub><sup>1</sup>, A<sub>g</sub><sup>2</sup>, and A<sub>g</sub><sup>3</sup> modes as defined for PdSe<sub>2</sub> in ref [127]. The B<sub>1g</sub><sup>2</sup> peak is visible in the spectra, although with a lower intensity due to the orientation of the crystal and its anisotropic nature. The B<sub>1g</sub><sup>3</sup> peak is on the shoulder of the A<sub>g</sub><sup>3</sup> also with relatively lower intensity. There is no difference in the spectra of pristine PdSe<sub>2</sub> and after irradiation in the high-frequency region (~100cm<sup>-1</sup> – 300cm<sup>-1</sup>) as shown in Fig. 6.3b. Also, there is no observed peak shift from statistically over 30 measured samples. Reports shows a similarity in the Raman peak which is corroborated by theoretical calculations.<sup>130</sup> However, in the LF Raman region (< 60 cm<sup>-1</sup>), there is a significant difference (Fig. 6.3c): disappearance of some peaks, with new peaks appearing at a reduced intensity. Recent work on low-frequency PdSe<sub>2</sub> shows each LF Raman peak could fit a model that accurately depicts the number of PdSe<sub>2</sub> layers. The fact that LF Raman intensities in PdSe<sub>2</sub> crystals are comparable to that of HF Raman makes it possible to characterize interlayer atomic vibrations in the breathing mode. The observed LF Raman peaks after irradiation deviates from the established model for PdSe<sub>2</sub>, thereby suggesting not only the thinning of the crystal but the creation of a new material. To understand better the phase transition mechanism, a reduced plasma power, 25 W was used on a ~7 nm PdSe<sub>2</sub> flake. Fig. 6.3d shows the Raman spectra in the LF region suggesting a mixed intermediate phase which is thought could be a result of incomplete conversion of the PdSe<sub>2</sub> to Pd<sub>17</sub>Se<sub>15</sub>.

Auger electron spectroscopy (AES) is a great tool to reveal atomic compositions especially

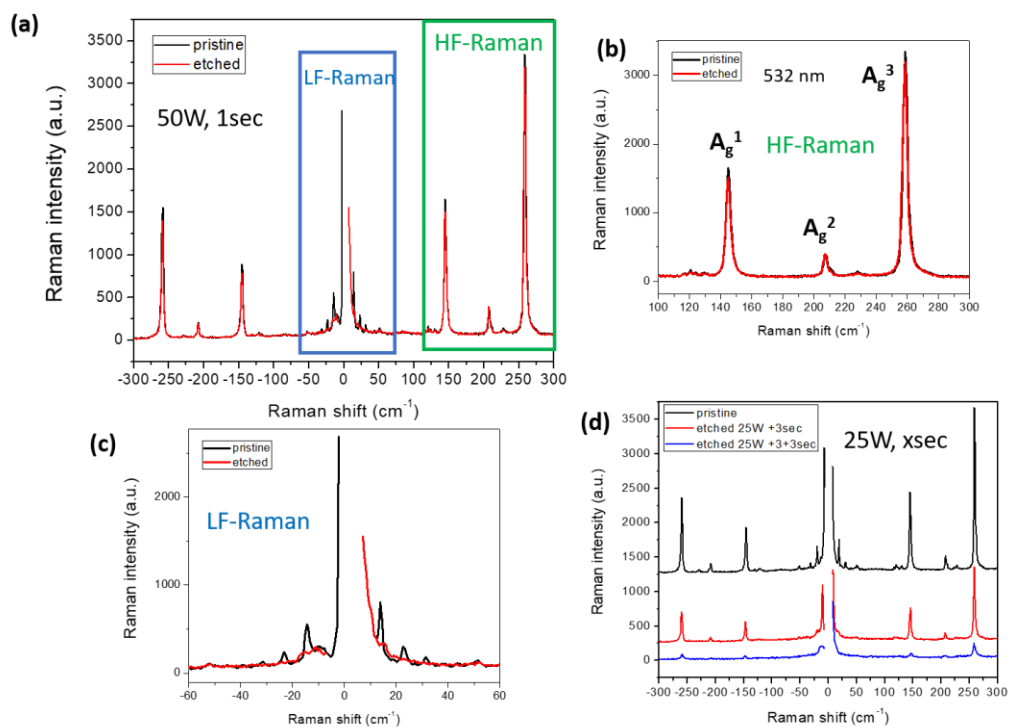


**Figure 6.3.** (a) Stokes and anti-Stokes Raman spectra of pristine and irradiated PdSe<sub>2</sub> crystals with a focus on the high-frequency (HF) region (b), and low-frequency (LF) region (c) for ~10 nm thick flake. (d) Raman spectra on ~ 7 nm thick flakes using a lower plasma power of 25 W, with treatment done at 3 sec intervals.

relating to vacancies and defects. Fig. 6.4a shows the scanning electron microscopy (SEM) image of a sample in which the left side has been exposed to  $\text{Ar}^+$  plasma, while the right part has been protected by PMMA through an electron-beam patterning fabrication process. The two red circles are where point-data from the nano-Auger was accumulated using a Survey Scan. Fig. 6.4 (b&d) show the survey spectra in both direct mode and derivative mode which indicates the presence of Pd, Se, C, Si, and O atoms. The Si atoms originate from the Si/SiO<sub>2</sub> substrate used, while C atoms indicate the presence of carbon residues from the photolithography process. Gray scale maps for Pd, and Se are shown in Fig. 6.4c (top images). The raw map data was processed this way: a smooth function was initially used on each map and then the contrast min/max were stretched to get a visually appealing image, and finally, the brightness was adjusted to minimize the noise level. Color maps and color-combined maps for Se + Pd was created from the individual maps: Fig. 6.4c (bottom) shows color-combined maps made from the gray-scale images, with a more blueish composition in the irradiated area due to the relative presence of more Pd atoms. To analyze the composition of the atoms in each material with improved accuracy, a 2  $\mu\text{m}$  x 1  $\mu\text{m}$  area was chosen around where the point data were taken. This is slightly different from point-data in that the resulting composition is an average of the area contained within the defined area. Table 6.1 shows the average composition from the two areas, where the Se/Pd ratio of the irradiated area is lower than that of the pristine area. This shows that the irradiated area has experienced the removal of about half the selenium atoms, which is the main driver for the phase transformation similar to those observed in  $\text{SnSe}_2$ .<sup>123</sup> It is important to note that the ratio for the irradiated areas is higher than expected. This is probably because the sensitivity factor was adjusted to match the pristine sample composition. Knowing that pristine  $\text{PdSe}_2$  has inherent Se vacancies, the Se/Pd ratio should be less than two, which when normalized will make the values of the Se/Pd for the irradiated

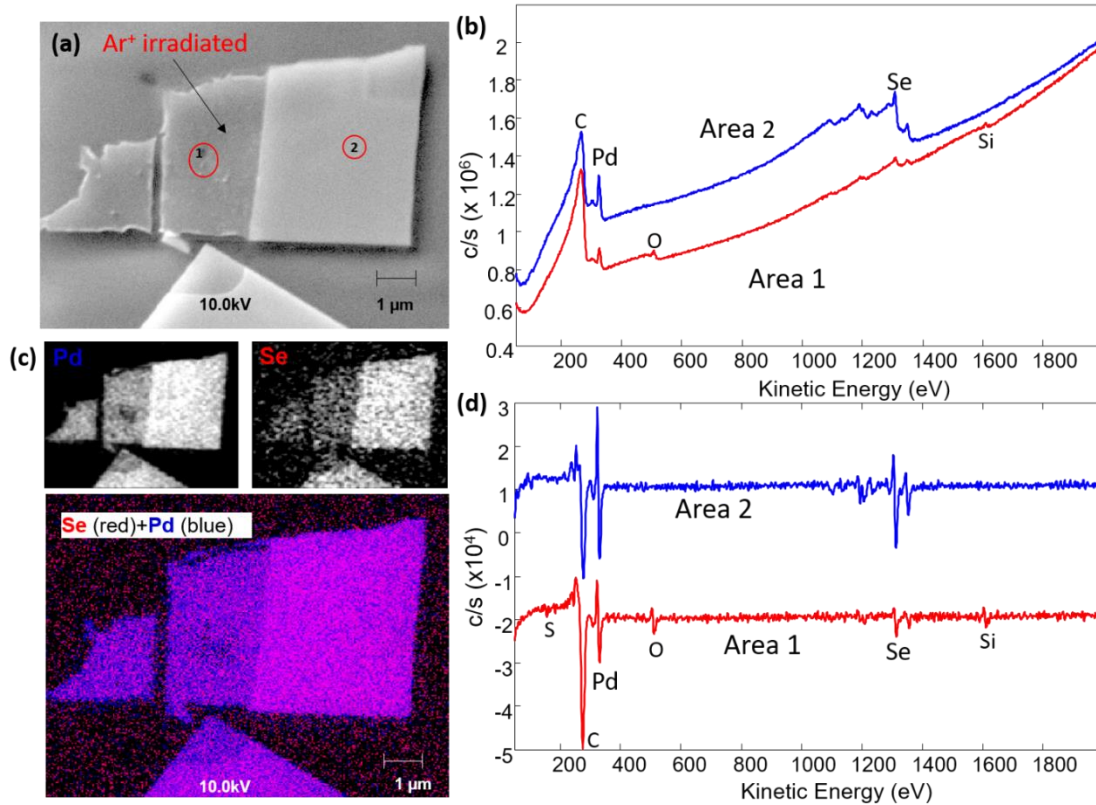


**Figure 6.4.** (a) Scanning electron microscope of irradiated and pristine regions of PdSe<sub>2</sub> crystal. (b) Survey spectra in both direct mode and (d) derivative mode which indicates the presence of Pd, Se, C, Si, and O atoms. (c) top image: gray scale maps for Pd, and Se obtained from the atomic composition in the survey spectra. Bottom image: color maps showing an increase in relative Pd composition for the irradiated areas.



**Table 6.1.** Composition of atoms from the irradiated and pristine areas obtained from nano-Auger electron spectroscopy

<b>Surface composition (at.%)</b>							
<b>Area</b>	<b>Pd</b>	<b>Se</b>	<b>C</b>	<b>O</b>	<b>Si</b>	<b>Se/Pd</b> <b>(actual)</b>	<b>Se/Pd</b> <b>(expected)</b>
<b>Irradiated</b>	20.7	22.0	51.7	2.2	3.3	0.941	0.882
<b>Pristine</b>	20.7	41.4	37.6	0.1	0.2	2.0	2.0

close to the expected values.

## 6.5 Improved contact resistance with PdSe<sub>2</sub>/Pd<sub>17</sub>Se<sub>15</sub> heterojunction Field Effect Transistors (FETs)

Using a two-terminal field-effect transistor (FET) configuration, the electrical properties of the new phase was studied. Fig. 6.5a shows that Pd<sub>17</sub>Se<sub>15</sub> displayed a metallic behavior with no gate dependence with total resistivity of  $\sim 1.9 \text{ k}\Omega\cdot\mu\text{m}$ . This is in agreement with previous studies conducted on the thin film and nanotube forms of Pd<sub>17</sub>Se<sub>15</sub>.<sup>130,131</sup> Furthermore, temperature-dependence measurements shown in Fig. 6.5b corroborated the metallic property, with a decrease in electrical conductivity with temperature due to the increase in the frequency of collisions between electrons and metal ions, at high temperature in metals. Due to the metallic property of the new phase, PdSe<sub>2</sub> devices can be designed with Pd<sub>17</sub>Se<sub>15</sub> contacts. Figure 6.5c shows the optical image of a PdSe<sub>2</sub> device with semiconducting channel, and the contact regions on the edges have undergone Ar<sup>+</sup> plasma-irradiation, with resulting Pd<sub>17</sub>Se<sub>15</sub> phase. From Fig. 6.5d, the absence of gate dependence in the transfer characteristics of the contacts confirm metallic behavior, while the channel displayed a typical semiconducting behavior observed in layered PdSe<sub>2</sub>.<sup>127</sup> The calculated two-terminal FET mobility of the channel using the metallic PdSe<sub>2</sub> is  $\sim 150 \text{ cm}^2\text{V}^{-1}\text{s}^{-1}$ , a 1000% increase when compared to  $\sim 12 \text{ cm}^2\text{V}^{-1}\text{s}^{-1}$  of similar thickness reported in Ref [127], in addition to the absence of hysteresis.

To understand the origin of the improvement in device performance, temperature-dependence electrical measurements were carried out to calculate the Schottky barrier at the Pd<sub>17</sub>Se<sub>15</sub>-PdSe<sub>2</sub> compared to the traditional metal-PdSe<sub>2</sub> interfaces. Fig. 6.5e shows  $I_{\text{ds}}-V_{\text{ds}}$  plots at different temperatures from 77K – 300K for zero gate voltage while Fig. 6.5f shows the

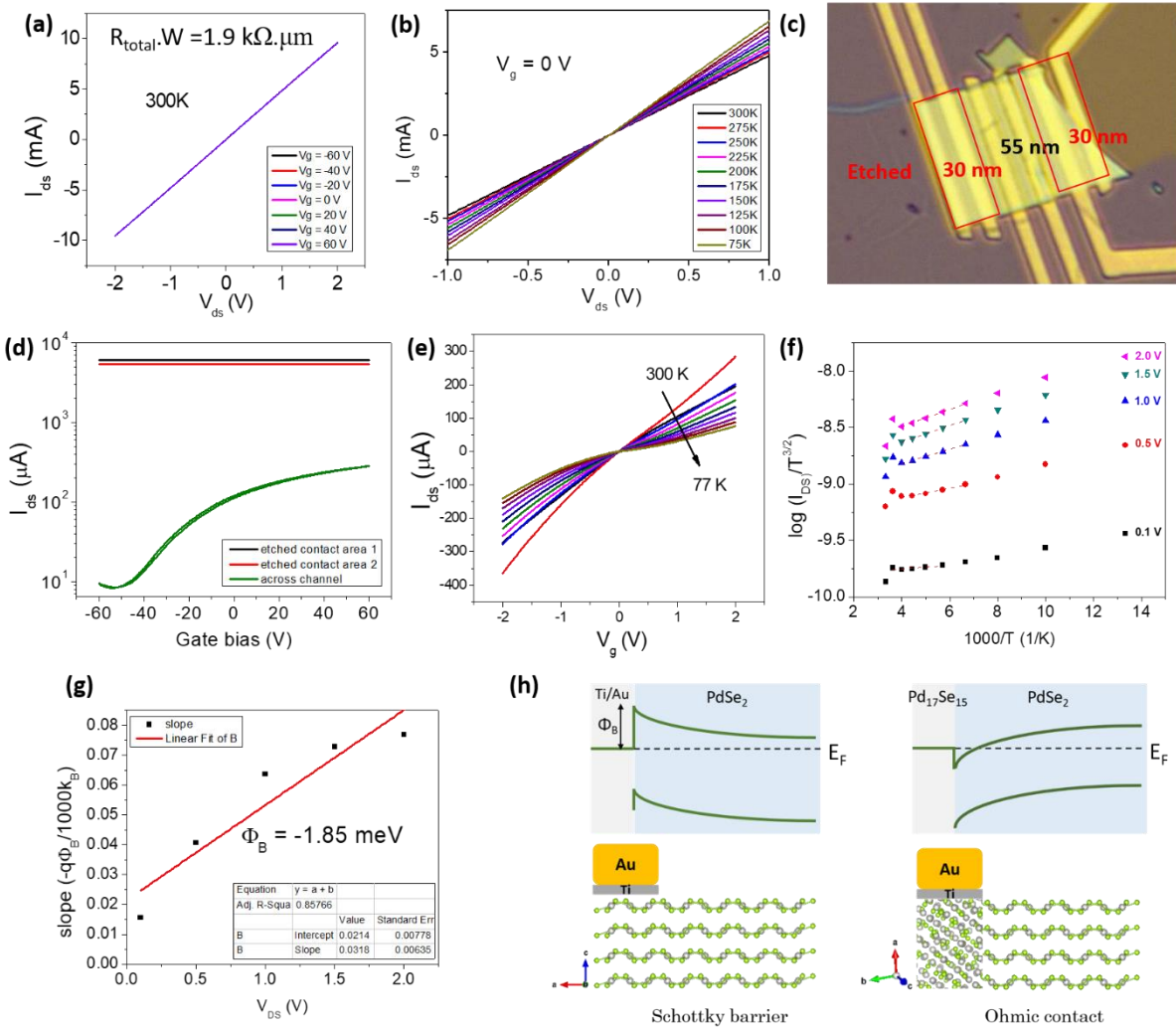


**Figure 6.5.** (a) Output characteristics of Pd<sub>17</sub>Se<sub>15</sub> device showing no gate dependence at room temperature. (b) Temperature-dependent output characteristics displaying a decrease in conductivity with temperature. (c) Optical image of PdSe<sub>2</sub> FET with Pd<sub>17</sub>Se<sub>15</sub> edge contacts. (d) Transfer characteristics for the metallic contacts and PdSe<sub>2</sub> semiconducting channel. (e) Temperature-dependent transfer characteristics. (f) The  $\log(I_{ds})$  versus  $1/T$  curves at different drain bias and the corresponding extracted slopes in (g). (h) Schematic diagram showing the absence of Schottky barrier in Pd<sub>17</sub>Se<sub>15</sub>/PdSe<sub>2</sub> junction.

corresponding  $\log(I_{DS})$  vs  $1000/T$  plot at different voltage bias. The current-density of thermionic emission through a metal-semiconductor contact is

$$I_{DS} = AT^{3/2} \exp\left[-\frac{q}{k_B T} \left(\Phi_B - \frac{V_{DS}}{n}\right)\right] \dots \dots \dots (6.1)$$

where A is the Richardson constant,  $V_{DS}$  is the applied voltage bias, T is the temperature, and  $k_B$  is the Boltzmann's constant.

The plot of the slope from Fig. 6.5f is shown in Fig. 6.5g from where Schottky barriers are extracted as the intercept on the y-axis. Extracted Schottky barrier height  $\Phi_B$  values  $\sim -1.85$  meV –  $-2.71$  meV, which is far less than  $\sim 62$  meV obtained when traditional Ti/Au contacts were used. This shows that the improvement in the device performance was as a result of the reduction in Schottky barrier height as illustrated in the schematic of Fig. 6.5g. Near-zero Schottky barrier heights are desired in electronic devices to facilitate a faster collection of charge carriers. In Fig. 6.5e the linear, symmetric nature of the output characteristics allude to the presence of ohmic contacts. For statistical purposes, several devices were fabricated with different thicknesses, with the Schottky barrier shown in Table 6.2. These near-zero values show the presence of ohmic contacts, which is much lower than values of 87.7 meV obtained when Ti/Au contacts were used for comparable channel thickness. The presence of Schottky barrier at the interface of metal-semiconductor has been a key issue limiting electronic device performance. The ability and ease to achieve ohmic contacts with the use of phase-transformed  $Pd_{17}Se_{15}$  for  $PdSe_2$ , makes the latter a more interesting material for the electronic industry.

**Table 6.2.** Comparison of the Schottky barrier heights at the heterointerface of metal-PdSe<sub>2</sub>.

	<b>PdSe<sub>2</sub> channel with Pd<sub>17</sub>Se<sub>15</sub></b>	<b>PdSe<sub>2</sub> channel with Ti/Au</b>
	<b>contact</b>	<b>contact</b>
<b>Schottky barrier height</b>	3.52 meV	87.7 meV
<b>(<math>\Phi_B</math>)</b>	7nm/4nm	5 nm/ Ti (5nm) Au (30 nm)
<b>Thickness of channel/contact</b>		
	5.81 meV	
	7nm/4nm	
	-1.85 meV	62 meV
	55 nm/30 nm	23 nm/Ti (5nm) Au (30 nm)
	-2.71 meV	
	55 nm/30 nm	

## 6.6 Summary

In conclusion, a fast method was used for phase patterning of few-layer PdSe<sub>2</sub> by Ar<sup>+</sup> plasma irradiation. Atomistic STEM and ab initio calculations were used to investigate the phase transformation of orthorhombic PdSe<sub>2</sub> to cubic Pd<sub>17</sub>Se<sub>15</sub>. It was revealed that the loss of Se atoms due to sputtering by high-energy atoms caused the conversion. Although the high-frequency Raman spectra of both materials are similar, LF Raman spectra is a unique technique to differentiate between the two phases. This is because the new phase breathing modes deviates from the model developed to determine the interlayer vibrations in pristine PdSe<sub>2</sub> crystals. Nano-Auger electron spectroscopy corroborates the chemical composition of the new phase with a loss of over 50% of the Se atoms. Electrical measurements confirm the new phase to be metallic in nature, unlike semiconducting PdSe<sub>2</sub>. The Pd<sub>17</sub>Se<sub>15</sub> was then used as a metallic contact to PdSe<sub>2</sub> field-effect transistors. The observed Schottky barrier present at the metal-semiconductor junction of 2D materials were reduced because of the seamless electrical, physical and chemical connectivity between the contact and the channel. This lead to higher device performance, with mobility increasing by about 1000%. The metallic Pd<sub>17</sub>Se<sub>15</sub> is an effective contact electrode with near zero Schottky barrier values of  $\sim -2.7$  meV at zero gate bias compared to  $\sim 90$  meV for traditional Ti/Au 3D metal contacts. This realization provides a pathway to design electronic devices with good ohmic contacts.

## Chapter 7: Conclusion

### 7.1 Major contributions of this thesis

The major contributions of this thesis are as follows:

1. Van der Waals (vdW) heterostructures of two dissimilar 2D materials was demonstrated using an all dry-transfer process. Gate-tunable rectifying behavior at the p-n junction was formed using WSe<sub>2</sub>-InSe and BP-MoSe<sub>2</sub> heterostructures, with rectification factor as high as 20.
2. This thesis demonstrates the isolation and optical and electronic characteristics of atomically thin palladium diselenide (PdSe<sub>2</sub>) crystals with a novel puckered pentagonal structure, experimentally revealed by atomic-resolution scanning transmission electron microscopy (AR-STEM). PdSe<sub>2</sub> has a unique puckered lattice with planar tetra-coordinate Pd atoms and Se-Se bonds forming a unique pentagonal structure. It exhibits a widely tunable band gap that varies from semi-metallic (bulk) to  $\sim 1.3$  eV (monolayer) - a band gap variation wider than any previously reported for 2D materials<sup>55,132</sup>. Raman spectroscopy and first-principles calculations show a strong interlayer interaction in PdSe<sub>2</sub> revealed by the large, layer-dependent Raman peak shifts.
3. Field-effect transistor (FET) device architecture was used to quantify and explore the performance of the 2D semiconductor material. FETs fabricated with conducting channels of few-layer PdSe<sub>2</sub> display ambipolar charge carrier conduction which has applications in inverters and logic gate circuits. Also, the transistor displays a layer-dependent property in which the on/off ratio can be increased from  $10^1$  (bulk) to  $10^6$  (2L) PdSe<sub>2</sub>. With high electron field-effect mobility of  $\sim 158$  cm<sup>2</sup> V<sup>-1</sup> s<sup>-1</sup>, PdSe<sub>2</sub> displays a useful property in designing novel electronic devices. In addition, PdSe<sub>2</sub> FET exhibit a metal-insulator

transition (MIT) with transition at around gate voltage of  $\sim 40$  V using traditional  $\text{SiO}_2$  substrates. The use of high dielectric sapphire bottom gate and ionic liquid could be used to drive down the operating voltages of these devices to less than 1 V. Overall,  $\text{PdSe}_2$  could become important for real-world applications due to their relative stability in air.

4. Finally, to achieve optimum device performance, phase engineering was employed to tune the contact area of the FET to a metallic phase, thereby achieving desired ohmic contact. It has been established that the interface between the metal contact and 2D channel material must be carefully designed to eliminate or reduce large contact resistance, which is a result of the Schottky barrier present at the metal-semiconductor interface. The non-ohmic barrier could limit the flow of charge carriers, and cause undesired non-linear transport characteristics. Thus, contact engineering has gained a widespread interest in 2D material devices. Deliberate choice of metal contacts with Fermi levels that align well with either the conduction or valence band of the semiconductor material has been a route that has been explored. For example, low work-function Ti is typically used with  $\text{MoS}_2$  for electron conduction, while high work-function Pd and Au are necessary for hole conduction. Mismatches in the band alignment at the interface makes the use of homojunctions – contacts from the same material but with a different phase - a favorable route to eliminate contact resistance and achieve ohmic contacts. For example, semiconductor  $\text{MoS}_2$  have displayed lower contact resistance when matched with metallic 1T  $\text{MoS}_2$ . The realization of metallic  $\text{PdSe}_2$  will facilitate the widespread adoption of  $\text{PdSe}_2$  in electronic devices.

## 7.2 Recommendations for future work

Based on the findings and discussion presented in this thesis, the following studies are recommended for future works:



## 1. Optimization of PdSe<sub>2</sub> field-effect transistor (FET) performance

To improve the prospects of 2D semiconductor technologies in future electronic devices, their performance must be comparable to or better than those obtained using silicon. Current technologies using silicon (Si) have been able to achieve mobility as high as  $\sim 1400 \text{ cm}^2\text{V}^{-1}\text{s}^{-1}$  at room temperature. Previous work on PdSe<sub>2</sub> have shown that we can realize up to  $\sim 220 \text{ cm}^2\text{V}^{-1}\text{s}^{-1}$ , which was achieved using a basic two-terminal configuration usually associated with high contact resistance. Therefore, there is need to explore, experimentally, the intrinsic carrier mobility of layered PdSe<sub>2</sub> by using a four-terminal probe configuration to eliminate contact resistance associated with the two-terminal measurements. In addition, metallic Pd<sub>17</sub>Se<sub>15</sub> can be used as interface contacts to reduce the Schottky barrier present at the metal-semiconductor junction. Also, to achieve an enhanced device performance, ionic gels can be used to increase carrier concentration in the semiconducting channel and high dielectric substrates can to reduce operating voltages. Lastly, using few-layer hexagonal boron nitride as a passivation/dielectric layer can help maintain device performance over an extended period.

## 2. Single material homojunction devices

Due to the widely tunable band gap of PdSe<sub>2</sub> from semi-metallic to semiconductor behavior, PdSe<sub>2</sub> can realize a stable, efficient single material device without the need for phase engineering, with both channel and contact materials made from layered PdSe<sub>2</sub>. Several layers of PdSe<sub>2</sub> could form the electrical contact, with few-layer PdSe<sub>2</sub> serving as the semiconducting channel. Similar device configuration has been predicted for the structural analogue of PdSe<sub>2</sub><sup>111</sup>. This should reduce contact resistance, and further optimize device performance.

### 3. 2D thermoelectric devices

Previous report shows interestingly high Seebeck coefficients ( $>200 \mu\text{V/K}$ ) and high electrical conductivity in 2D PdSe<sub>2</sub>.<sup>1</sup> From preliminary experiments conducted during this thesis, the electrical transport is mildly affected by temperature, suggesting a low thermal conductivity. These properties, in conjunction with the anisotropic characteristics in the electronic structure of PdSe<sub>2</sub>, suggests that exploring their applications in thermoelectric devices is a worthy venture.<sup>133</sup>

### 4. Exploring the few-layer properties of metallic-Pd<sub>17</sub>Se<sub>15</sub>.

Since we can now realize Pd<sub>17</sub>Se<sub>15</sub> from 2D PdSe<sub>2</sub>, the electrical, optical and structural properties of atomically-thin Pd<sub>17</sub>Se<sub>15</sub> can be studied. Previous work on bulk Pd<sub>17</sub>Se<sub>15</sub> shows a metallic characteristic, with superconductivity behavior below 2.2 K.<sup>134</sup> Also, Pd<sub>17</sub>Se<sub>15</sub> has shown great applications in electrocatalysis and solar cells.<sup>130,131</sup>

## References

- 1 Schaller, R. R. Moore's law: past, present and future. *IEEE spectrum* **34**, 52-59 (1997).
- 2 Novoselov, K. S. *et al.* A roadmap for graphene. *Nature* **490**, 192-200 (2012).
- 3 Wang, Q. H., Kalantar-Zadeh, K., Kis, A., Coleman, J. N. & Strano, M. S. Electronics and optoelectronics of two-dimensional transition metal dichalcogenides. *Nature Nanotechnology* **7**, 699-712 (2012).
- 4 Radisavljevic, B., Radenovic, A., Brivio, J., Giacometti, i. V. & Kis, A. Single-layer MoS<sub>2</sub> transistors. *Nature Nanotechnology* **6**, 147-150 (2011).
- 5 Mak, K. F., Lee, C., Hone, J., Shan, J. & Heinz, T. F. Atomically thin MoS<sub>2</sub>: a new direct-gap semiconductor. *Physical Review Letters* **105**, 136805 (2010).
- 6 Li, L. *et al.* Black phosphorus field-effect transistors. *Nature Nanotechnology* **9**, 372-377 (2014).
- 7 Novoselov, K. *et al.* Two-dimensional atomic crystals. *Proceedings of the National Academy of Sciences of the United States of America* **102**, 10451-10453 (2005).
- 8 Cann, O. *These are the top 10 emerging technologies of 2016*, [<https://www.weforum.org/agenda/2016/06/top-10-emerging-technologies-2016/>](https://www.weforum.org/agenda/2016/06/top-10-emerging-technologies-2016/) (2016).
- 9 Novoselov, K. S. *et al.* Electric field effect in atomically thin carbon films. *Science* **306**, 666-669 (2004).
- 10 Tan, C. *et al.* Recent advances in ultrathin two-dimensional nanomaterials. *Chemical Reviews* **117**, 6225-6331 (2017).
- 11 Novoselov, K. S. *et al.* Two-dimensional gas of massless Dirac fermions in graphene. *Nature* **438**, 197-200 (2005).
- 12 Schwierz, F. Graphene transistors. *Nature Nanotechnology* **5**, 487-496 (2010).
- 13 Liao, L. *et al.* High- $\kappa$  oxide nanoribbons as gate dielectrics for high mobility top-gated graphene transistors. *Proceedings of the National Academy of Sciences* **107**, 6711-6715 (2010).
- 14 Splendiani, A. *et al.* Emerging photoluminescence in monolayer MoS<sub>2</sub>. *Nano Letters* **10**, 1271-1275 (2010).
- 15 Geim, A. K. & Grigorieva, I. V. Van der Waals heterostructures. *Nature* **499**, 419-425 (2013).
- 16 Novoselov, K., Mishchenko, A., Carvalho, A. & Neto, A. C. 2D materials and van der Waals heterostructures. *Science* **353**, aac9439 (2016).
- 17 Furchi, M. M., Pospischil, A., Libisch, F., Burgdörfer, J. & Mueller, T. Photovoltaic effect in an electrically tunable van der Waals heterojunction. *Nano Letters* **14**, 4785-4791 (2014).
- 18 Ajayan, P., Kim, P. & Banerjee, K. Two-dimensional van der Waals materials. *Physics Today* **69**, 38-44 (2016).
- 19 Withers, F. *et al.* Light-emitting diodes by band-structure engineering in van der Waals heterostructures. *Nature Materials* **14**, 301-306 (2015).
- 20 Yang, H., Kim, S. W., Chhowalla, M. & Lee, Y. H. Structural and quantum-state phase transitions in van der Waals layered materials. *Nature Physics* **13**, 931 (2017).
- 21 Kappera, R. *et al.* Phase-engineered low-resistance contacts for ultrathin MoS<sub>2</sub> transistors. *Nature Materials* **13**, 1128-1134 (2014).
- 22 Lin, Z. *et al.* Defect engineering of two-dimensional transition metal dichalcogenides. *2D Materials* **3**, 022002 (2016).

- 23 Li, X. & Zhu, H. Two-dimensional MoS<sub>2</sub>: Properties, preparation, and applications. *Journal of Materiomics* **1**, 33-44 (2015).
- 24 Miró, P., Ghorbani-Asl, M. & Heine, T. Two Dimensional Materials Beyond MoS<sub>2</sub>: Noble-Transition-Metal Dichalcogenides. *Angewandte Chemie International Edition* **53**, 3015-3018 (2014).
- 25 Mak, K. F. & Shan, J. Photonics and optoelectronics of 2D semiconductor transition metal dichalcogenides. *Nature Photonics* **10**, 216-226 (2016).
- 26 Mahjouri-Samani, M. *et al.* Tailoring Vacancies Far Beyond Intrinsic Levels Changes the Carrier Type and Optical Response in Monolayer MoSe<sub>2-x</sub> Crystals. *Nano Letters* **16**, 5213-5220 (2016).
- 27 Zhao, W. *et al.* Evolution of electronic structure in atomically thin sheets of WS<sub>2</sub> and WSe<sub>2</sub>. *ACS nano* **7**, 791-797 (2012).
- 28 Ovchinnikov, D., Allain, A., Huang, Y.-S., Dumcenco, D. & Kis, A. Electrical transport properties of single-layer WS<sub>2</sub>. *ACS nano* **8**, 8174-8181 (2014).
- 29 Pudasaini, P. R. *et al.* High-performance multilayer WSe<sub>2</sub> field-effect transistors with carrier type control. *Nano Research*, 1-9 (2017).
- 30 Pudasaini, P. R. *et al.* High performance top-gated multilayer WSe<sub>2</sub> field effect transistors. *Nanotechnology* **28**, 475202 (2017).
- 31 Stanford, M. G. *et al.* High conduction hopping behavior induced in transition metal dichalcogenides by percolating defect networks: toward atomically thin circuits. *Advanced Functional Materials* **27** (2017).
- 32 Puretzky, A. A., Oyedele A., Xiao K., Haglund A. V., Sumpter B. G., Mandrus D. G., Geohegan D. B., and Liang L. Anomalous interlayer vibrations in strongly coupled layered PdSe<sub>2</sub>. *2D Materials* (2018).
- 33 Zhao, Y. *et al.* Extraordinarily Strong Interlayer Interaction in 2D Layered PtS<sub>2</sub>. *Advanced Materials* (2016).
- 34 Wang, Y. *et al.* Monolayer PtSe<sub>2</sub>, a New Semiconducting Transition-Metal-Dichalcogenide, Epitaxially Grown by Direct Selenization of Pt. *Nano Letters* **15**, 4013-4018 (2015).
- 35 Zhao, Y. *et al.* High-Electron-Mobility and Air-Stable 2D Layered PtSe<sub>2</sub> FETs. *Advanced Materials* (2016).
- 36 Wang, Y., Li, Y. & Chen, Z. Not your familiar two dimensional transition metal disulfide: structural and electronic properties of the PdS<sub>2</sub> monolayer. *Journal of Materials Chemistry C* **3**, 9603-9608 (2015).
- 37 Li, L. *et al.* Few-Layered PtS<sub>2</sub> Phototransistor on h-BN with High Gain. *Advanced Functional Materials* **27** (2017).
- 38 Lee, C. *et al.* Anomalous lattice vibrations of single-and few-layer MoS<sub>2</sub>. *ACS nano* **4**, 2695-2700 (2010).
- 39 Tongay, S. *et al.* Monolayer behaviour in bulk ReS<sub>2</sub> due to electronic and vibrational decoupling. *Nature Communications* **5** (2014).
- 40 Voiry, D., Mohite, A. & Chhowalla, M. Phase engineering of transition metal dichalcogenides. *Chemical Society Reviews* **44**, 2702-2712 (2015).
- 41 Chhowalla, M. *et al.* The chemistry of two-dimensional layered transition metal dichalcogenide nanosheets. *Nature Chemistry* **5**, 263 (2013).
- 42 Zhang, W., Huang, Z., Zhang, W. & Li, Y. Two-dimensional semiconductors with possible high room temperature mobility. *Nano Research* **7**, 1731-1737 (2014).

- 43 Yuan, J. *et al.* Wafer-scale fabrication of 2D van der Waals heterojunctions for efficient and broadband photodetection. *arXiv preprint arXiv:1803.04695* (2018).
- 44 Huang, H., Zhou, S. & Duan, W. Type-II Dirac fermions in the PtSe<sub>2</sub> class of transition metal dichalcogenides. *Physical Review B* **94**, 121117 (2016).
- 45 Cao, W., Tang, P., Zhang, S.-C., Duan, W. & Rubio, A. Stable Dirac semimetal in the allotropes of group-IV elements. *Physical Review B* **93**, 241117 (2016).
- 46 Noh, H.-J. *et al.* Experimental realization of type-II Dirac fermions in a PdTe<sub>2</sub> superconductor. *Physical Review Letters* **119**, 016401 (2017).
- 47 Zhang, S. *et al.* Penta-graphene: A new carbon allotrope. *Proceedings of the National Academy of Sciences* **112**, 2372-2377 (2015).
- 48 Ma, Y., Kou, L., Li, X., Dai, Y. & Heine, T. Room temperature quantum spin Hall states in two-dimensional crystals composed of pentagonal rings and their quantum wells. *NPG Asia Materials* **8**, e264 (2016).
- 49 Yagmurcukardes, M. *et al.* Pentagonal monolayer crystals of carbon, boron nitride, and silver azide. *Journal of Applied Physics* **118**, 104303 (2015).
- 50 Wang, X.-Q., Li, H.-D. & Wang, J.-T. Prediction of a new two-dimensional metallic carbon allotrope. *Physical Chemistry Chemical Physics* **15**, 2024-2030 (2013).
- 51 Rao, M. Exhaustive search of convex pentagons which tile the plane. *arXiv preprint arXiv:1708.00274* (2017).
- 52 Xu, W., Zhang, G. & Li, B. Thermal conductivity of penta-graphene from molecular dynamics study. *The Journal of Chemical Physics* **143**, 154703 (2015).
- 53 Mannix, A. J. *et al.* Synthesis of borophenes: Anisotropic, two-dimensional boron polymorphs. *Science* **350**, 1513-1516 (2015).
- 54 Li, X., Dai, Y., Li, M., Wei, W. & Huang, B. Stable Si-based pentagonal monolayers: high carrier mobilities and applications in photocatalytic water splitting. *Journal of Materials Chemistry A* **3**, 24055-24063 (2015).
- 55 Sun, J., Shi, H., Siegrist, T. & Singh, D. J. Electronic, transport, and optical properties of bulk and mono-layer PdSe<sub>2</sub>. *Applied Physics Letters* **107**, 153902 (2015).
- 56 Xia, F., Wang, H. & Jia, Y. Rediscovering black phosphorus as an anisotropic layered material for optoelectronics and electronics. *Nature Communications* **5** (2014).
- 57 Luo, Z. *et al.* Anisotropic in-plane thermal conductivity observed in few-layer black phosphorus. *Nature Communications* **6**, 8572 (2015).
- 58 Sofer, Z. *et al.* Layered Black Phosphorus: Strongly Anisotropic Magnetic, Electronic, and Electron-Transfer Properties. *Angewandte Chemie* **128**, 3443-3447 (2016).
- 59 Priyadarshi, A., Chauhan, Y. S., Bhowmick, S. & Agarwal, A. Strain-tunable charge carrier mobility of atomically thin phosphorus allotropes. *Physical Review B* **97**, 115434 (2018).
- 60 Tao, L. *et al.* Silicene field-effect transistors operating at room temperature. *Nature Nanotechnology* **10**, 227-231 (2015).
- 61 Li, L. *et al.* Buckled germanene formation on Pt (111). *Advanced Materials* **26**, 4820-4824 (2014).
- 62 Quhe, R. *et al.* Tunable and sizable band gap in silicene by surface adsorption. *Scientific Reports* **2**, 853 (2012).
- 63 Gong, C. *et al.* Electronic and optoelectronic applications based on 2D novel anisotropic transition metal dichalcogenides. *Advanced Science* (2017).

- 64 Li, L. *et al.* Direct observation of the layer-dependent electronic structure in phosphorene. *Nature Nanotechnology* **12**, 21-25 (2017).
- 65 Li, H. *et al.* Mechanical Exfoliation and Characterization of Single-and Few-Layer Nanosheets of WSe<sub>2</sub>, TaS<sub>2</sub>, and TaSe<sub>2</sub>. *Small* **9**, 1974-1981 (2013).
- 66 Yin, Z. *et al.* Single-layer MoS<sub>2</sub> phototransistors. *ACS Nano* **6**, 74-80 (2011).
- 67 Fang, H. *et al.* Strong interlayer coupling in van der Waals heterostructures built from single-layer chalcogenides. *Proceedings of the National Academy of Sciences* **111**, 6198-6202 (2014).
- 68 Oyedele, A. D., Rouleau, C. M., Geohegan, D. B. & Xiao, K. The growth and assembly of organic molecules and inorganic 2D materials on graphene for van der Waals heterostructures. *Carbon* (2018).
- 69 Ross, J. S. *et al.* Interlayer exciton optoelectronics in a 2D heterostructure p-n junction. *Nano Letters* **17**, 638-643 (2017).
- 70 Bertolazzi, S., Krasnozhan, D. & Kis, A. Nonvolatile memory cells based on MoS<sub>2</sub>/graphene heterostructures. *ACS nano* **7**, 3246-3252 (2013).
- 71 Suk, J. W. *et al.* Transfer of CVD-grown monolayer graphene onto arbitrary substrates. *ACS Nano* **5**, 6916-6924 (2011).
- 72 Li, X. *et al.* Two-dimensional GaSe/MoSe<sub>2</sub> misfit bilayer heterojunctions by van der Waals epitaxy. *Science Advances* **2**, e1501882 (2016).
- 73 Bonaccorso, F. *et al.* Production and processing of graphene and 2D crystals. *Materials Today* **15**, 564-589 (2012).
- 74 Castellanos-Gomez, A. *et al.* Deterministic transfer of two-dimensional materials by all-dry viscoelastic stamping. *2D Materials* **1**, 011002 (2014).
- 75 Haigh, S. *et al.* Cross-sectional imaging of individual layers and buried interfaces of graphene-based heterostructures and superlattices. *Nature Materials* **11**, 764-767 (2012).
- 76 Fang, H. *et al.* High-performance single layered WSe<sub>2</sub> p-FETs with chemically doped contacts. *Nano Letters* **12**, 3788-3792 (2012).
- 77 Feng, W., Zheng, W., Cao, W. & Hu, P. Back gated multilayer InSe transistors with enhanced carrier mobilities via the suppression of carrier scattering from a dielectric interface. *Advanced Materials* **26**, 6587-6593 (2014).
- 78 Larentis, S., Fallahazad, B. & Tutuc, E. Field-effect transistors and intrinsic mobility in ultra-thin MoSe<sub>2</sub> layers. *Applied Physics Letters* **101**, 223104 (2012).
- 79 Chen, Z., Gacem, K., Boukhicha, M., Biscaras, J. & Shukla, A. Anodic bonded 2D semiconductors: from synthesis to device fabrication. *Nanotechnology* **24**, 415708 (2013).
- 80 Tonndorf, P. *et al.* Photoluminescence emission and Raman response of monolayer MoS<sub>2</sub>, MoSe<sub>2</sub>, and WSe<sub>2</sub>. *Optics Express* **21**, 4908-4916 (2013).
- 81 Mahjouri-Samani, M. *et al.* Patterned arrays of lateral heterojunctions within monolayer two-dimensional semiconductors. *Nature Communications* **6** (2015).
- 82 Brent, J. R. *et al.* Production of few-layer phosphorene by liquid exfoliation of black phosphorus. *Chemical Communications* **50**, 13338-13341 (2014).
- 83 He, J. *et al.* Exceptional and anisotropic transport properties of photocarriers in black phosphorus. *ACS Nano* **9**, 6436-6442 (2015).
- 84 Phaneuf-L'Heureux, A.-L. *et al.* Polarization-resolved Raman study of bulk-like and Davydov-induced vibrational modes of exfoliated Black Phosphorus. *Nano Letters* **16**, 7761-7767 (2016).

- 85 Soulard, C. *et al.* Experimental and theoretical investigation on the relative stability of the  
PdS<sub>2</sub>-and pyrite-type structures of PdSe<sub>2</sub>. *Inorganic Chemistry* **43**, 1943-1949 (2004).
- 86 Grønvold, F. & Røst, E. The crystal structure of PdSe<sub>2</sub> and PdS<sub>2</sub>. *Acta Crystallographica*  
**10**, 329-331 (1957).
- 87 Puretzky, A. A. *et al.* Low-frequency Raman fingerprints of two-dimensional metal  
dichalcogenide layer stacking configurations. *ACS Nano* **9**, 6333-6342 (2015).
- 88 Kresse, G. & Furthmüller, J. Efficiency of ab-initio total energy calculations for metals  
and semiconductors using a plane-wave basis set. *Computational Materials Science* **6**,  
15-50 (1996).
- 89 Perdew, J. P., Burke, K. & Ernzerhof, M. Generalized gradient approximation made  
simple. *Physical Review Letters* **77**, 3865 (1996).
- 90 Dion, M., Rydberg, H., Schröder, E., Langreth, D. C. & Lundqvist, B. I. Van der Waals  
density functional for general geometries. *Physical Review Letters* **92**, 246401 (2004).
- 91 Hulliger, F. Electrical properties of some nickel-group chalcogenides. *Journal of Physics*  
*and Chemistry of Solids* **26**, 639-645 (1965).
- 92 Wilson, J. & Yoffe, A. The transition metal dichalcogenides discussion and interpretation  
of the observed optical, electrical and structural properties. *Advances in Physics* **18**, 193-  
335 (1969).
- 93 Giannozzi, P. *et al.* QUANTUM ESPRESSO: a modular and open-source software  
project for quantum simulations of materials. *Journal of Physics: Condensed matter* **21**,  
395502 (2009).
- 94 Cooper, V. R. Van der Waals density functional: An appropriate exchange functional.  
*Physical Review B* **81**, 161104 (2010).
- 95 Klimeš, J., Bowler, D. R. & Michaelides, A. Chemical accuracy for the van der Waals  
density functional. *Journal of Physics: Condensed Matter* **22**, 022201 (2009).
- 96 Grimme, S. Semiempirical GGA-type density functional constructed with a long-range  
dispersion correction. *Journal of Computational Chemistry* **27**, 1787-1799 (2006).
- 97 Iberi, V. *et al.* Nanoforging Single Layer MoSe<sub>2</sub> Through Defect Engineering with  
Focused Helium Ion Beams. *Scientific Reports* **6** (2016).
- 98 Togo, A. & Tanaka, I. First principles phonon calculations in materials science. *Scripta*  
*Materialia* **108**, 1-5 (2015).
- 99 Liang, L. & Meunier, V. Electronic and thermoelectric properties of assembled graphene  
nanoribbons with elastic strain and structural dislocation. *Applied Physics Letters* **102**,  
143101 (2013).
- 100 Liang, L. & Meunier, V. First-principles Raman spectra of MoS<sub>2</sub>, WS<sub>2</sub> and their  
heterostructures. *Nanoscale* **6**, 5394-5401 (2014).
- 101 Umari, P., Pasquarello, A. & Dal Corso, A. Raman scattering intensities in  $\alpha$ -quartz: A  
first-principles investigation. *Physical Review B* **63**, 094305 (2001).
- 102 Puretzky, A. A. *et al.* Twisted MoSe<sub>2</sub> bilayers with variable local stacking and interlayer  
coupling revealed by low-frequency raman spectroscopy. *ACS Nano* **10**, 2736-2744  
(2016).
- 103 Gajdoš, M., Hummer, K., Kresse, G., Furthmüller, J. & Bechstedt, F. Linear optical  
properties in the projector-augmented wave methodology. *Physical Review B* **73**, 045112  
(2006).



- 104 Massote, D. V., Liang, L., Kharche, N. & Meunier, V. Electronic, vibrational, Raman, and scanning tunneling microscopy signatures of two-dimensional boron nanomaterials. *Physical Review B* **94**, 195416 (2016).
- 105 Ling, X. *et al.* Low-frequency interlayer breathing modes in few-layer black phosphorus. *Nano Letters* **15**, 4080-4088 (2015).
- 106 Aroyo, M. *et al.* Crystallography online: Bilbao crystallographic server. *Bulg. Chem. Commun* **43**, 183-197 (2011).
- 107 Denisov, V. N., Mavrin, B. N. & Podobedov, V. B. Hyper-Raman scattering by vibrational excitations in crystals, glasses and liquids. *Physics Reports* **151**, 1-92 (1987).
- 108 Luo, X., Zhao, Y., Zhang, J., Xiong, Q. & Quek, S. Y. Anomalous frequency trends in MoS<sub>2</sub> thin films attributed to surface effects. *Physical Review B* **88**, 075320 (2013).
- 109 Lu, X., Luo, X., Zhang, J., Quek, S. Y. & Xiong, Q. Lattice vibrations and Raman scattering in two-dimensional layered materials beyond graphene. *Nano Research* **9**, 3559-3597 (2016).
- 110 Zhang, X. *et al.* Phonon and Raman scattering of two-dimensional transition metal dichalcogenides from monolayer, multilayer to bulk material. *Chemical Society Reviews* **44**, 2757-2785 (2015).
- 111 Ghorbani-Asl, M., Kuc, A., Miró, P. & Heine, T. A Single-Material Logical Junction Based on 2D Crystal PdS<sub>2</sub>. *Advanced Materials* **28**, 853-856 (2016).
- 112 Radisavljevic, B. & Kis, A. Mobility engineering and a metal–insulator transition in monolayer MoS<sub>2</sub>. *Nature Materials* **12**, 815-820 (2013).
- 113 Lin, M.-W. *et al.* Thickness-dependent charge transport in few-layer MoS<sub>2</sub> field-effect transistors. *Nanotechnology* **27**, 165203 (2016).
- 114 Pradhan, N. R. *et al.* Metal to insulator quantum-phase transition in few-layered ReS<sub>2</sub>. *Nano Letters* **15**, 8377-8384 (2015).
- 115 Rasmussen, F. A. & Thygesen, K. S. Computational 2D materials database: Electronic structure of transition-metal dichalcogenides and oxides. *The Journal of Physical Chemistry C* **119**, 13169-13183 (2015).
- 116 Wu, J., Mao, N., Xie, L., Xu, H. & Zhang, J. Identifying the Crystalline Orientation of Black Phosphorus Using Angle-Resolved Polarized Raman Spectroscopy. *Angewandte Chemie* **127**, 2396-2399 (2015).
- 117 Gu, T. *et al.* Regenerative oscillation and four-wave mixing in graphene optoelectronics. *Nature Photonics* **6**, 554-559 (2012).
- 118 Gullans, M., Chang, D., Koppens, F., de Abajo, F. G. & Lukin, M. D. Single-photon nonlinear optics with graphene plasmons. *Physical Review Letters* **111**, 247401 (2013).
- 119 Yin, X. *et al.* Edge nonlinear optics on a MoS<sub>2</sub> atomic monolayer. *Science* **344**, 488-490 (2014).
- 120 Lin, Y.-C., Dumcenco, D. O., Huang, Y.-S. & Suenaga, K. Atomic mechanism of the semiconducting-to-metallic phase transition in single-layered MoS<sub>2</sub>. *Nature Nanotechnology* **9**, 391 (2014).
- 121 Cho, S. *et al.* Phase patterning for ohmic homojunction contact in MoTe<sub>2</sub>. *Science* **349**, 625-628 (2015).
- 122 Lin, J. *et al.* Novel Pd<sub>2</sub>Se<sub>3</sub> Two-Dimensional Phase Driven by Interlayer Fusion in Layered PdSe<sub>2</sub>. *Physical Review Letters* **119**, 016101 (2017).
- 123 Sutter, E. *et al.* Electron-beam induced transformations of layered tin dichalcogenides. *Nano Letters* **16**, 4410-4416 (2016).

- 124 Wang, Y. *et al.* Structural phase transition in monolayer MoTe<sub>2</sub> driven by electrostatic doping. *Nature* **550**, 487 (2017).
- 125 ElGhazali, M. A. *et al.* Pressure-induced superconductivity up to 13.1 K in the pyrite phase of palladium diselenide PdSe<sub>2</sub>. *Physical Review B* **96**, 060509 (2017).
- 126 Song, S. *et al.* Room temperature semiconductor–metal transition of MoTe<sub>2</sub> thin films engineered by strain. *Nano Letters* **16**, 188-193 (2015).
- 127 Oyedele, A. D. *et al.* PdSe<sub>2</sub>: Pentagonal 2D Layers with High Air Stability for Electronics. *Journal of the American Chemical Society* (2017).
- 128 Chow, W. L. *et al.* High Mobility 2D Palladium Diselenide Field-Effect Transistors with Tunable Ambipolar Characteristics. *Advanced Materials* **29** (2017).
- 129 Okamoto, H. The Pd-Se (palladium-selenium) system. *Journal of Phase Equilibria* **13**, 69-72 (1992).
- 130 Kukunuri, S., Karthick, S. & Sampath, S. Robust, metallic Pd<sub>17</sub>Se<sub>15</sub> and Pd<sub>7</sub>Se<sub>4</sub> phases from a single source precursor and their use as counter electrodes in dye sensitized solar cells. *Journal of Materials Chemistry A* **3**, 17144-17153 (2015).
- 131 Kukunuri, S., Austeria, P. M. & Sampath, S. Electrically conducting palladium selenide (Pd<sub>4</sub>Se, Pd<sub>17</sub>Se<sub>15</sub>, Pd<sub>7</sub>Se<sub>4</sub>) phases: synthesis and activity towards hydrogen evolution reaction. *Chemical Communications* **52**, 206-209 (2016).
- 132 Miro, P., Audiffred, M. & Heine, T. An atlas of two-dimensional materials. *Chemical Society Reviews* **43**, 6537-6554 (2014).
- 133 Qin, D. *et al.* Monolayer PdSe<sub>2</sub>: A promising two-dimensional thermoelectric material. *Scientific Reports* **8**, 2764 (2018).
- 134 Naren, H., Tamizhavel, A. & Ramakrishnan, S. in *Journal of Physics: Conference Series*. 012074 (IOP Publishing).
- 135 Oyedele, A., McNutt, N. W., Rios, O. & Keffer, D. J. Hierarchical Model for the Analysis of Scattering Data of Complex Materials. *JOM* **68**, 1583-1588 (2016).
- 136 García-Negrón, V. *et al.* Evaluation of nano-and mesoscale structural features in composite materials through hierarchical decomposition of the radial distribution function. *Journal of Applied Crystallography* **51** (2018).

# Appendix

## Author's published journal papers

- 1 **A. Oyedele**, et al. "PdSe<sub>2</sub>: Pentagonal Puckered 2D layers with High Air Stability for Electronics.", *Journal of American Chemical Society*, 139.40 (2017): 14090-14097. (Selected as **journal cover**). (Also, this work was selected as a **DOE science highlight** by the US Department of Energy (DOE) and as an independent highlight in Chemistry World, Royal Society of Chemistry).
- 2 **A. Oyedele**, et al. "Vacancy-induced phase transition in palladium diselenide (PdSe<sub>2</sub>) for the realization of ohmic contacts in 2D electronics." *In Preparation*.
- 3 **A. Oyedele**, et. al. "The growth and assembly of organic molecules and inorganic 2D materials on graphene for van der Waals heterostructures." **Invited review**, *Carbon*, 131(2018): 246-257.
- 4 A. Puretzky, **A. Oyedele**, et. al. "Anomalous low-frequency Raman scattering in 2D layered PdSe<sub>2</sub> arising from strong interlayer interactions." *2D Materials*.
- 5 G. D. Nguyen, L. Liang, Q. Zou, M. Fu, **A. Oyedele**, et. al. "Manipulation of subsurface selenium vacancies in PdSe<sub>2</sub>." *Under review*.
- 6 M. Mahjouri-Samani, L. Liang, **A. Oyedele**, et al. "Tailoring Vacancies Far Beyond Intrinsic Levels Changes the Carrier Type and Optical Response in Monolayer MoSe<sub>2-x</sub> Crystals.", *Nano Letters*, 16.8 (2016): 5213-5220.
- 7 P. R. Pudasaini, **A. Oyedele**, et al. "High performance multilayer WSe<sub>2</sub> field effect transistors with carrier type control", *Nano Research*, 11.2 (2018): 722-730.
- 8 P. R. Pudasaini, M. G. Stanford, **A. Oyedele**, et.al. "High performance top-gated multilayer WSe<sub>2</sub> field effect transistors." *Nanotechnology*, 28.47 (2017): 475202.

- 9 M. Z. Bellus, M. Mahjouri-Samani, S. D. Lane, **A. Oyedele**, et al. "Time-Resolved Measurements of Carrier Transfer across Monolayer MoS<sub>2</sub>-MoSe<sub>2</sub> Lateral Heterojunctions." *Under Review*.
- 10 M. G Stanford, P. R. Pudasaini, E. T. Gallmeier, N. Cross, L. Liang, **A. Oyedele**, et al. "High conduction hopping behavior induced in transition metal dichalcogenides by percolating defect networks: toward atomically thin circuits." *Advanced Functional Materials*, 27.36 (2017).
- 11 C. Zhang, P. Pudasaini, **A. Oyedele**, et. al. "Ion Migration Studies in 2D Molybdenum Trioxide Thin Flake through Ionic Liquid Gating." *Under Review*.
- 12 K. Wang, N. Cross, A. Boulesbaa, P. R. Pudasaini, M. K. Tian, M. Mahjouri-Samani, M. P. Oxley, **A. Oyedele**, et al "Correlating the Isoelectronic Mo Doping and Optical Properties in WS<sub>2</sub> Monolayers Grown by Chemical Vapor Deposition." *In Preparation*.
- 13 K. Wang, Z. Hu, B. R. Srijanto, A. A. Poretzky, X. Li, N. Guputa, H. Yu, M. Tian, M. Mahjouri-Samani, X. Gao, **A. Oyedele**, et al. "Strain Tolerant Growth of Two Dimensional Materials on Curved Surfaces." *Under Review*.
- 14 A. Strasser, **A. Oyedele**, et al. "High Performance Perovskite Solar Cells: A Review on Device Engineering and Physics." *In Preparation*.
- 15 J. Choi, C. Kim, J. Pison, **A. Oyedele**, et al., "Exploiting the potential of DPTMM as an efficient donor molecule in vacuum-processed BHJ organic solar cells", *RSC Advances*, 4.10 (2014): 5236-5242.
- 16 **A. Oyedele**, et al. "A Hierarchical Model for the Analysis of Scattering Data of Complex Materials.", *Journal of Materials*, 68.6 (2016): 1583-1588.

- 17 V. Garcia-Negron\*, **A. Oyedele\***, et al. Assessment of Nano- and Mesoscale Structural Features in Carbon Composites through Hierarchical Decomposition of the Radial Distribution Function, *Journal of Applied Crystallography*, 51.1 (2018). (co-first author)
- 18 A. Adediran, and **A. Oyedele**. "Operational aspects and regulatory gaps in additive manufacturing." *Additive Manufacturing Handbook: Product Development for the Defense Industry* (2017): 7.

### Conference presentations

- 1 "Pentagonal 2D palladium diselenide with high carrier mobility for air-stable electronics." MRS Fall Meeting, Nov 29- Dec 3, 2017, Boston, MA. (Graduate Student Award Oral Presentation and Poster Presentation)
- 2 "Anisotropic 2D palladium diselenide with high mobility for air-stable electronics." The 64th AVS International Symposium and Exhibition, Oct 29-Nov 3, 2017, Tampa, FL. (Oral Presentation)
- 3 "Anisotropic 2D palladium diselenide with high mobility for air-stable electronics." Oak Ridge Postdoctoral Association (ORPA) Research Symposium, August 18, 2017, Oak Ridge, TN. (Oral Presentation)
- 4 "Palladium diselenide, a new 2D semiconductor with tunable bandgaps and high mobility for electronics." 2017 Joint Nanoscience and Neutron Scattering User Meeting, July 31 – Aug 4, 2017, Oak Ridge, TN. (Oral Presentation)
- 5 "Synthesis and Optoelectronics of Two-Dimensional Heterostructures." UTK-Future Materials Forum, July 18, 2017, Knoxville, TN. (Poster Presentation)

- 6 “Palladium diselenide, a new 2D semiconductor with tunable bandgaps and high mobility for electronics.” 2017 Workshop on Spins, Valleys, and Topological States in 2D and Layered Materials, June 4 – 8, 2017, Columbus, OH. (Poster Presentation)
- 7 “Van der Waals heterojunctions built via an all dry-transfer method.” Two Dimensional Electronics Beyond Graphene - Gordon Research Conference, June 5-10, 2016, South Hadley, MA. (Poster Presentation)

### Notable awards

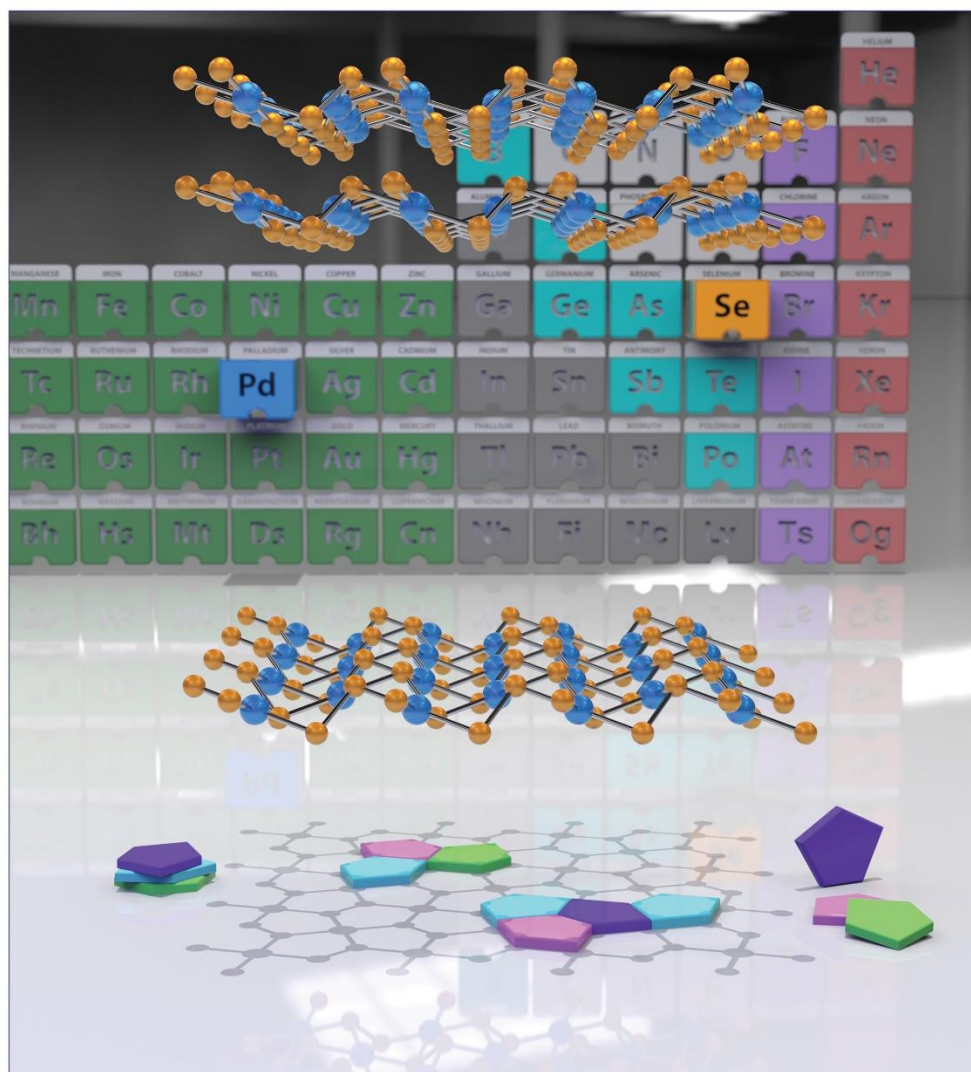
- Materials Research Society (MRS) Graduate Student Silver Award, Fall 2017 MRS Boston
- Center for Nanophase Materials Science (CNMS) Distinguished Scientific Paper of 2017
- Joint SNS/CNMS User Meeting Best Students’ Poster Award (2017)
- Chancellor's Citation for Extraordinary Professional Promise (2016)
- 1<sup>st</sup> place, Vol Court Entrepreneurship Pitch Competition (2015)
- \$8,000 start-up grant from the US consulate in Nigeria to develop an energy program for high school students (2015)

The work on “*PdSe<sub>2</sub>: Pentagonal Puckered 2D layers with High Air Stability for Electronics.*” was selected for cover in the Journal of American Chemical Society.

October 11, 2017  
Volume 139  
Number 40  
pubs.acs.org/JACS

# J | A | C | S

JOURNAL OF THE AMERICAN CHEMICAL SOCIETY





## Vita

Akinola Oyedele grew up in Ifo, thirty miles from Lagos – Africa’s most populous city. He obtained his bachelor’s degree in electrical and electronics engineering from the University of Lagos, where he graduated top of his class. With support from Air Liquide and Exxon Mobil, Akinola did his Master’s thesis at Ecole Polytechnique, France and worked on developing nanomaterials for solar cell applications. In August 2013, Akinola moved to Tennessee to pursue his PhD. He has been working in Dr. Kai Xiao and Dr. David Geohegan’s group at Oak Ridge National Laboratory (ORNL) since 2014 on his dissertation research.

Akinola’s research revolves around understanding the optical and electronic properties of new two-dimensional (2D) nanomaterials. His work on palladium diselenide ( $\text{PdSe}_2$ ) was the first experimental realization of stable, high mobility pentagonal 2D materials, which are suitable for electronic and optoelectronic applications. As a side-venture, Akinola worked with Prof. D. J. Keffer of the Department of Materials Science to develop an algorithm that reduces the computational time for predicting material structure by a factor of 1,000,000. This mathematical model has led to two first-authored, peer-reviewed publications <sup>135,136</sup>.